

## Radiometric and Radiation Response of Visible FPAs

Submitted to NASA NEPP Program  
by John Hubbs (AFRL)  
April 2007

### 1 Executive Summary

This report presents the results of radiometric and radiation (total dose, debris gamma, and proton fluence) characterizations of visible focal plane arrays (VFPAs) developed by Rockwell Sciences Company (RSC) for Ball Aerospace and Technologies Corp. (BATC) on the NASA Cross Enterprise Program. A summary of the significant results found during these tests is provided below.

The readout integrated circuit (ROIC) used in these devices was originally developed for use in space based infrared systems operating at deep cryogenic temperatures and was selected because of its proven tolerance to total ionizing radiation.<sup>1</sup> The detectors are a 128 x 128 array of 60  $\mu\text{m}$  x 60  $\mu\text{m}$  pixel elements that have been anti-reflection (AR) coated to improve the response at very short wavelengths. These visible focal plane arrays were operated at -40 C (233 K).

Two focal planes were characterized using cobalt-60 radiation to produce ionizing total dose damage in the VFPAs. Both operational and performance data were obtained as functions of total dose. The first device tested showed no appreciable change in responsivity or noise up to 300 krad(Si). However, at the next dose level of 600 krad(Si), the readout was non-operational due to failure in the digital circuitry. The second device was characterized to a total dose of 750 krad(Si) with no observed change in responsivity. An increase dark current was observed in both devices, and in the second device, the dark current caused an increase in noise at low irradiance at 400 krad(Si) and above.

The increase in dark current was somewhat un-expected for visible PIN detectors. The median dark current increased more than two orders of magnitude at 300 krad(Si) for the first device and a factor of 350 at 750 krad(Si) for pixels near the edge for the second device. The dark current was found to be a strong function of detector bias, with pixels near the edge of the array showing a greater increase in dark current with bias than those near the center. Since the optical response was not a function of bias, it is hypothesized that the dark current is a surface effect and that the variation in dark current with location is due to a variation in pixel bias, caused by a voltage drop across the pixel common lead. As the total dose increased, the dark current and the voltage drop increased.

Additional data were obtained on the second device after approximately 1 week of annealing at -

---

<sup>1</sup> J. E. Hubbs, M. E. Gramer, D. C. Arrington, G. A. Dole, D. Maestas-Jepson, S. E. Takeall, "Total Ionizing Dose and Proton Radiation Characterization of Si P-i-N Visible Hybrid Focal Plane Arrays," *Proc. of SPIE*, vol. 5902, pp. 128-142, 2005.

40 C, and the dark current was found to be significantly lower. These data imply that if the total dose is accumulated at a slower rate, as in orbit, the dark current could be significantly lower than observed in these tests where the dose rate was approximately 17 rad(Si)/sec and no time was generally given for annealing to take place.

Two focal plane arrays were also characterized using proton radiation that produces both displacement and ionizing damage to the VFPA's. Operational and performance data were obtained on both devices using 63 MeV protons. No appreciable change in responsivity or noise was observed up to a fluence of  $3 \times 10^{12}$  protons/cm<sup>2</sup> (400 krad(Si) of total dose). The median dark current increased approximately 2 orders of magnitude, but even at this higher level, the dark current did not contribute significantly to the median noise at integration times of 10 ms. The dark current produced by protons was higher around the edges as was seen with gamma ionizing radiation.

In conclusion the data presented in this report shows that up to a total dose of 750 krad(Si) and a proton fluence (63 MeV protons) of  $3 \times 10^{12}$  protons/cm<sup>2</sup>, no change in quantum efficiency was observed for the PIN detectors at any wavelength that was greater than experimental reproducibility. There was a significant increase in dark current with both total dose and proton fluence that was decidedly non-uniform in nature. It is proposed that this dark current non-uniformity is due to non-uniformities in pixel bias, due to a voltage drop across the pixel common lead caused by the increased dark current. With an applied bias of 15 volts, the voltage drop was approximately 6 volts for the center pixel at a total dose of 750 krad(Si). The maximum dark current (for pixels near the edge) at 750 krad(Si) was approximately 2.5 pA.

While one of four devices readouts failed between 300 and 600 krad(Si), one other device was fully functioning at 750 krad(Si). For this second device, there was an increase in power dissipation of a factor of 2, but no change in readout conversion gain or readout noise was observed. It is felt that the one failure was an anomaly and that most readouts should function to approximately 1 Mrad(Si) with little change in operation or performance. This conclusion is based on these data and a significant amount of additional data obtained on another program that used this same readout at a temperature of 40 K.

## 2 Introduction

This report presents the results of radiometric and radiation (debris gamma, total dose, and proton fluence) characterizations of visible focal plane arrays (VFPAs) arrays developed by Rockwell Sciences Company (RSC) for Ball Aerospace and Technologies Corp. (BATC) on the NASA Cross Enterprise Program. A summary of the performance of each device is provided in the sections below. The nominal operating temperature was - 40 C (233 K).

All measurements were made by the staff of the Infrared Radiation Effects Laboratory (IRREL), which is located at the AFRL Phillips Research Site (PRS), Kirtland AFB, New Mexico. While this facility is a government laboratory, the AF allows the IRREL staff to use AF equipment for measurements on other programs of interest to the AF as long as that work does not interfere with AF testing needs. All data were obtained using the Mosaic Array Test System III (MATS III); which was used to control the operation of test devices and to acquire and reduce the test data. MATS III was developed for the AFRL/VSSS by Ball Aerospace & Technologies Corp. (BATC) for the characterization of Infrared and Visible FPAs and associated devices in clear and radiation environments<sup>2</sup>.

The remainder of this report is divided into four sections: Section 3 gives a description of the VFPAs characterized; Section 4 discusses the measurements and analyses performed on the data; Section 5 describes the measurement conditions; and Section 6 presents the characterization data obtained for each device.

---

<sup>2</sup> Arrington, D. and Hubbs, J., *Development of Enhanced Performance of the Mosaic Array Test System (MATS II)*, WL-TR-90-24, Weapons Laboratory, Kirtland AFB, New Mexico, May, 1990.

### **3 Device Descriptions**

#### **3.1.1 Detector Array**

The detectors are 128 x 128 arrays of 60  $\mu\text{m}$  x 60  $\mu\text{m}$  PIN detectors that were anti-reflection (AR) coated to improve their short wavelength response. The detector arrays were provided in two thicknesses: 50 and 110 micrometers.

#### **3.1.2 Packaging**

The VFPA's were mounted in 68-pin leadless chip carriers.

#### **3.1.3 Devices Characterized**

7 VFPA's were delivered to IRREL for these tests, two of which were Engineering Units. Total dose tests were made on SN #155 and SN #154 while proton fluence tests were made on SN #150 and #157. SN #150 and the two Engineering Units had detector arrays that were 110 microns in thickness, while the others were 50 microns thick.

### **4 Measurement Conditions**

All radiometric measurements were made with the VFPA's mounted in liquid nitrogen pour-filled cryogenic Dewars. A 0.5-inch limiting aperture mounted on a 77 K cold shield approximately 5.5 inches from the VFPA set the minimum irradiance from room temperature at a very low level. Radiometric measurements were made using two visible sources: a uniform illumination source from Spectra-Physics (SP Model 66990) was used for measurements between 250 and 400 nm, and an integrating sphere source from LabSphere (LS) was used from 400 to 1000nm. A variable aperture, which was part of the LS source, allowed the irradiance to be changed at any wavelength in the range of 400 to 1000 nm.

#### **4.1 Irradiance Calibration**

The irradiance from both sources in the Dewar on the VFPA's was measured using a silicon PIN diode from UTD Sensors (Model PIN UV 100L, SN 73623). This diode, which was calibrated using standards traceable to NIST, was placed in the Dewar at the location of the VFPA's for these measurements.

The radiometric setup for the integrating sphere source is shown in Figure 1 (the setup is similar for the Spectra Physics (SP) source). Pictures of the two sources located under the Dewar during radiometric tests are shown in Figure 2. Various spectral filters were placed between the source and the Dewar window and the current in the PIN diode was measured at each wavelength. The irradiance was then calculated using the calibration provided by UTD Sensors. The resulting calibration data are shown in Table 1.

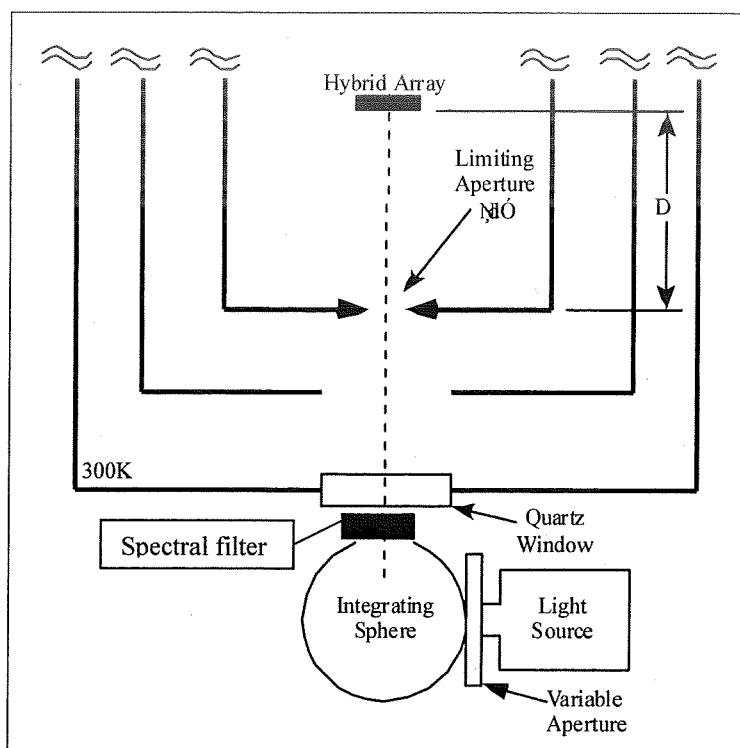


Figure 1. Setup for Calibration and Radiometric Measurements

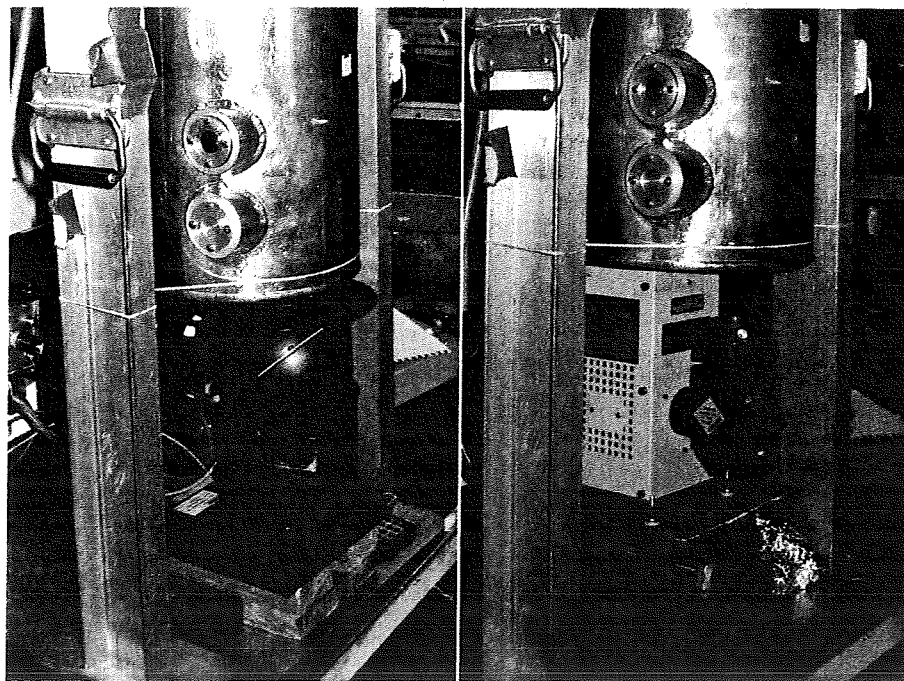


Figure 2. Radiometric Setup for Integrating Sphere (l) and Spectra-Physics Source (r)

Filter Wavelength (nm)	Irradiance SP Source (ph/s-cm <sup>2</sup> )	Filter Wavelength (nm)	Irradiance Integrating Sphere (ph/s-cm <sup>2</sup> )
250	$1.55 \times 10^{13}$	400	$3.28 \times 10^{11}$
260	$3.22 \times 10^{13}$	450	$4.49 \times 10^{11}$
280	$1.15 \times 10^{14}$	500	$2.05 \times 10^{12}$
290	$7.22 \times 10^{13}$	551	$5.07 \times 10^{12}$
300	$8.57 \times 10^{13}$	600	$8.53 \times 10^{12}$
310	$5.68 \times 10^{13}$	650	$1.08 \times 10^{13}$
314	$9.07 \times 10^{13}$	700	$1.27 \times 10^{13}$
340	$1.79 \times 10^{14}$	800	$1.07 \times 10^{13}$
350	$1.05 \times 10^{13}$	850	$2.28 \times 10^{13}$
360	$1.18 \times 10^{14}$	902	$3.00 \times 10^{13}$
400	$2.44 \times 10^{13}$	949	$3.06 \times 10^{13}$
		1000	$2.18 \times 10^{13}$
		1050	$1.99 \times 10^{13}$
		1100	$1.50 \times 10^{13}$

Table 1. Dewar Irradiances for each source

During these calibration measurements, the output of each source was monitored at each wavelength. The SP source output was monitored using the current in a second PIN diode from UDT that was placed just above the spectral filter. The output of the Integrating sphere was monitored by a silicon diode that is mounted within the sphere. During radiometric measurements, these outputs were again monitored to insure that the calibrated irradiances were being produced on the VFPA's.

## 4.2 VFPA Operating Conditions

While all clock waveforms were set to the values recommended by RSC, several changes were made to the DC biasing of the readout to improve its total dose hardness. An integration time of approximately 10 ms was used during the collection of the majority of the radiometric data. The VFPA chip carriers were held in thermal contact with an aluminum block and the temperature of this block was set and controlled to the desired temperature. However, while the temperature of the block is controlled, it must be assumed that the chip carrier makes good thermal contact with it and that the VFPA is mounted to the chip carrier with good thermal contact. To aid with the contact between the chip carrier and the aluminum block, thin indium was used as a shim. A temperature of -40 C was maintained for the duration of each radiation test except when dark current was determined as a function of temperature.

## 4.3 AFRL Cobalt-60 (<sup>60</sup>Co) Total Dose Source Configuration

Total dose and gamma transient measurements were performed at the AFRL 5,300 Curie Cobalt-60 (<sup>60</sup>Co) source located at Kirtland Air Force Base, New Mexico. Prior to the total dose exposure, dosimetry measurements were made to determine the dose rate at the surface of the VFPA as a function of distance from the source. The dose rate was measured using a calibrated ionization gauge placed inside the Dewar at the location of the VFPA. The dose rate used for accumulating total dose was approximately 16.8 rad(Si)/s. The VFPA was fully biased and

operational at -40 C during irradiation.

A picture of the Dewar placed near the cobalt-60 source is shown in Figure 3. The cobalt-60 is stored in the lead container below the table, and when it is used, it rises up in the stainless tube. The dose rate on the test device within the Dewar is varied by changing the distance between the cobalt-60 and the Dewar. Because the cobalt-60 is essentially a point source, all test electronics must be shielded using lead bricks as shown in Figure 4.

#### **4.4 U.C. Davis Source Configuration**

Proton fluence measurements were performed at the Crocker Nuclear Laboratory (CNL) of the University of California, Davis (UC Davis). The proton beam facility at CNL is based on the 76" Isochronous Cyclotron that can provide protons with energies up to 68 MeV. A picture of the target area, where the VFPA was irradiated, is shown in Figure 5, and a side view of the test Dewar mounted in front of the proton beam line is shown in Figure 6. The beam energy is measured by a time of flight system in combination with knowledge of the cyclotron magnetic field settings. Beam counting is performed by the combination of a Secondary Electron Emission Monitor and a removable Faraday Cup. A Segmented Secondary Electron Emission Monitor positions the proton beam in the center of the target. The spatial distribution of the beam is shown in Figure 7 where the z-axis is a measurement of the proton fluence expressed as an optical density and the x- and y-axis are position measurements expressed in cm from the center of the distribution. The spatial distribution changes from 100 % at the center of the distribution to 97% at 2 cm to 92% at 4 cm. For these experiments, the cyclotron was configured to irradiate the VFPA at 63 MeV, and the VFPA was fully biased and operational at -40 C during irradiation. During proton characterizations, the VFPA was mounted at a 45° angle with respect to the proton beam line and to the incident photon irradiance so that the proton beam could uniformly irradiate the VFPA.

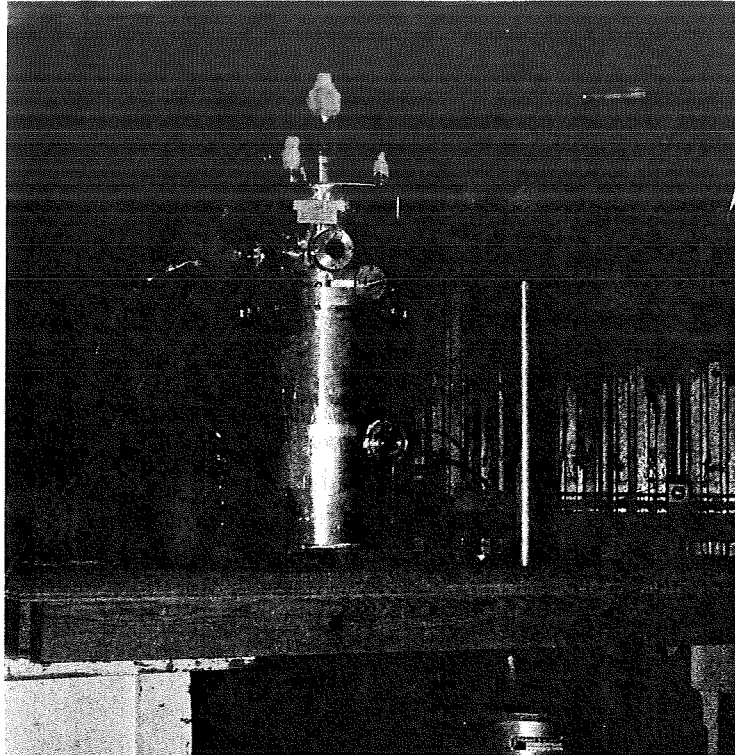


Figure 3. AFRL Cobalt-60 Source with Dewar Mounted Nearby

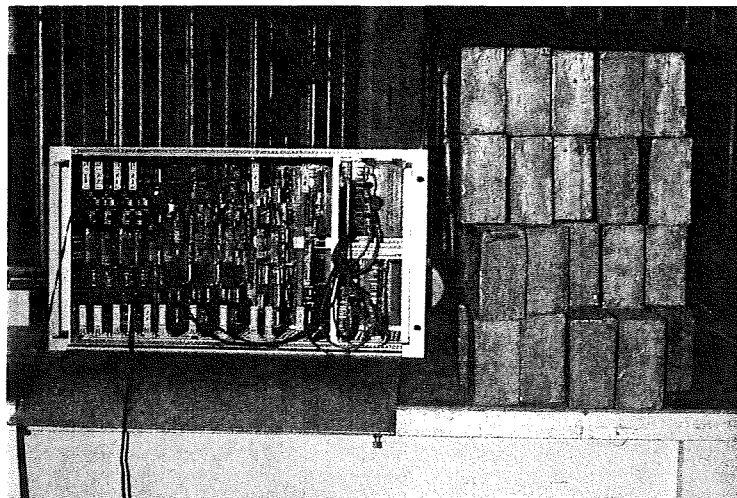


Figure 4. Lead Bricks Used To Shield Test Electronics



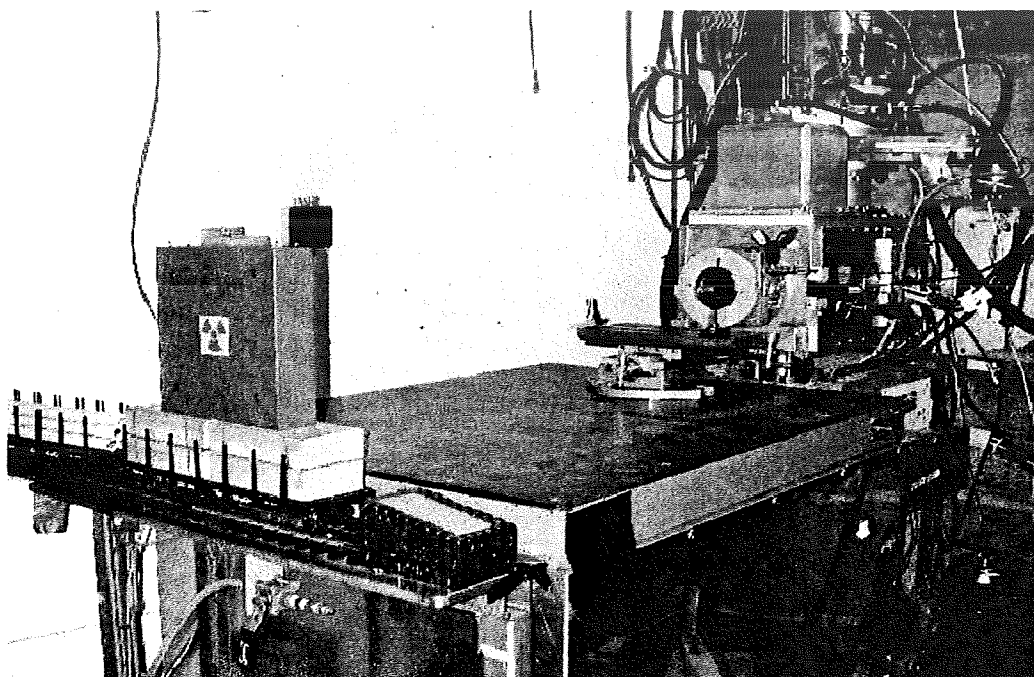


Figure 5. VFPA Irradiation Area at UC Davis Crocker Nuclear Lab Proton Test Facility.

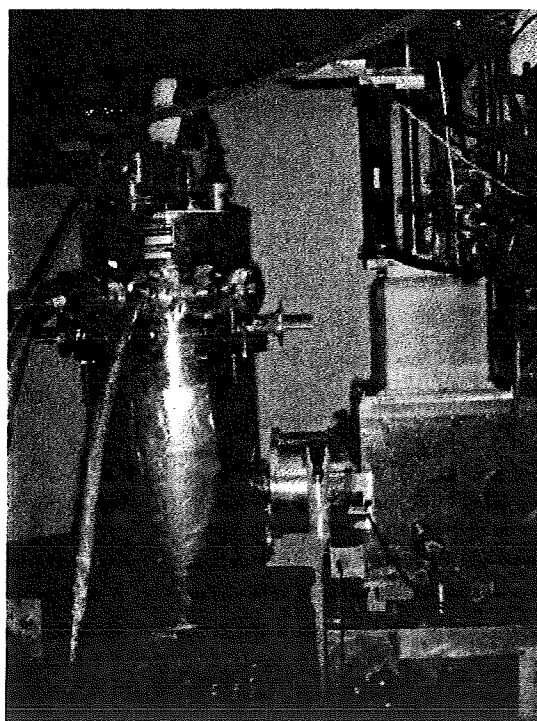


Figure 6. Side View of Test Dewar Mounted In Front of Proton Beam Line.

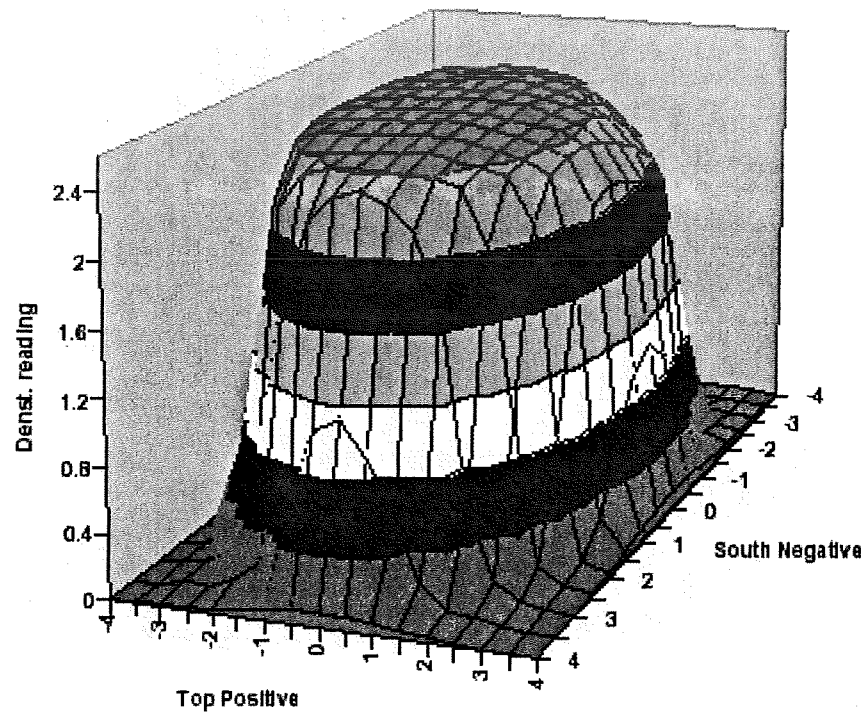


Figure 7. Spatial Distribution of Proton Beam Output.

## 5 Characterization Measurements

Radiometric performance data were obtained on each VFPA that was characterized. Several operational parameters that were varied during these data collections include temperature, integration time, detector bias, and photon irradiance. In the remainder of this section, the measurements made and the figures of merit used to quantify device performance are described.

### 5.1 DC Currents, Voltages, and Power Dissipation

The voltages applied to and the currents into each VFPA node are important measures of the health of a VFPA and provide a measure of its power dissipation. The detector current can also be monitored as a function of photon irradiance, to provide data for computing the average detector quantum efficiency. Other dc measurements included the monitoring of reference outputs and test circuit performance. These data are of particular interest during radiation testing because they provide data on the “health” and status of the test device at each radiation level and thus, provide insight into failure mechanisms and allow methodologies to be developed to mitigate these failures.

### 5.2 Conversion Gain

The conversion gain of a VFPA is the transfer function between the charge developed on the unit cell integration capacitor (integrated pixel current) and the output voltage. If the conversion gain is known, detector parameters can be calculated from measured VFPA voltage data. Two methods can and have been used to determine the conversion gain: (1) the dc current method and (2) the mean-variance method.

#### 5.2.1 DC Current Method

In the dc current method, the total current flowing in the detector common node and the median pixel output voltage are measured at a number of photon irradiances. A unique total current and median pixel output voltage are produced at each irradiance level. Expressions for the total detector current and the pixel output voltage are given in Equation 1 and 2, respectively.

$$I_{total} = N_p (e \eta E_q A_{Det} + I_{dark}) \quad (1)$$

$$V_{output} = C_g \left( \eta E_q A_{det} \tau_{int} + \frac{I_{dark} \tau_{int}}{q} \right) + V_{offset} \quad (2)$$

where:

$N_p$  = number of pixels in array (128 x 128)

$q$  = electronic charge ( $1.6 \times 10^{-19}$  coulomb)

$\eta$  = quantum efficiency (electrons/photon)

$E_q$  = photon irradiance (ph/s-cm<sup>2</sup>)

$A_{det}$  = detector area (cm<sup>2</sup>)

$C_g$  = conversion gain (volts/electron)

$\tau_{int}$  = integration time (seconds)

$I_{dark}$  = total pixel dark current (amps)

$V_{offset}$  = multiplexer dc voltage output (volts)

In the expression for the detector current, the first term gives the contribution from the photon irradiance and the second is due to pixel dark current. Similarly, in the equation for the pixel output voltage, the first term is the output due to the photon irradiance, the second term is due to

the pixel dark current, and the third is a constant due to the multiplexer circuitry. Expressions for the photon current in terms of the pixel output voltage and the pixel output in terms of total current are given by:

$$I_{total} = \left( \frac{qN_e}{C_g \tau_{int}} \right) V_{output} \quad , \quad V_{output} = \left( \frac{C_g \tau_{int}}{qN} \right) I_{total} \quad (3)$$

If the output voltage is plotted as a function of the measured current, a straight line is usually obtained if the VFPA does not have an excessive number of high dark current pixels. The slope of this line is then used to determine the conversion gain using Equation 4. A conversion gain obtained using Equation 4 is an average value for the entire array

$$\begin{aligned} \frac{dV_{output}}{dI_{total}} &= \left( \frac{C_g \tau_{int}}{qN_e} \right) = \frac{\Delta V}{\Delta I} = \frac{\Delta V}{N_p \Delta i} = \frac{\Delta V}{N_p} \left( \frac{1}{\Delta Q_i / \tau_{int}} \right) = \frac{\Delta V}{N_p} \left( \frac{\tau_{int}}{q \Delta N_e} \right) \\ C_g \left( \frac{\text{Volts}}{\text{electron}} \right) &\equiv \frac{\Delta V}{\Delta N_e} = \frac{\tau_{int}}{qN_p} \cdot \left( \frac{dV_{output}}{dI_{total}} \right) \end{aligned} \quad (4)$$

Where:

- $\Delta I$  = change in total detector current (Amps)
- $\Delta V$  = change in median output voltage (volts)
- $\Delta i$  = average change in single pixel current (Amps)
- $N_e$  = number of electrons
- $\Delta Q_i$  = change in charge integrated for one pixel (coulombs)

In some of the data shown in later sections, the different irradiances were produced at different wavelengths, and due to the variation in source radiance and filter transmittances, different integration times were necessary. Thus, each output voltage was normalized to the appropriate integration time before plotting.

### 5.2.2 Mean Variance Method

If the pixel noise is dominated by photon noise, the mean-variance method can be used to determine the conversion gain. Equation 5 gives an expression for photon noise from a pixel. If this expression is squared and the expression for the quantity,  $\eta E_q A_{det} \tau_{int}$ , is substituted into the equation for pixel output voltage, we obtain Equation 6, the pixel variance (square of noise) as a function of pixel output voltage. Thus, the conversion gain is the slope of a plot of the variance versus the output voltage.

$$Noise_{photon} = C_g \sqrt{\eta E_q A_{det} \tau_{int}} \quad (\text{RMS Volts}) \quad (5)$$

$$Noise_{photon}^2 = C_g \bullet V_{Output} - C_g \left( \frac{C_g I_{dark} \tau_{int}}{q} \right) \text{ (Volts)}^2 \quad (6)$$

To obtain the conversion gain data, pixel output voltages and RMS noises are measured at a number of photon irradiances. The output level for each pixel is the average of the output for a number of consecutive frames and the noise is the RMS deviation of the output around its average value for the same number of frames. The variance is then plotted as a function of the output voltage and the conversion gain is determined. This process can be performed for individual pixels, but in practice, median outputs and variances are typically used.

### 5.3 Output and Responsivity

The pixel output voltage is a linear function of the photon irradiance (within the linear range of the ROIC) as given in Equation 2. The responsivity is equal to the slope of output versus irradiance as expressed in Equation 7. To obtain the VFPA responsivity, the values for detector area and integration time are used with Equation 7 and the measured slope of the output voltage versus photon irradiance. The VFPA responsivities are generally reported here at 650 nm.

$$\text{Responsivity} = C_g \eta = \frac{dV_{Output}}{d(E_q A_{det} \tau_{int})} = \frac{1}{A_{det} \tau_{int}} \frac{dV_{Output}}{d(E_q)} \left( \frac{\text{Volts}}{\text{photon}} \right) \quad (7)$$

Since all response data were obtained at the same integration time, the response reported below has not been normalized to detector area and integration time and the units used are volts/(ph/s-cm<sup>2</sup>).

One hundred (100) consecutive frames of data were used to determine the output used for responsivity. In the data section below, pixel output voltage data are presented as array medians versus irradiance and full array distributions. Pixel responsivities obtained from these data are similarly plotted. Additionally, the detector quantum efficiency can be determined from the responsivity and the measured conversion gain as shown in Equation 7.

Alternately, the responsivity can be determined at a fixed irradiance by changing the integration time if the dark current is *insignificant*. If the output is differentiated with respect to integration time instead of irradiance in Equation 7, we get Equation 8. This is the method used to determine responsivity at different wavelengths using the Spectra-Physics (SP) source because there was no method for changing the irradiance at a fixed wavelength was conveniently available.

$$\text{Responsivity} = \frac{1}{A_{det} E_q} \frac{dV_{Output}}{d(\tau_{int})} \left( \frac{\text{Volts}}{\text{photon}} \right) \quad (8)$$

As will be seen below, the dark current was not always small compared to the photocurrent and errors in responsivity were present when using this method. However, conclusions can still be drawn about the responsivity and how it varies with radiation.

## 5.4 Dark Current

Differentiating the expression for pixel output voltage (Equation 2) with respect to integration time yields:

$$\begin{aligned}\frac{d(V_{Output})}{d(\tau_{int})} &= C_g \eta E_q A_{det} + \frac{C_g I_{dark}}{q} \\ &= \frac{C_g}{q} \left[ (\eta q E_q A_{det}) + I_{dark} \right]\end{aligned}\quad (9)$$

The first term in the brackets is the pixel current due to the photon irradiance and the second is that due to dark current. Output voltage measurements were made as a function of integration time at very low photon irradiance, and these output data were plotted as a function of integration time. The dark current were then calculated from the slope of this plot and Equation 10, since all other parameters in this Equation are known.

$$I_{dark} (Amps) = \frac{q}{C_g} \frac{d(V_{Output})}{d(\tau_{int})} - \eta q E_q A_{det} \quad (10)$$

## 5.5 Noise

Pixel noise was calculated as the RMS deviation of the pixel output voltage about its average for one hundred (100) consecutive frames of data. The measured noise always includes contributions from both readout and detector, and detector noise can include contributions from photon noise, thermal noise, and other noises as described below. Pixel noise data are presented as array median values versus irradiance and full array distributions.

### 5.5.1 Read Noise

Read noise is determined by measuring the VFPA noise under conditions where it dominates. It is thus measured at low photon irradiances, where photon noise is low; at low temperatures, where dark current noise is low; and at short integration times where 1/f noise is low.

### 5.5.2 Detector Thermal Noise

Thermal noise is that noise due to the random generation of carriers due to the finite detector operating temperature. This noise obviously will be lower at lower temperatures. Detector thermal noise in RMS volts is calculated from the dark current as determined above (see Section 5.4) using Equation 11.

$$Noise_{Thermal} = C_g \sqrt{\frac{I_{dark} \tau_{int}}{q}} \quad (11)$$

### 5.5.3 Photon Noise

Photon noise is due to the random generation of carriers by the random arrival of photons. Photon noise is calculated from the FPA conversion gain and the detector quantum efficiency

using Equation 5.

#### 5.5.4 Total Noise

Any measured VFPA noise is made up of contributions from several sources. In general, it is the square root of the sum of the squares of: (1) readout noise, (2) photon noise, (3) dark current shot noise, and (4) other noises. The total noise can thus be written as:

$$Noise_{total} = \sqrt{Noise_{Readout}^2 + Noise_{photon}^2 + Noise_{Thermal}^2 + \dots} \quad (12)$$

By modeling each of these noise sources based on measured data, it is possible to determine which is the most significant for different combinations of operating temperature, integration time, and photon irradiance. When measuring noise, it is important that the noise of the measurement system is negligible. For all data shown here, the test system noise is not significant.

### 5.6 RAW Data Collection

To determine the transient response of the SCM1250 to gammas and protons, several consecutive frames of data were collected at different gamma and proton fluence rates. These data are reported as distributions of output and as 2-D images of single output frames.

#### 5.6.1 Gamma Radiation

The majority of the ionizing events produced by the gamma source in the detectors are due to interactions of secondary electrons produced in the Dewar and the mount structure near the VFPA. These electrons come from a variety of directions and are distributed in energy. The lowest gamma rate used, achieved when the Dewar was at the maximum distance from the source, was experimentally found to produce ionizing events in approximately 20% of the array pixels in each integration time. Data were also obtained at interaction probabilities, of approximately 40% and 100%, by moving the Dewar closer to the source.

#### 5.6.2 Proton Radiation

The proton fluence rates were chosen for data collection, based on Equation 13, to approximate interaction probabilities of 4, 8, and 16% with a pixel in one integration time. Note that these rates account for the 45-degree angle the detector surface makes with the proton beam, but do not account for interactions that protons can make with other pixels after passing through the first one. As shown in Figure 8, the protons can go through up to 3 pixels for SN #150, which is 110 microns thick, and up to 2 pixels for SN #157, which is 50 microns thick. Thus, actual event rates can be factors of 3 or 2 higher than calculated, respectively. The proton fluence rates used were:  $1.7 \times 10^5$ ,  $3.4 \times 10^5$ , and  $6.8 \times 10^5$  protons/s-cm<sup>2</sup>.

$$\text{Event Rate} \left( \frac{\text{events}}{\text{pixel} \cdot \text{frame}} \right) = \text{Fluence Rate} \left( \frac{\text{protons}}{\text{s-cm}^2} \right) \cdot \tau_{\text{int}}(\text{s}) \cdot \text{Pix Area}(\text{cm}^2) \cdot \cos(45^\circ) \quad (13)$$

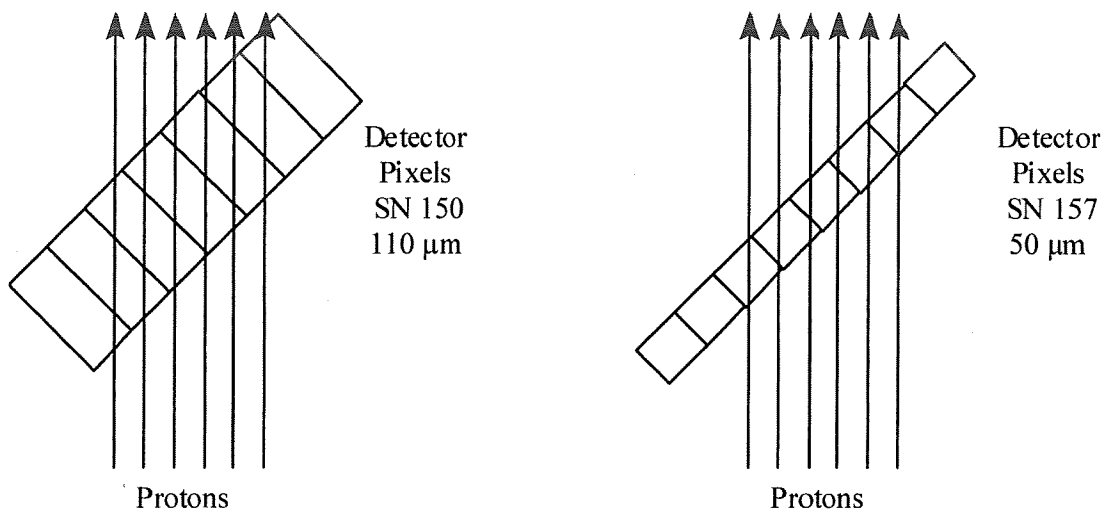


Figure 8. Geometry for Proton Beam Interaction with Detector Pixels



## 6 Characterization Data

Characterization data for each of the visible focal plane arrays (VFPAs) are given in this Section in the order in which the measurements were described in Section 4. The devices characterized during these tests are summarized in Table 2.

Part Number	Radiation Type	Thickness ( $\mu\text{m}$ )
SCM1250-155	$^{60}\text{Co}$ Gamma	50
SCM1250-154	$^{60}\text{Co}$ Gamma	50
SCM1250-150	Protons	110
SCM1250-157	Proton	50

Table 2. Summary of Devices Characterized

### 6.1 VFPA S/N 1250-155 Total Dose

RSC VFPA 1250-155 was characterized in a gamma environment produced by a cobalt-60 source located at the Air Force Research Laboratory, Albuquerque, NM. The VFPA was fully operational during all irradiations, and the temperature was maintained at  $-40^\circ\text{C}$  at all times.

#### 6.1.1 Diagnostic Measurements

The voltages on and the currents drawn in all readout nodes were measured as a function of total dose to determine the operational condition of the VFPA and the power dissipation.

#### 6.1.2 Conversion Gain

The readout conversion was determined as a function of total dose using the mean-variance method. Pixel output voltages and RMS noises were measured at a number of photon irradiances (at 650 nm) at each dose level and the square of the noise (variance) data is plotted as a function of the output voltage in Figure 9. These data can be fit with straight lines, indicative of shot noise limited operation, and the ROIC conversion gain at all doses, obtained as the slopes of these plots, is  $0.60 \mu\text{V}/\text{electron}$  (except at 300 krad(Si) where it is slightly lower). This value is close to values obtained on other programs.

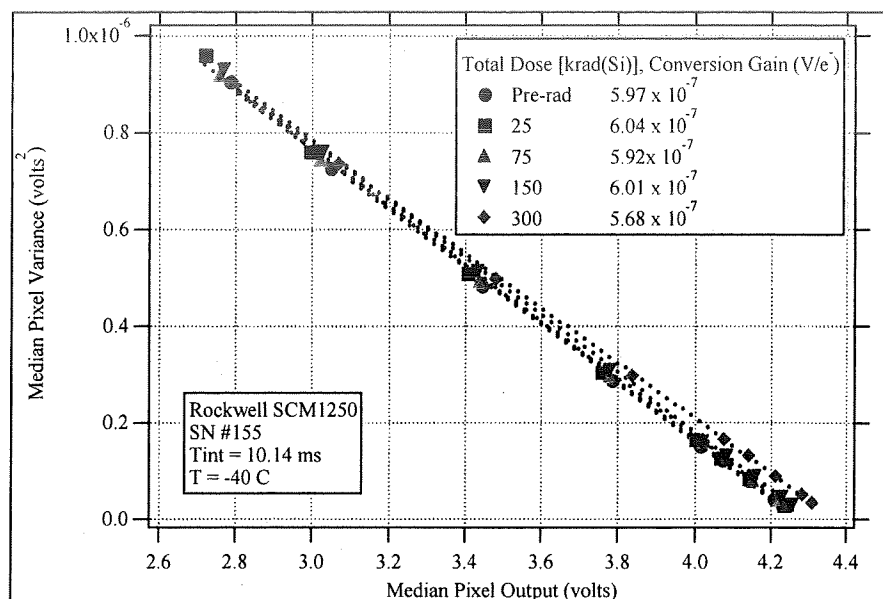


Figure 9. SN #155 Conversion Gain Data

### 6.1.3 Output

Pixel output voltage data, obtained as a function of photon irradiance, are described in this section. Data are also presented that describe the pixel output voltage as a function of the detector bias at various wavelengths.

#### 6.1.3.1 Responsivity

The median pixel output voltage is plotted as a function of photon irradiance (at 650) nm in Figure 10 and Figure 11. Figure 10 is a plot of the pre-radiation data, showing the linearity of the ROIC of better than 1% over most of the output voltage range. Similar output data at different total doses, plotted in Figure 11, show that the responsivity, as determined from the slopes of these plots, is relatively constant for the range doses studied. This result assures that neither the QE nor the conversion gain change with total dose.

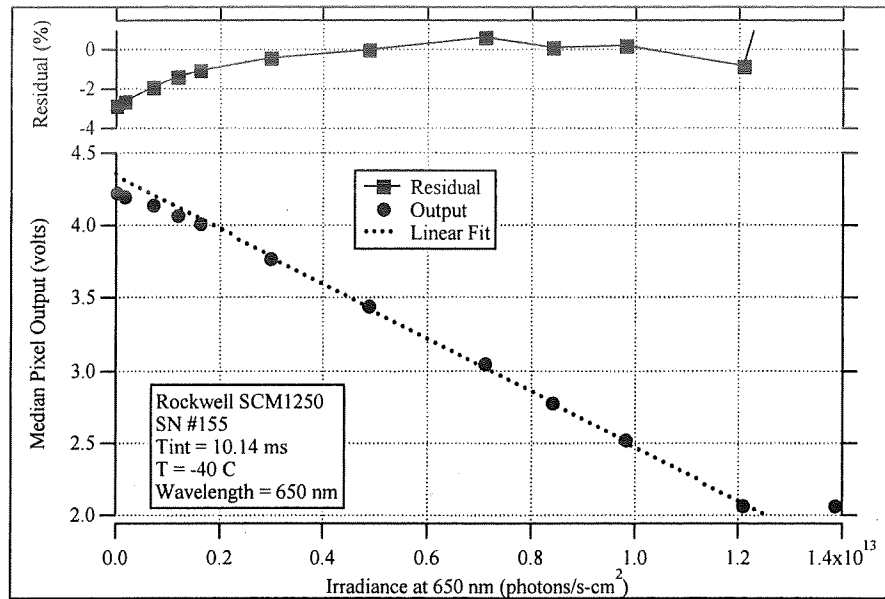


Figure 10. SN #155 Output versus Irradiance, Pre-rad

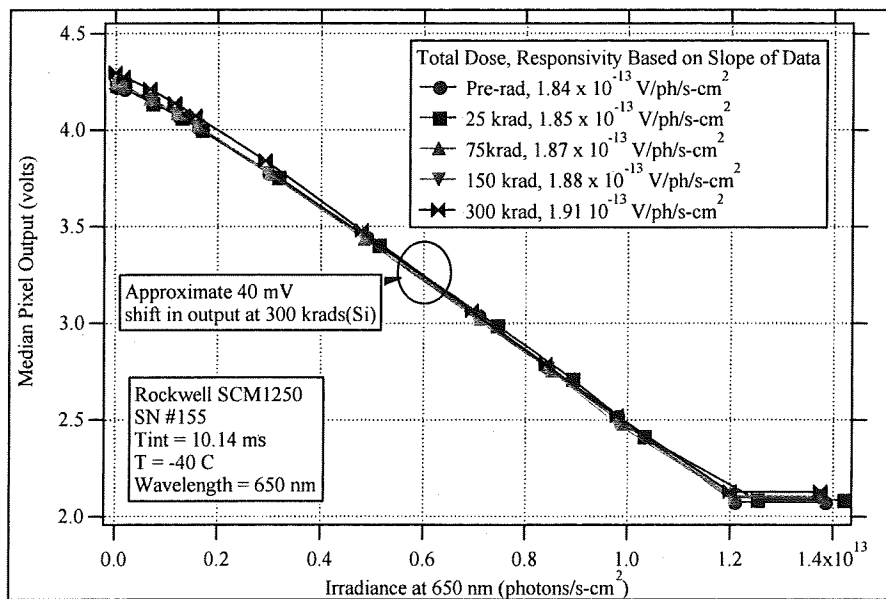


Figure 11. SN #155 Output versus Irradiance, Various Total Doses

Responsivity histograms obtained prior to radiation and at the maximum total dose are shown in Figure 12. These data, which were obtained from the difference in pixel outputs at two irradiances, show very little change in either the average or the very uniform distribution with dose.

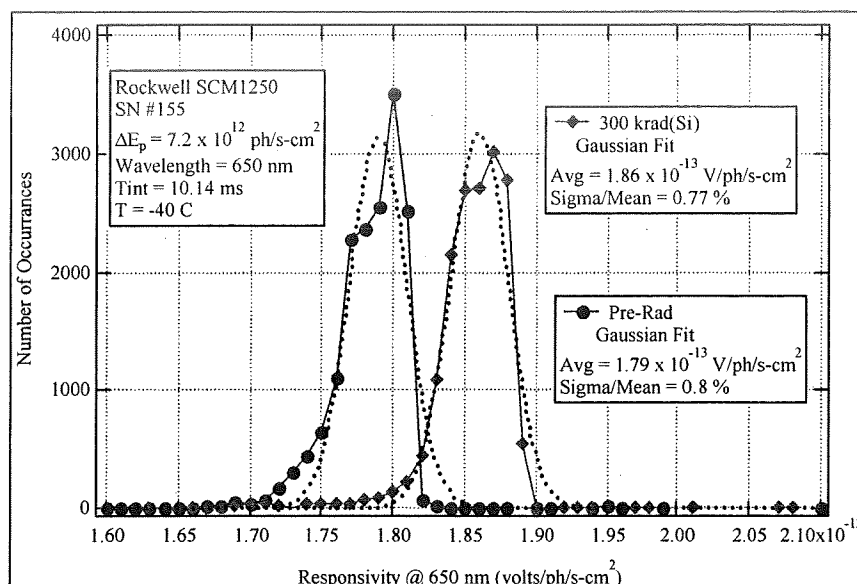


Figure 12. SN #155 Responsivity Histograms, Pre-Radiation and 300 krad(Si)

### 6.1.3.2 Response versus Bias

A major objective of these tests was to determine if the quantum efficiency (QE) of the PIN detectors changed with total dose, especially at very short UV wavelengths. If a change was to occur, it was expected that it would be due to a change in the degree of depletion of the detectors at a VSUB bias of 15 V. Thus, to determine if a change in depletion did occur, the response was measured as a function of VSUB bias, at several wavelengths, from 5 to 40 V as a function of total dose.

Prior to total dose radiation, the QE at each wavelength was found to be independent of VSUB bias (within experimental error) from 4 to 40 volts as shown in Figure 16. As the total dose increased, some loss in signal at lower biases was noted at some wavelengths as shown in Figure 14. Here the relative response versus bias at the final operational total dose of 300 krad(Si) is plotted.

These measurements were done at a fixed irradiance at each wavelength and the integration time was changed to determine the response. As is discussed in the section on dark current below (Section 6.1.4), the pixel dark current increased significantly with total dose and is was a strong function of the VSUB bias. While this dark was insignificant compared to the photo current at some wavelengths, it contributed in a measurable way to the total current and thus the responsivity, at other wavelengths. And since the dark current component was bias dependent while the photo current was not, those wavelength where the dark current was significant appear to have a responsivity that changes with bias as shown in Figure 14.

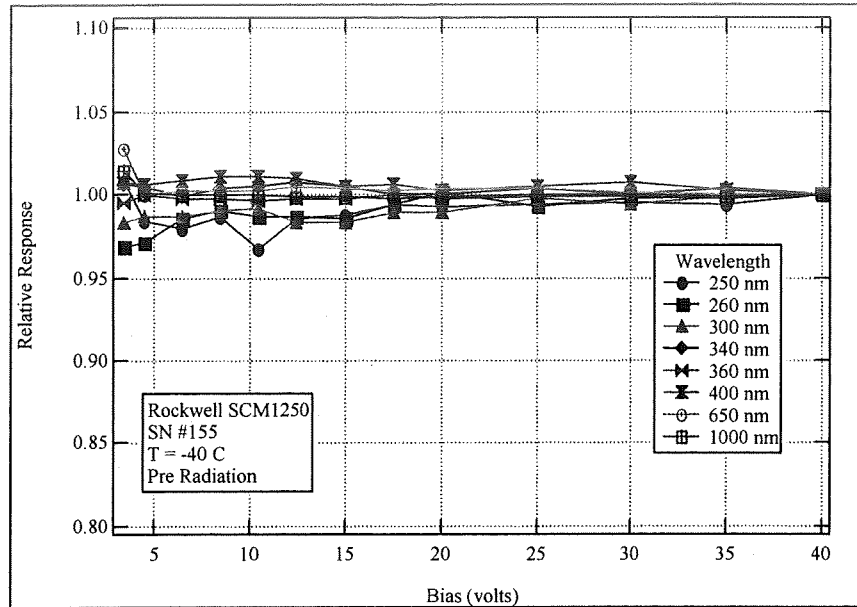


Figure 13. SN #155 Pre-Radiation Relative Response versus Bias

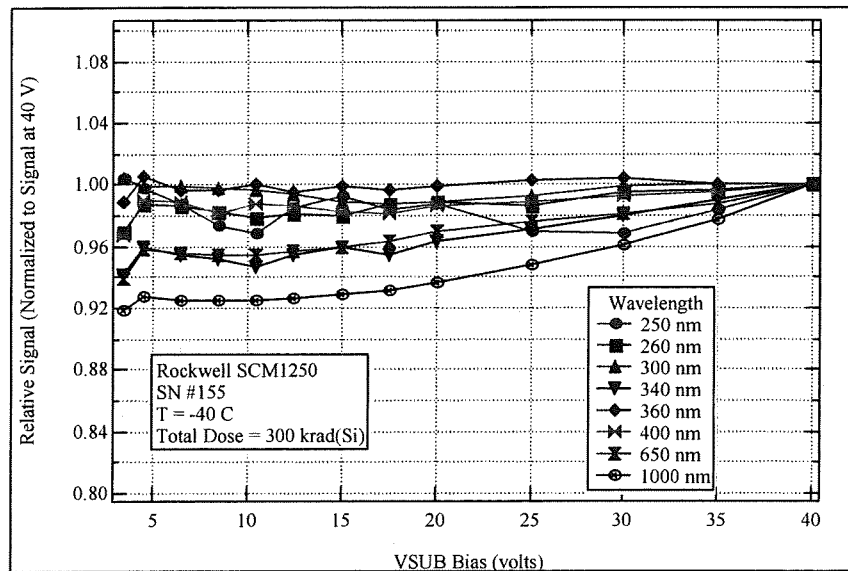


Figure 14. SN #155 Relative Response versus Bias at 300 krad(Si)

The response at 15 V, relative to that at 40 V, is shown as a function of wavelength in Figure along with the relative photocurrent measured in the VSUB bias line. [This current is a measure of the current produced by the irradiance from the optical source.] Note that those wavelengths with the lowest photocurrent are the ones with a higher percentage of dark current and are the ones that appear to have lowered response at 15 volts. Also note that one of these wavelengths with low photocurrent is 650 nm, and in the section on responsivity above (Section 6.1.3.1), it was shown that the responsivity at 650 nm, as measured by changing the irradiance, was constant

a function of total dose.

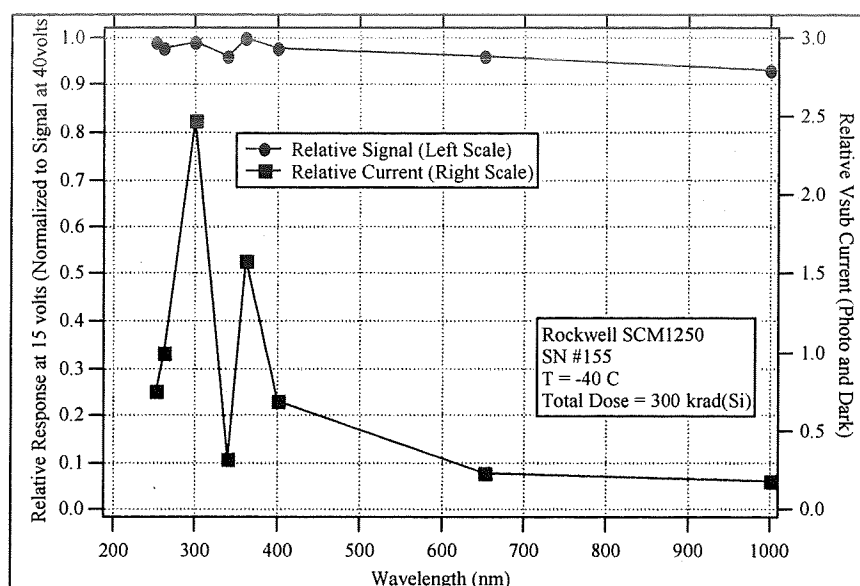


Figure 18. SN #155 Rel. Response and Relative Photo Current vs. Wavelength at 300 krad(Si)

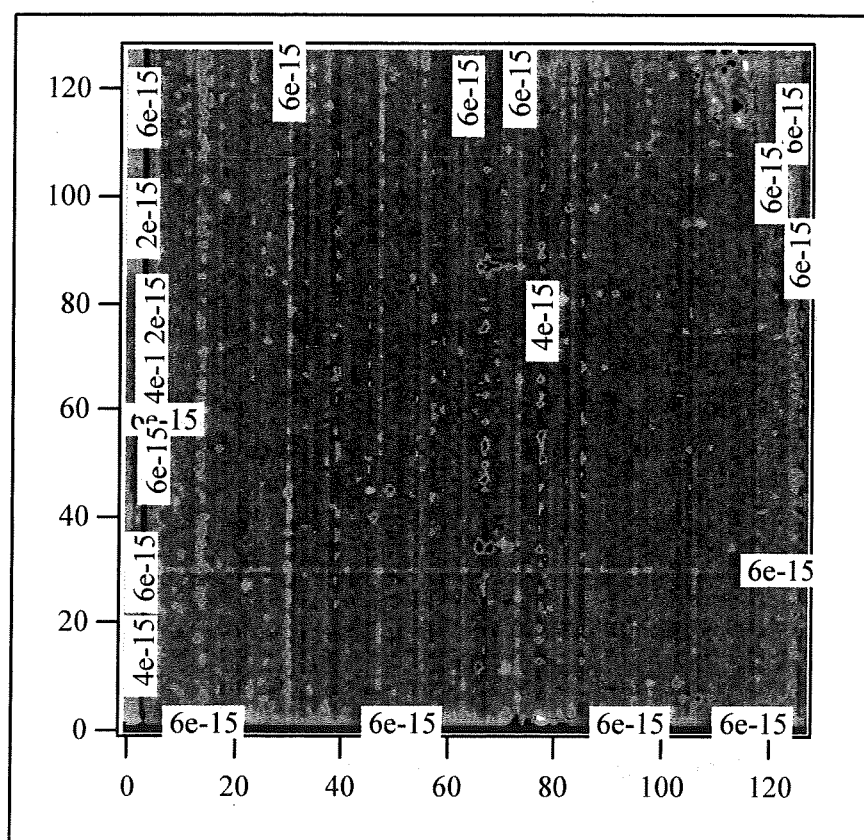
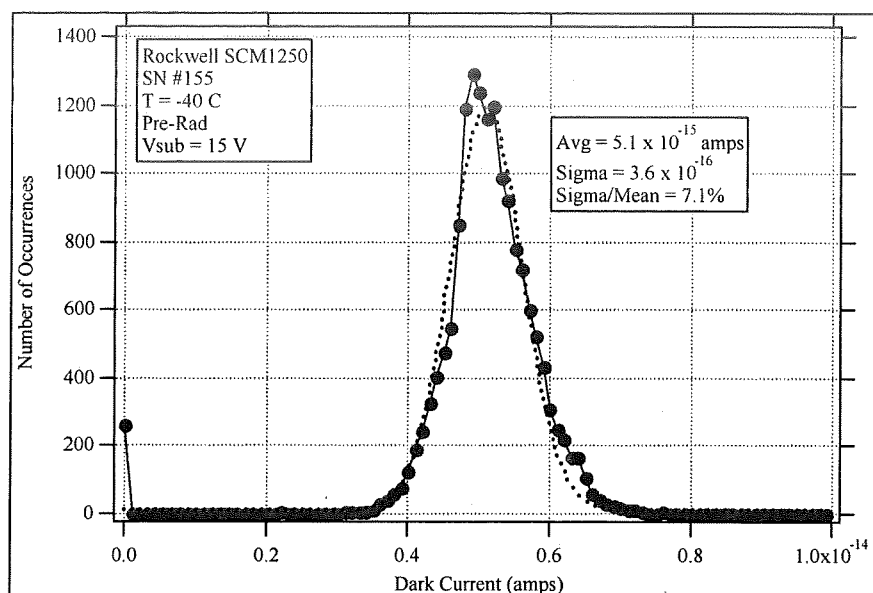
Thus, the conclusion can be drawn that the responsivity (and quantum efficiency, since the conversion gain was also shown to be constant with total dose) at all wavelengths does not change (within experimental error) as a function of total dose.

#### 6.1.4 Dark Current

Pixel dark currents were determined by measuring the output of the VFPA at several integration times, at very low photon irradiance, as a function of total dose. Data were obtained at several integration times to insure the measured output data were linear with integration time, and the dark current was determined from the slope of these data and the readout conversion gain.

A histogram of the pre-radiation dark current distribution is shown in Figure 14 and a 2-D map of these data is shown in Figure 15. The dark current is quite uniform, being slightly higher around the perimeter and in the upper right hand corner. There are also one column and one row that were not operational for this measurement.

The median pixel dark current versus total dose, plotted in Figure 16, shows that the dark current increases slightly more than 2 orders of magnitude from pre-rad to the maximum dose, 300 krad(Si), at a rate proportional to total dose to the 1.85 power. At doses of 150 krad(Si) and above, the dark current was measured as a function of detector bias (V<sub>SUB</sub> voltage) to obtain additional data to help find the origin of the dark current. These measurements are shown in Figure 17. Note that the current varies approximately as V<sub>SUB</sub> squared. Again this is an unexpected result since the optical response is NOT a function of bias. These data thus suggest that the origin of the dark current is not in the detector bulk but rather on the detector surface. Since the detector surface was passivated with SiO<sub>2</sub> and total dose effects are typically associated with trapped charge in dielectrics, this conclusion is consistent with those effects.



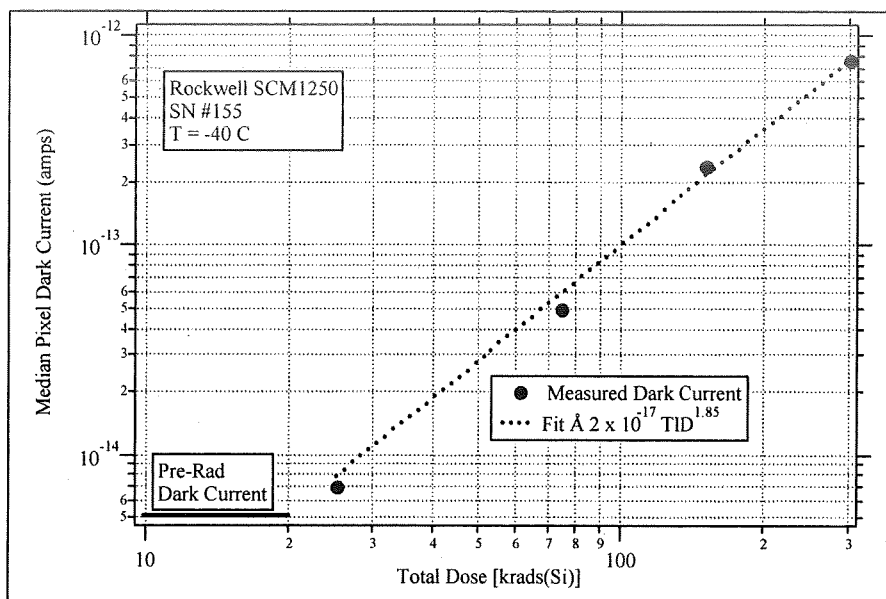


Figure 16. SN #155 Median Dark Current versus Total Dose

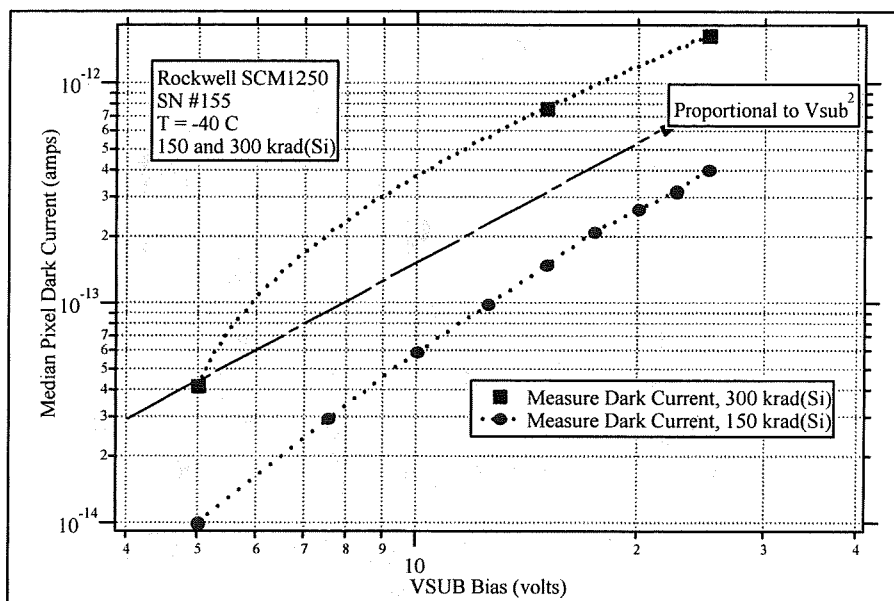


Figure 17. SN #155 Median Dark Current versus VSUB at 150 and 300 krad(Si)

The distribution of pixel dark currents at a dose of 300 krad(Si) is shown in Figure 18, and the associated 2-D map is shown in Figure 19. The dark current at this dose is decidedly non-uniform, being higher around the perimeter than in the center. It is these perimeter pixels that are responsible for high current to the right of the distribution in Figure 18. In order to see this non-uniformity more clearly, a plot of the dark current of the pixels in row 64 (middle of the array) is plotted at all total dose levels in Figure 20.



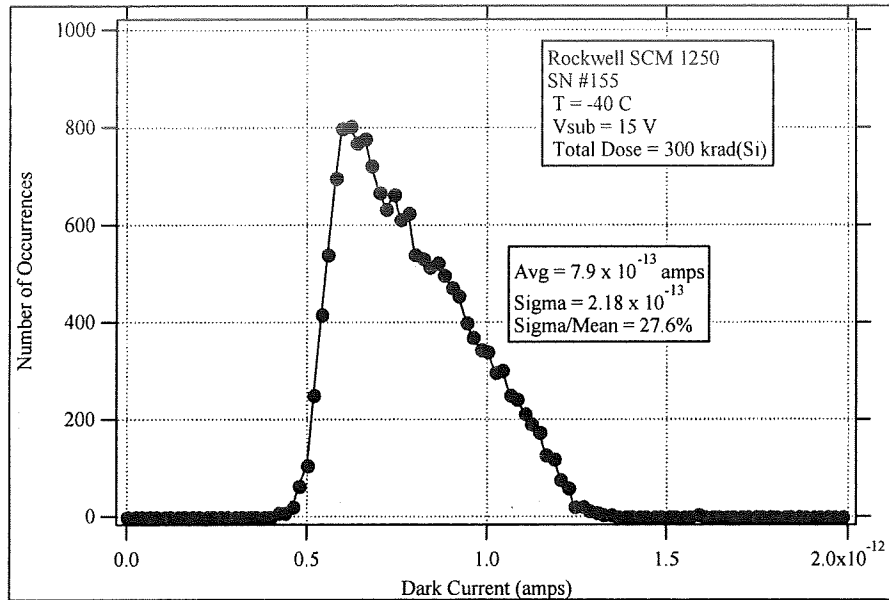


Figure 18. SN #155 Dark Current Histogram at 300 krad(Si)

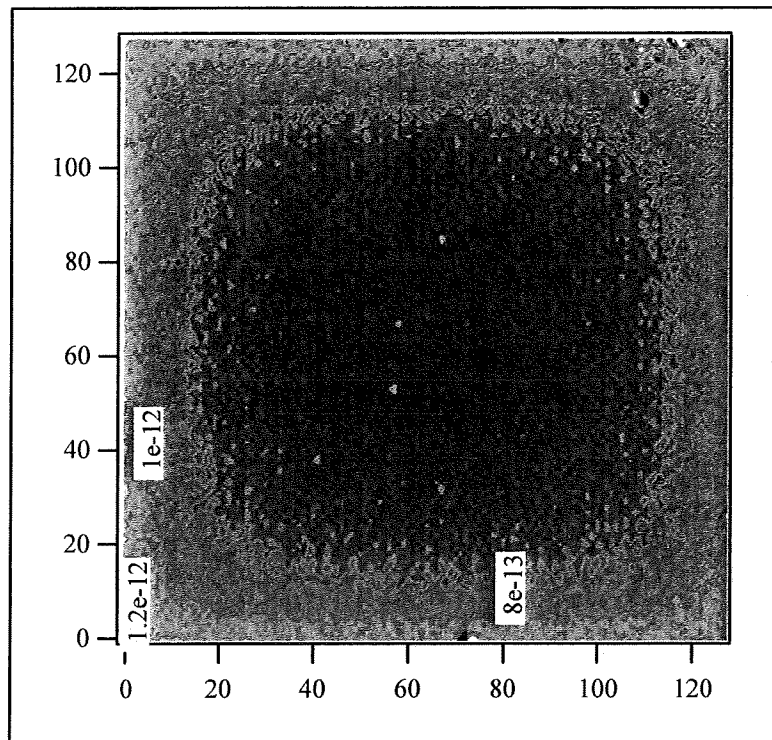


Figure 19. SN #155 Dark Current Map at 300 krad(Si)

These data show that the perimeter pixels have higher dark current at all total dose levels. This non-uniformity could be due to poor thermal contact between the VFPA and the chip carrier. Another reason could be stress in the detectors created when the detector chip was bonded to the readout chip. Rockwell saw this non-uniformity in pre-radiation dark current on some devices, but thought it had been solved. In the section below on SN #154, significantly more bias data

were obtained, and these data suggest that the non-uniformity is due to a bias difference between center and edge pixels caused by a voltage drop across the pixel common lead.

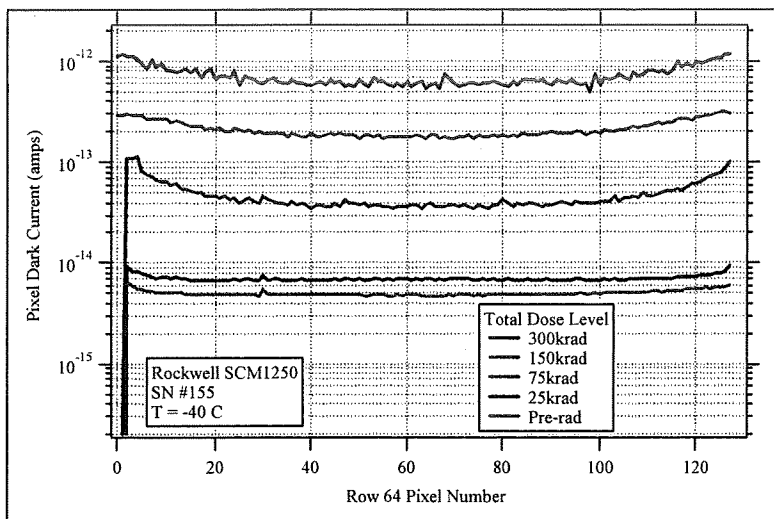


Figure 20. SN #155 Dark Current of Pixels in Row 64 At All Total Dose Levels

### 6.1.5 Noise

Pre-Radiation median pixel noise data are shown as a function of irradiance in Figure 21. Also shown in this figure are plots of photon noise, based on a quantum efficiency of 0.7 and a conversion gain of  $0.6 \times 10^{-6}$  V/e, and read noise, 0.12 mV. These two noises were RSS'd together to obtain the total noise, which is a good fit to the measured data. There is some increase in the measured noise as the readout approaches saturation, but the noise basically has two terms, readout noise and photon noise. Noise data at all total dose levels are shown in Figure 22, and little change in median noise is noted with total dose. Histograms of noise at an irradiance of approximately  $4.8 \times 10^{12}$  ph/s-cm<sup>2</sup> for pre-radiation and at the maximum dose are shown in Figure . Both distributions are quite uniform and essentially identical. Thus, under these conditions up to a total dose of 300 krad(Si), the dark current is insignificant.

### 6.1.6 Transient Data

Histograms of pixel outputs for 50 frames of data collected from one forth of the pixels in the VFPA at three different gamma flux rates are shown in Figure . An optical flux was placed on the VFPA for these measurements to insure that the readout was operating in its linear range. The output data for these histograms was obtained by subtracting frames with gammas from frames without gammas; thus they are deviations from zero. The bottom axis is in test system A/D counts (1 count = 160 micro-volts) and the upper scale is in volts. The lowest gamma rate was achieved by placing the Dewar containing VFPA at the greatest distance from the cobalt-60 source, and the other rates are approximately increases of factors of two achieved by moving the Dewar closer to the source. At the lowest gamma flux rate, 200 frames of data were collected from every pixel in the array and a histogram of these data is shown in Figure .

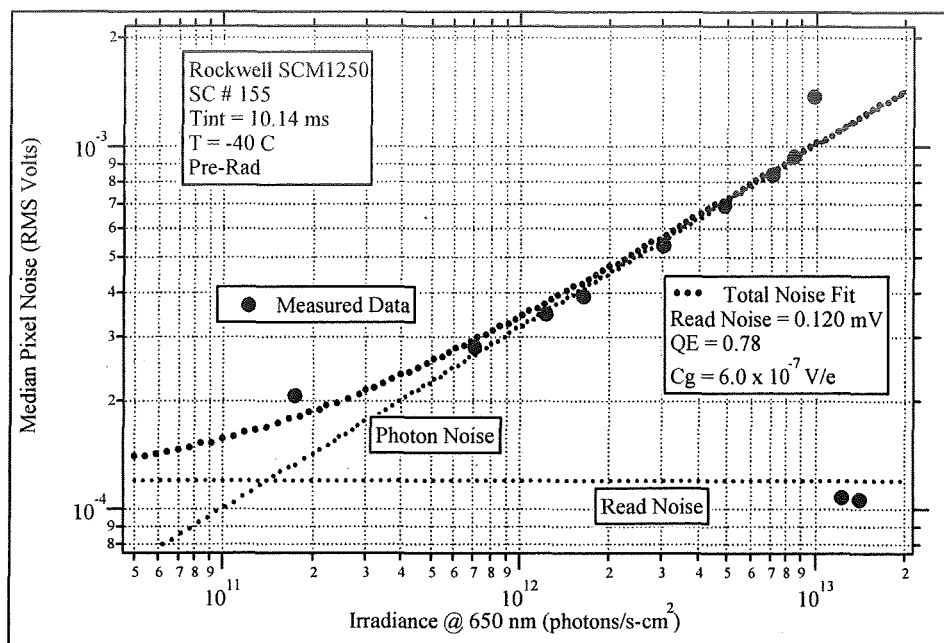


Figure 21. SN #155 Pre-Radiation Noise versus Irradiance

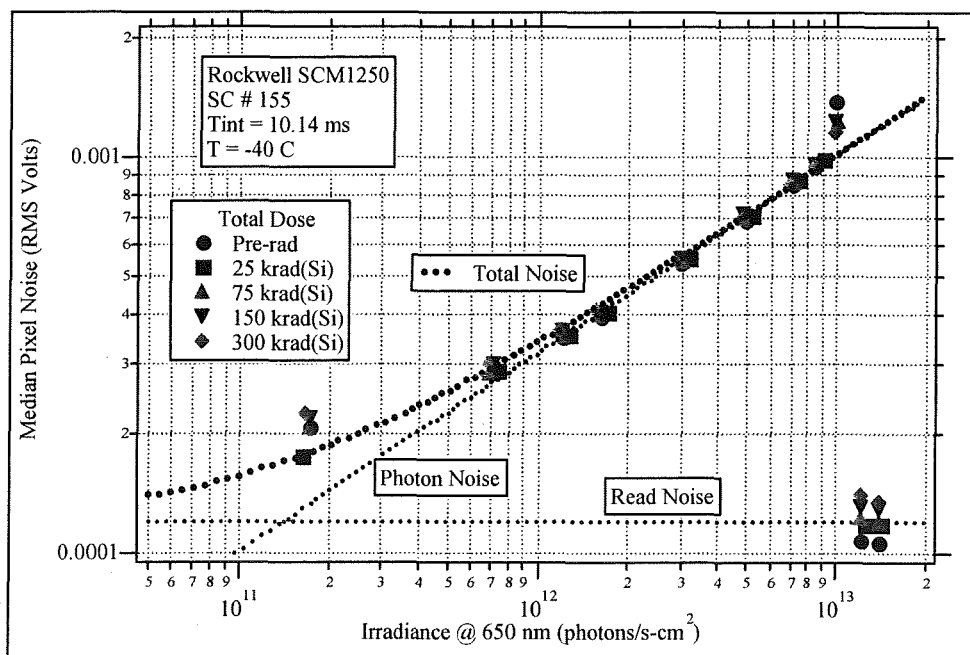


Figure 22. SN #155 Noise versus Irradiance at All Dose Levels

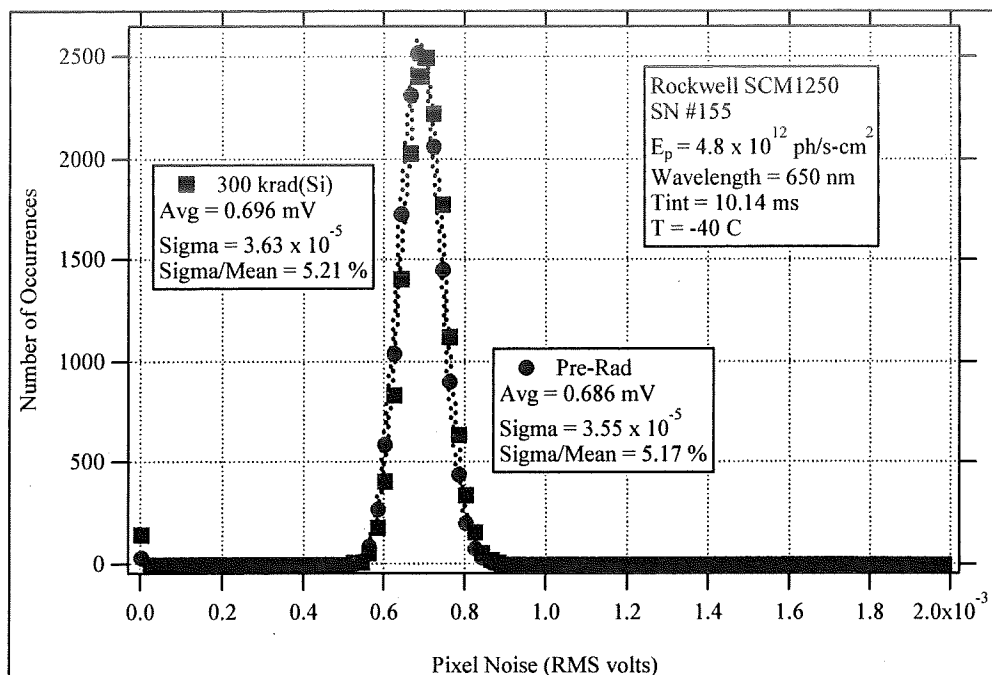


Figure 28. SN #155 Noise Histograms at  $4.8 \times 10^{12} \text{ p/s-cm}^2$ , Pre-Rad and 300 krad(Si)

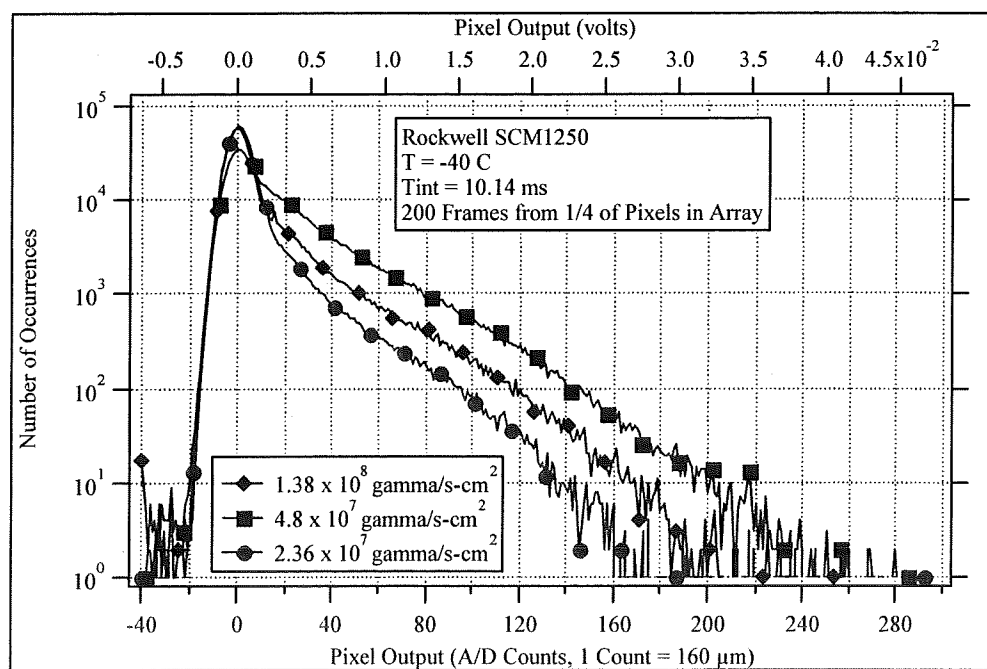


Figure 29. SN #155 Pixel Output Distributions at Three Ionizing Event Rates

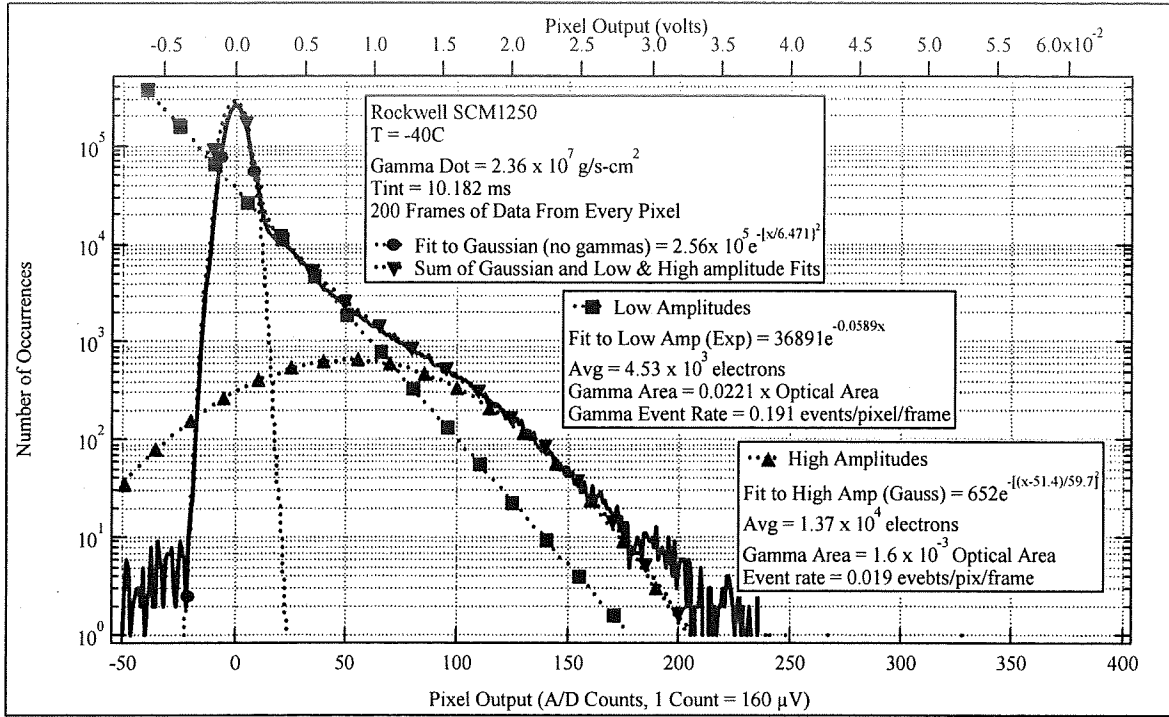


Figure 30 SN #155 Pixel Output Distributions at Lowest Gamma Flux Rate

Because of the significant amount of data collected in 200 frames from 16,384 pixels, the output histogram clearly shows three different regions. The first region is a Gaussian, centered on zero, which contains outputs from those pixels without ionizing events. Immediately to the right of the Gaussian is an exponential distribution of the form:

$$N = N_0 e^{-\alpha x} \quad (14)$$

where  $N$  = Number of Occurrences at output  $x$   
 $N_0$  = Number of Occurrences at  $x = 0$   
 $\alpha$  = Exponential constant

From this expression, the average value for  $x$  and the total number of occurrences for the exponential expression can be obtained from:

$$X_{average} = \frac{N_0 \int x e^{-\alpha x}}{N_0 \int e^{-\alpha x}} = \frac{1}{\alpha} \quad (15)$$

$$Total \ Number \ of \ Events = N_0 \int e^{-\alpha x} = \frac{N_0}{\alpha}$$

From the fit to the exponential part of the distribution, we obtain an average ionizing event of

$4.53 \times 10^3$  electrons (based on a conversion gain of  $0.6 \times 10^{-6}$  V/e) and a total number of ionizing events of  $6.26 \times 10^6$ . Based on 200 frames at an integration time of 10.182 ms at a gamma flux rate of  $2.36 \times 10^7$  gammas/s-cm<sup>2</sup>, the total number of gammas incident on the VFPA is  $2.83 \times 10^7$ . Thus, the ionization event rate is 0.191 events/pixel/frame, and the effective gamma area is  $6.26 \times 10^6 / 2.83 \times 10^7 = 0.022$  times the optical area. This event rate is somewhat higher than is desirable to insure that no more than one event occurs in each pixel per frame, but it was the lowest gamma dose rate achievable.

The remaining part of the distribution can be fit with another Gaussian centered on 59.7 counts, corresponding to an average ionizing event of  $1.37 \times 10^4$  electrons, a factor of 3 larger than the average for the exponential distribution. The event rate for this distribution is a factor of 10 lower than that of the exponential distribution. If the three distributions are added together, the resultant distribution fits the actual data quite well as shown in Figure .

Individual frames of output at the three gamma dose rates are shown in Figure 23, Figure 24, and Figure 25. During the collection of these data, there was some problem without the readout, which was not known at the time. As is seen in these three figures, the lower 1/4 of the array was not being read out correctly. This problem was isolated to these data collections and was not observed in any of the other data.

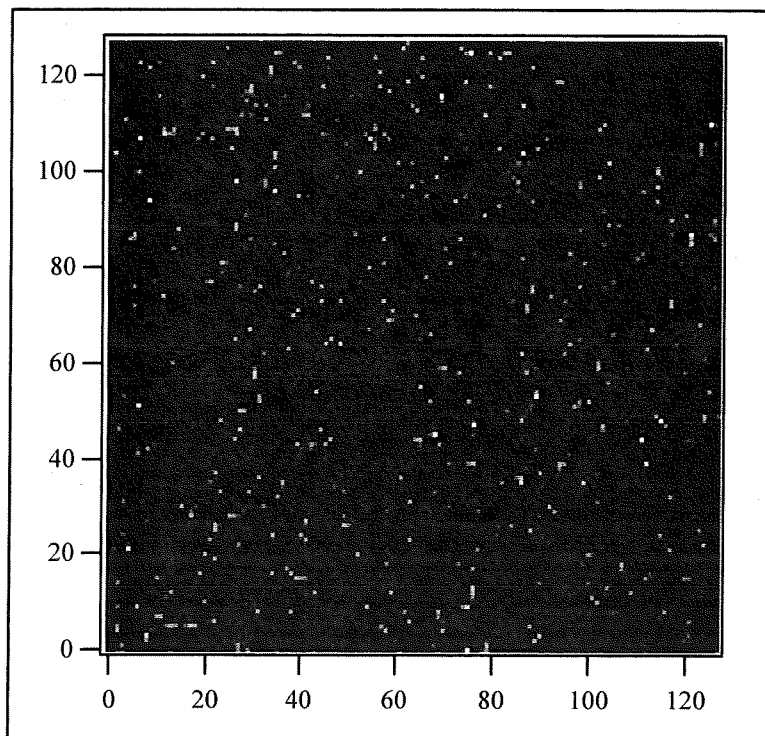


Figure 23. SN #155 One Output Frame at  $2.36 \times 10^7$  gammas/s-cm<sup>2</sup>

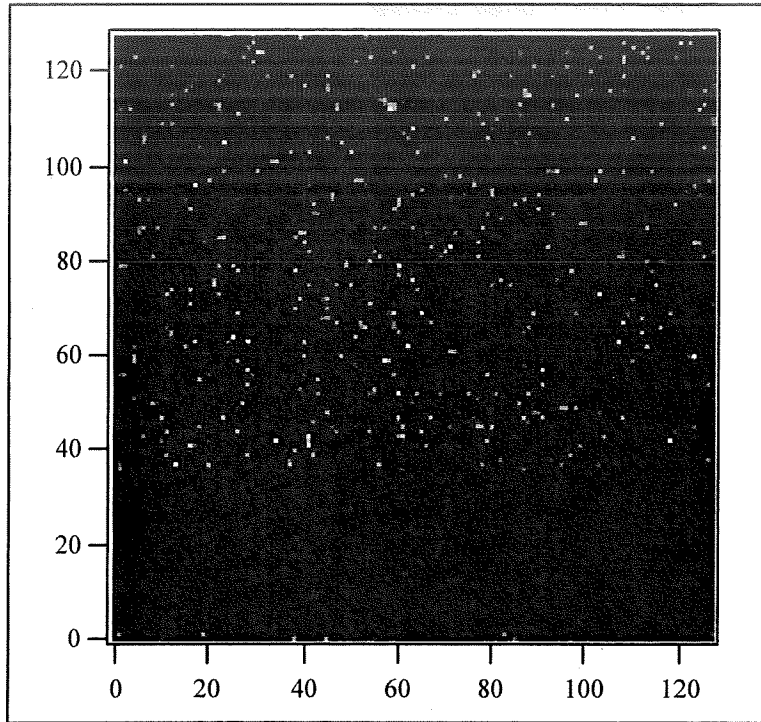


Figure 24. SN #155 One Output Frame at  $4.8 \times 10^7$  gammas/s-cm<sup>2</sup>

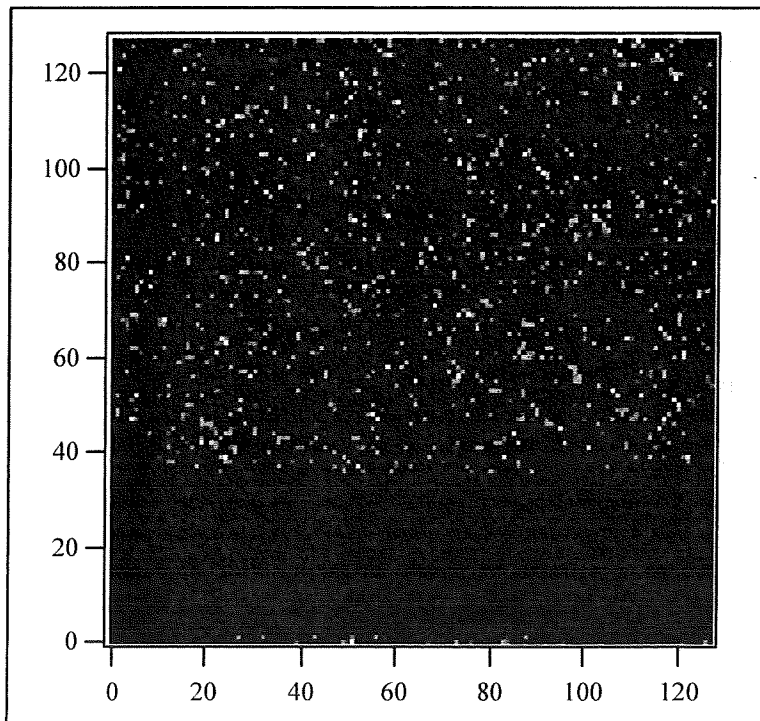


Figure 25. SN #155 One Output Frame at  $1.38 \times 10^8$  gammas/s-cm<sup>2</sup>

## **6.2 VFPA S/N 1250-154 Total Dose**

RSC VFPA 1250-154 was characterized in a gamma environment produced by a cobalt-60 source located at the Air Force Research Laboratory, Albuquerque, NM. The VFPA was fully operational during all irradiations, and the temperature was maintained at -40 C at all times. Some measurements were also made after 1 week of annealing at -40 C after the last dose. These annealing data are shown at the end of the other data.

### **6.2.1 Diagnostic Measurements**

The voltages on and the currents drawn in all readout nodes were measured as functions of total dose to determine the operational condition of the VFPA.

### **6.2.2 Conversion Gain**

The readout conversion was determined as a function of total dose using the mean-variance method.

### **6.2.3 Output**

Pixel output voltage data, obtained as a function of photon irradiance, are described in this section. Data are also presented that describe the pixel output voltage as a function of the detector bias at various total dose levels.

#### **6.2.3.1 Responsivity**

The median pixel output voltage is plotted as a function of photon irradiance (at 650) nm in Figure 26 and Figure 27. Figure 26 is a plot of pre-radiation data, showing the linearity of the ROIC of better than 1% over most of the output voltage range. Similar output data at different total dose levels is plotted in Figure 27. There is some variation in the responsivities as determined from the slope of these data that has been traced to a problem in aligning the Dewar with the visible source. Despite this problem, it is thought that the responsivity is constant with total dose. Since the conversion gain was also constant with total dose, this conclusion implies that the quantum efficiency does not change with total dose at 650 nm.

The problem with alignment is illustrated in Figure 28, where responsivity histograms at various total doses are plotted. These data were obtained from the difference in pixel outputs at two irradiances. The broadness of the pre-rad data clearly shows the misalignment and the 50 krad(Si) data are also not aligned well. However, responsivity data at 100 krad(Si) and above appear to be fairly well aligned with closely grouped responsivities. Responsivity histograms at 100 and 750 krad(Si), plotted in Figure along with statistics obtained from Gaussian fits to the data, show again that the very uniform responsivity did not change with total dose.



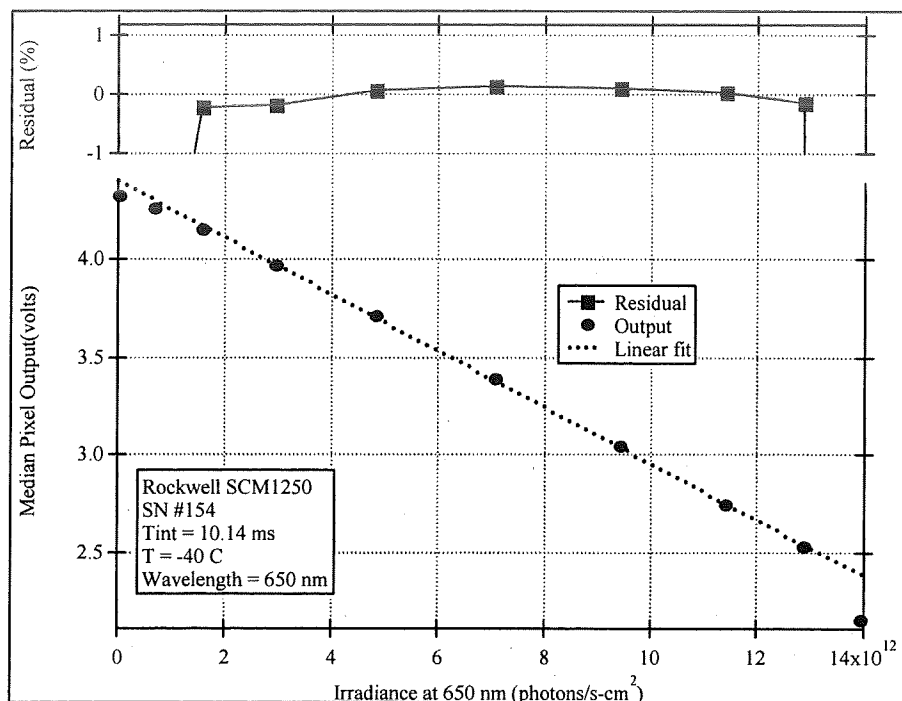


Figure 26. SN #154 Output versus Irradiance, Pre-Rad

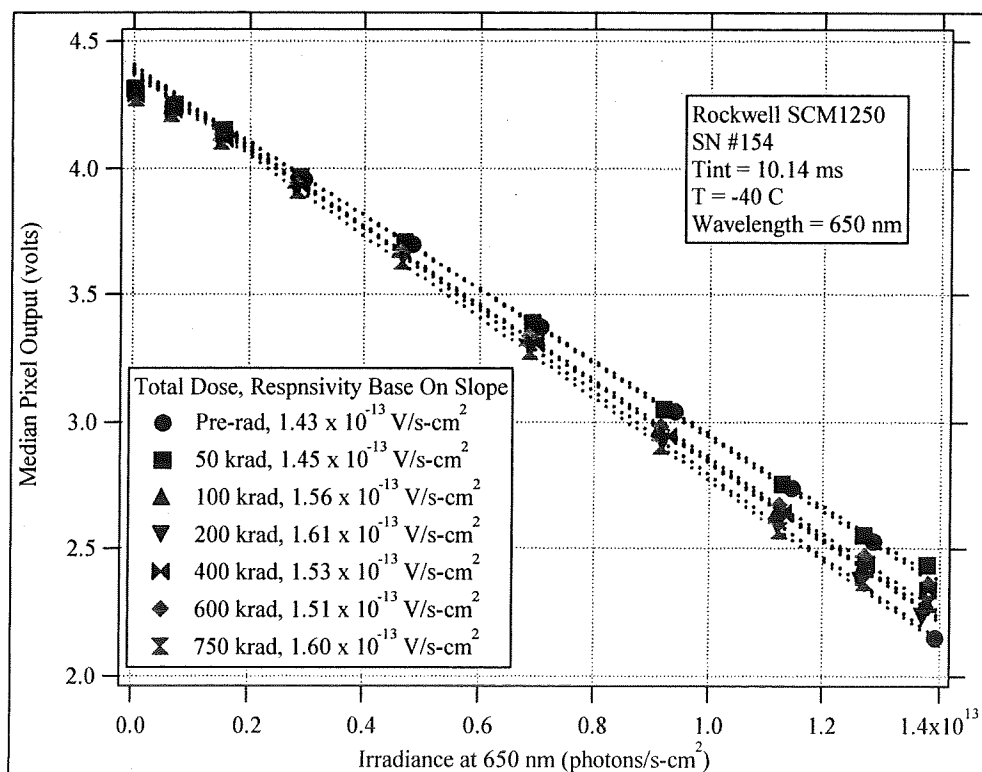


Figure 27. SN #154 Output versus Irradiance, Various Total doses

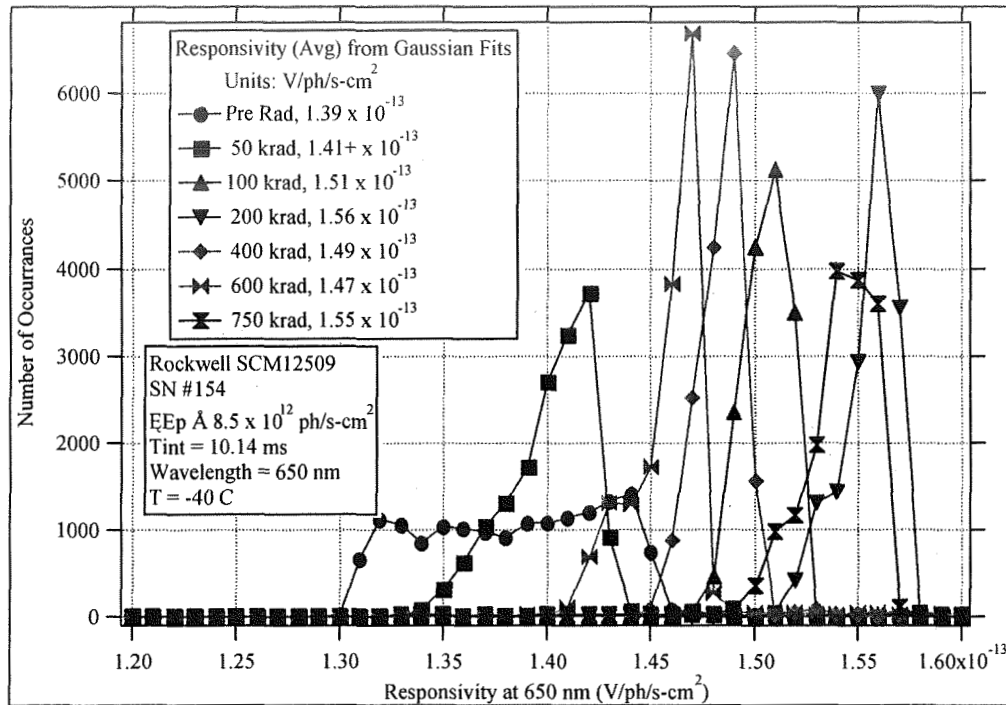


Figure 28. SN #154 Histograms of Responsivity at Various Total Doses

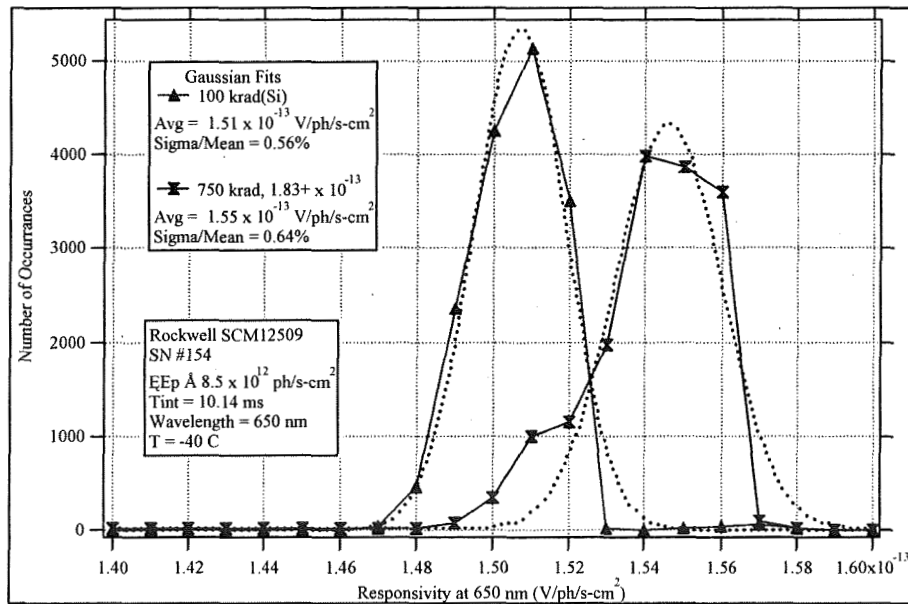


Figure 37. SN #154 Histograms of Responsivity at 100 and 750 krad(Si)

### 6.2.3.2 Response versus Bias

A major objective of these tests was to determine if the quantum efficiency (QE) of the PIN detectors changed with total dose, especially at very short UV wavelengths. If a change was to occur, it was expected that the cause would be a change in the degree of depletion of the detectors at a VSUB bias of 15 V. Thus, the response was monitored as a function of bias, at

several wavelengths, from 5 to 40 V as a function of total dose to determine if a change in depletion did occur. Additionally, the median response, at a VSUB voltage of 15 volts, was measured at all total dose levels.

Prior to total dose radiation, the QE at each wavelength was found to be independent of VSUB bias (within experimental error) at all wavelengths from 4 to 40 volts as shown in Figure . The normalized response at a VSUB voltage of 15 V is shown as a function of total dose in Figure . These data, which have been normalized to the average over all total doses, show no particular decrease or increase with dose, but rather a randomness of approximately  $\pm 10\%$  due to problems with the repeatability of the optical alignment. Response data at the shortest wavelength, 250 nm, is shown as a function of bias at total doses at 200 krad(Si) and above in Figure 29. The data below 200 krad(Si) was found to be above theoretical limits due to some unknown experimental problem and these data were deleted from the data set. The apparent increase in responsivity at high voltages and high total doses is due to an increase in dark current and the methodology used to measure the responsivity. For these data, the irradiance was fixed and the integration time was varied to determine responsivity. Thus, dark current that is comparable to the photocurrent will contribute to the measured responsivity. The fact that the dark current is a function of VSUB voltage also contributes to the functionality of the data with respect to VSUB voltage. [See later section on dark current.]

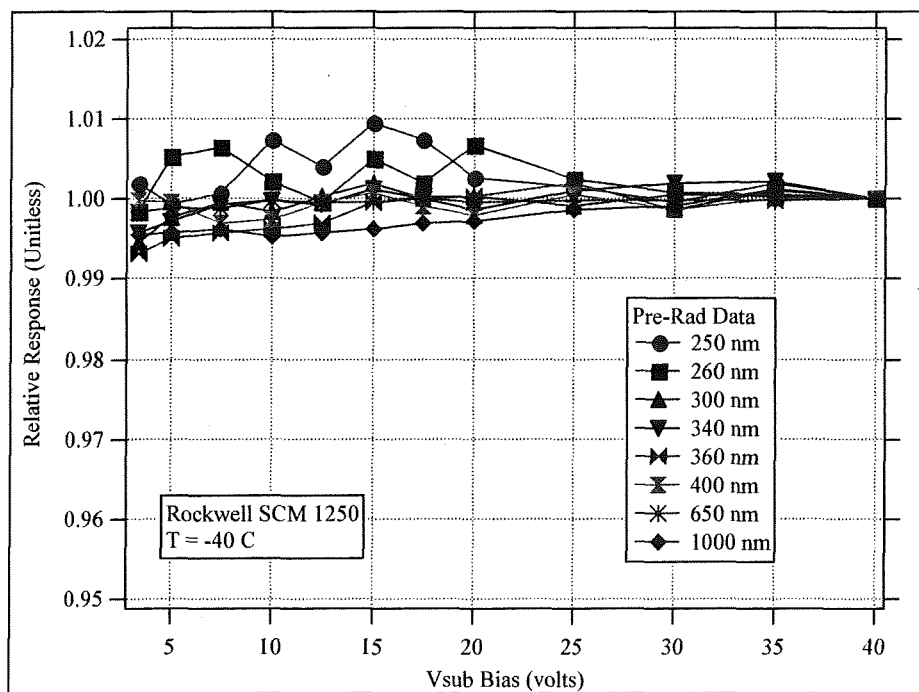


Figure 38. SN #154 Relative Response versus VSUB Bias, Pre-Rad

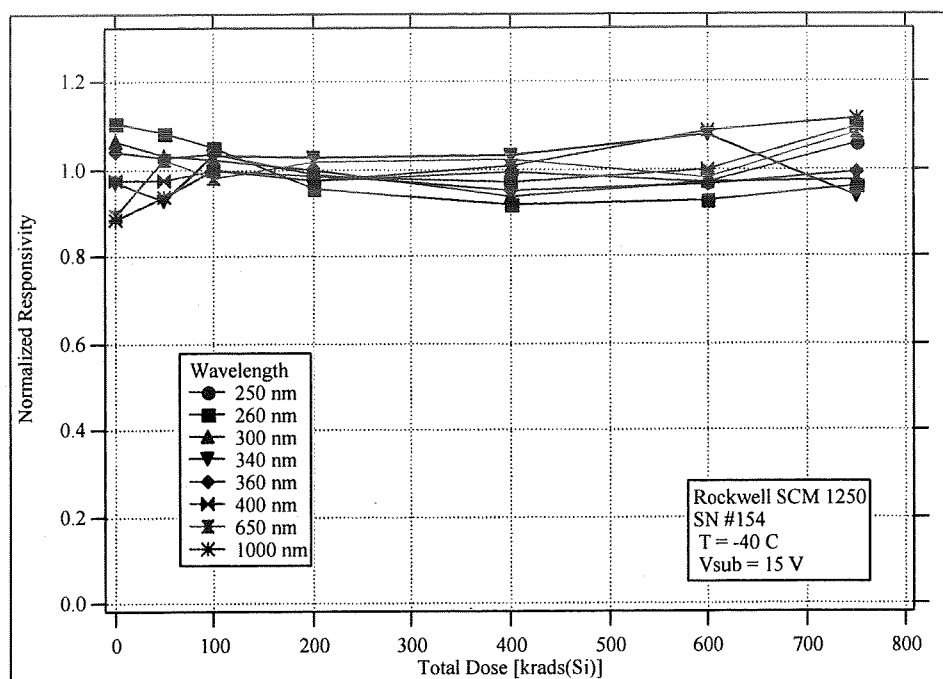


Figure 39. SN #154 Normalized Response versus Total Dose at VSUB = 15 V

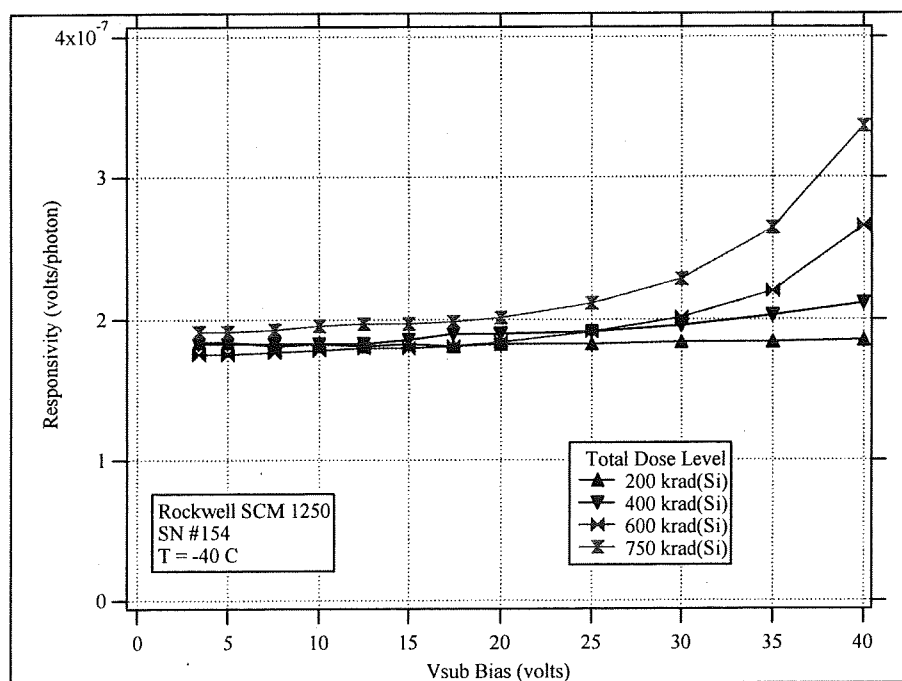


Figure 29. SN #154 Response at 250 nm versus VSUB Bias, Various Total Doses

## 6.2.4 Dark Current

Pixel dark currents were determined by measuring the output of the VFPA at several integration times, at very low photon irradiance, as a function of total dose. Data were obtained at several

integration times to insure the measured output data were linear with integration, and the dark current was determined from the slope of these data and the readout conversion gain.

Plots of the pre-radiation median dark current at various VSUB voltages as functions of  $1000/T$  is shown in Figure 30. All of these plots are parallel and the energy gap determined from the slope is consistent with a visible silicon detector. A histogram of the pre-radiation dark current distribution at the nominal VSUB voltage of 15 V is shown in Figure 31, and a 2-D map of these data is shown in Figure 32. The dark current is quite uniform with a slight minimum near the center of the array. Dark current histograms at 200, 400, 600, and 750 krad(Si) are shown in 44- Figure for a VSUB voltage of 15 V; the corresponding dark current maps are shown in Figure - Figure 37. These data show that the dark current increases with total dose and that the current around the edges increases faster than in the center of the array.

This spatial non-uniformity is further illustrated in Figure 38, where the dark current for the pixels in row 64, across the center of the array, is plotted at all total dose levels. These data show that the non-uniformity is present prior to radiation, but the difference in current between pixels near the edge and in the center is very small.

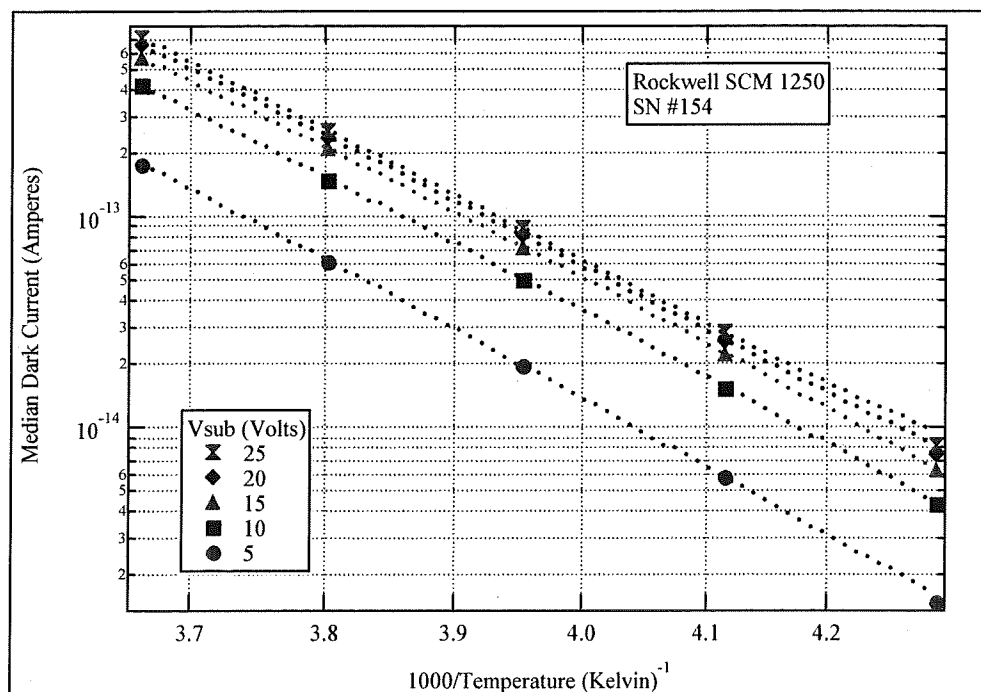


Figure 30. SN #154 Median Dark Current versus  $1000/T$ , Pre-Radiation

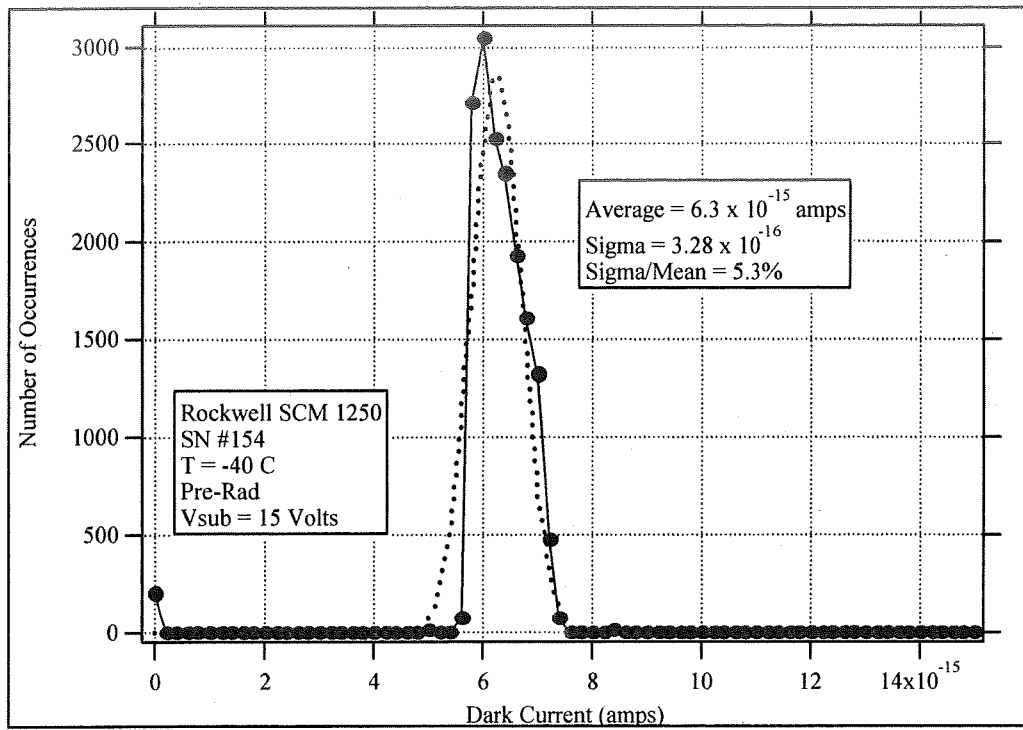


Figure 31. SN #154 Pre-Radiation Histogram of Dark Current

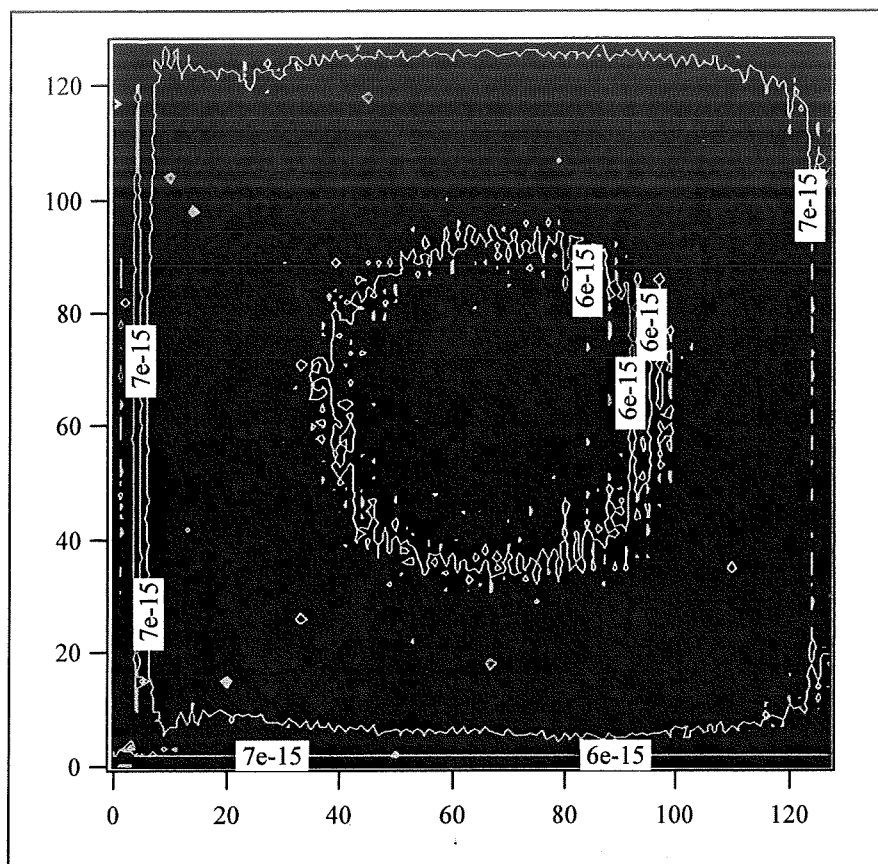


Figure 32. SN #154 Pre-Radiation Dark Current Map

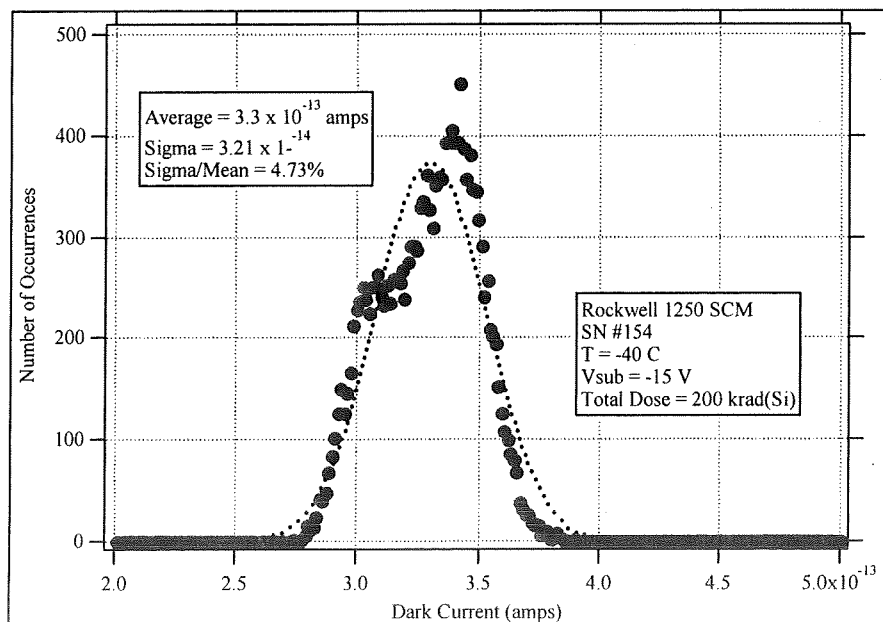


Figure 33. SN #154 Dark Current Histogram, 200 krad(Si)

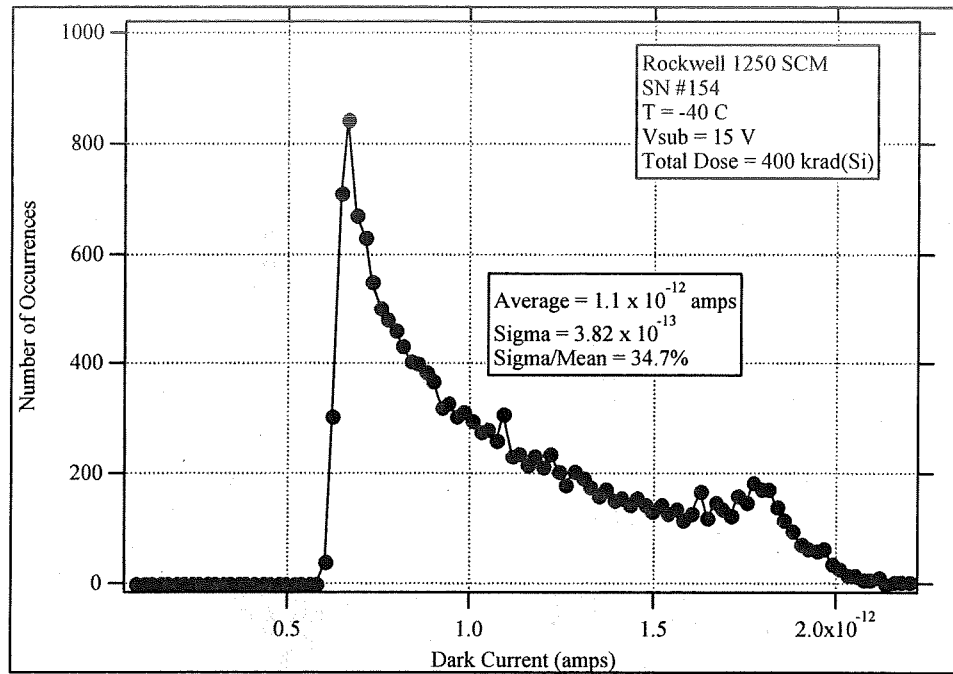


Figure 34. SN #154 Dark Current Histogram, 400 krad(Si)

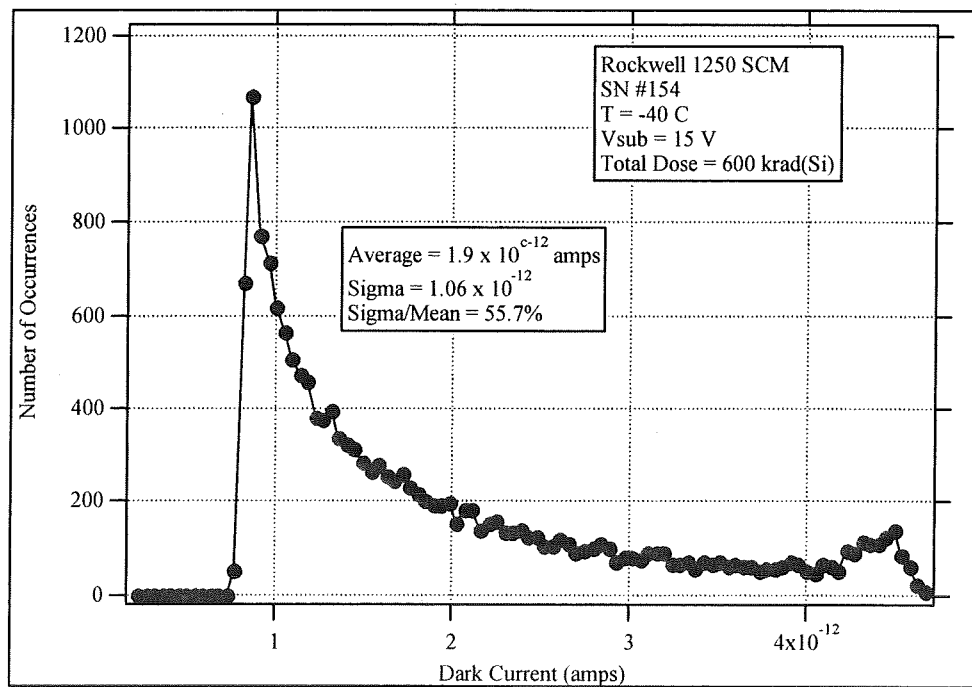


Figure 35. SN #154 Dark Current Histogram, 600 krad(Si)



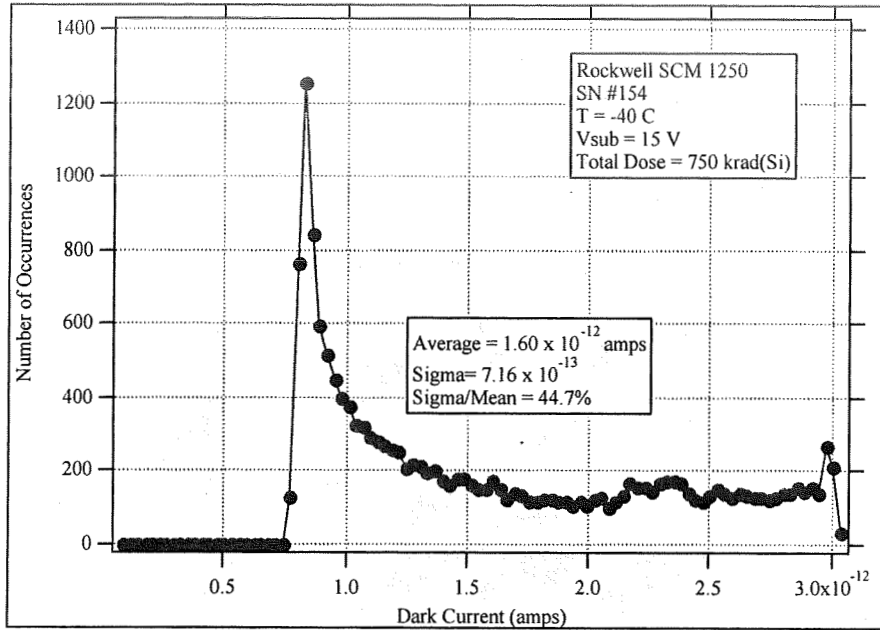


Figure 47. SN #154 Dark Current Histogram, 750 krad(Si)

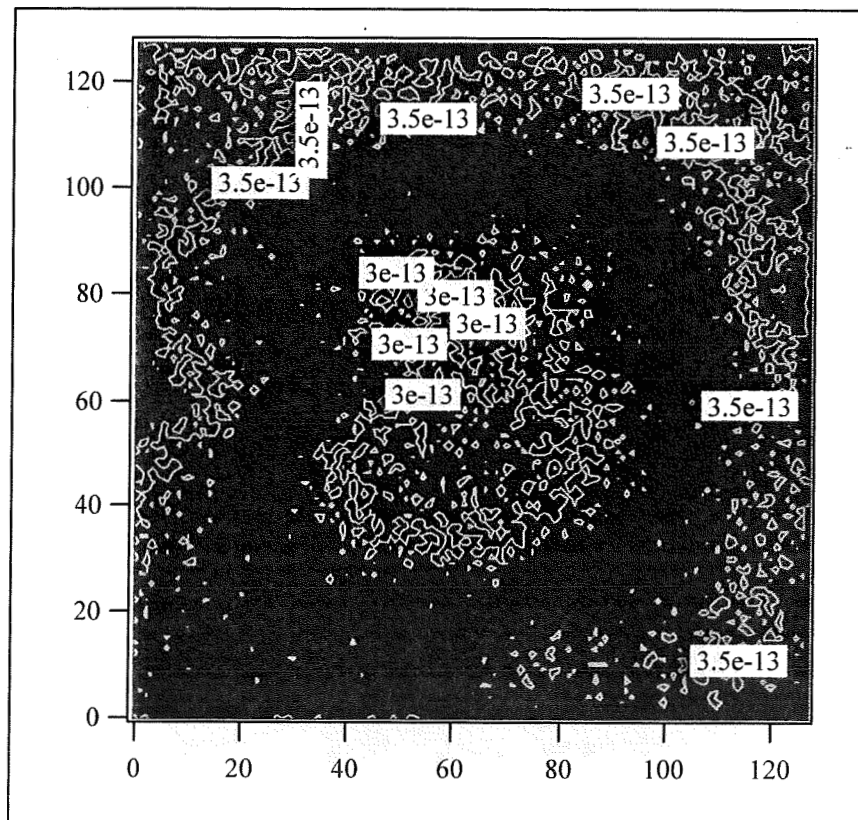


Figure 48. SN #154 Dark Current Map, 200 krad(Si)

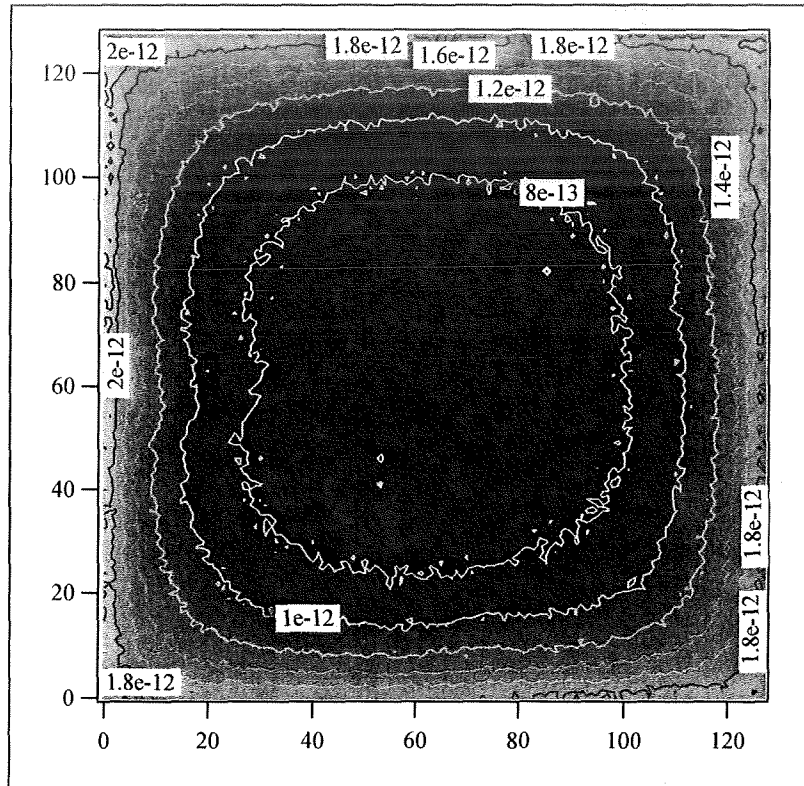


Figure 49. SN #154 Dark Current Map, 400 krad(Si)

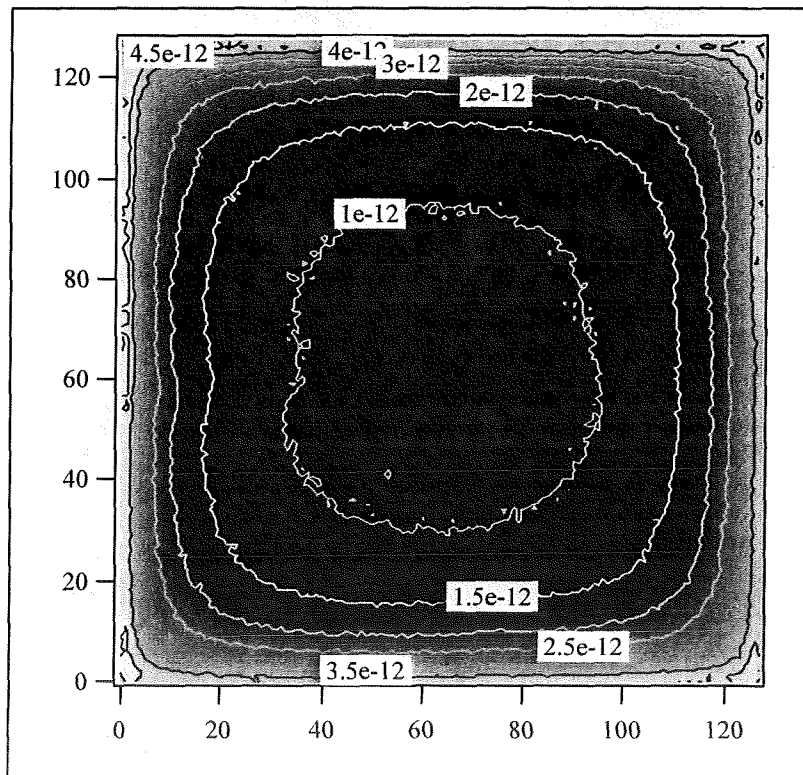


Figure 36. SN #154 Dark Current Map, 600 krad(Si)

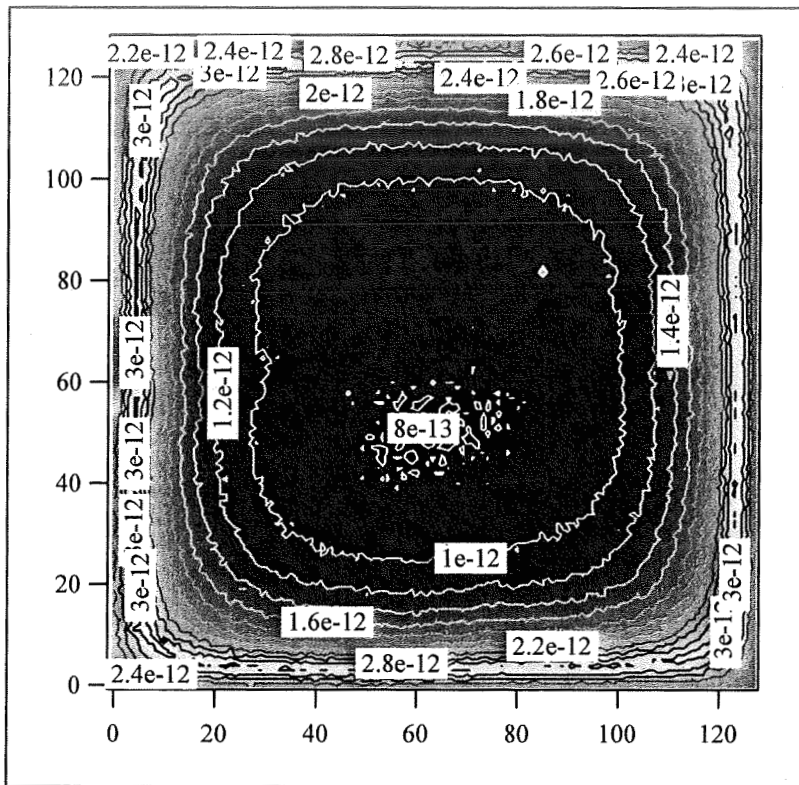


Figure 37. SN #154 Dark Current Map, 750 krad(Si)

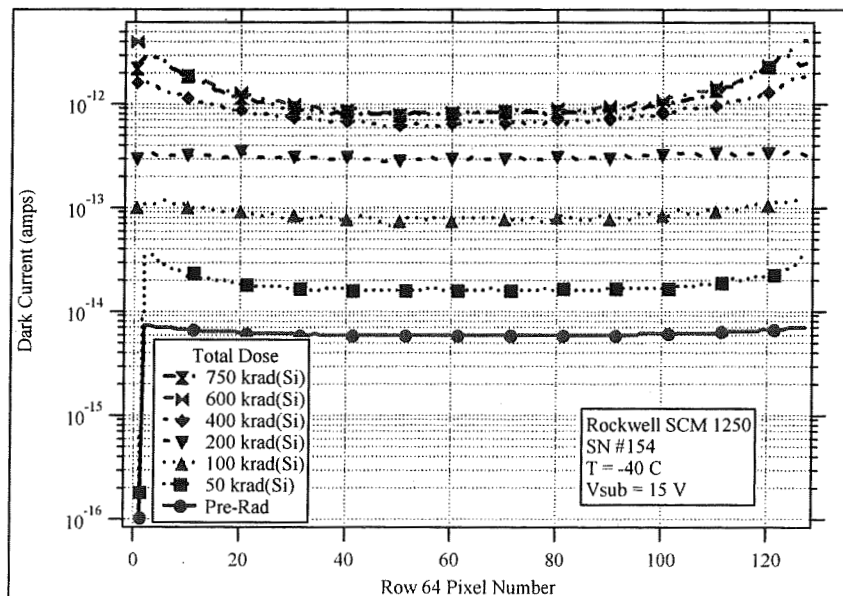


Figure 38. SN #154 Dark Current for Pixels in Row 64 at Various Total Doses

Because of the unusual behavior of the dark current observed for SN #155, the dark current of SN #154 was measured as a function of bias at each total dose level. It was hoped that these data

would shed additional light on the origin of the dark current and the non-uniformity that developed at high doses. Luckily, SN #154 was still operational at 750 krad(Si) and a significant amount of data was collected.

One informative way to plot the dark current versus bias data is in Figure 39. Here the dark currents for a pixel near the edge (7 pixels in from the edge) and one in the center of the array (64 pixels from the edge) are plotted as functions of total dose at V<sub>SUB</sub> voltages of 5, 15, and 25 volts. [Note that 15 V is the nominal operational voltage.] Several observations can be made from this plot: (1) the dark currents increase with bias at all total dose levels; (2) the dark currents increase with total dose; and (3) the dark current is higher for pixels near the edge and it increases faster than for the center pixel. As with SN #155, this origin of this dark current is hypothesized to be the surface effect since the photo response, a bulk effect is not a function of bias.

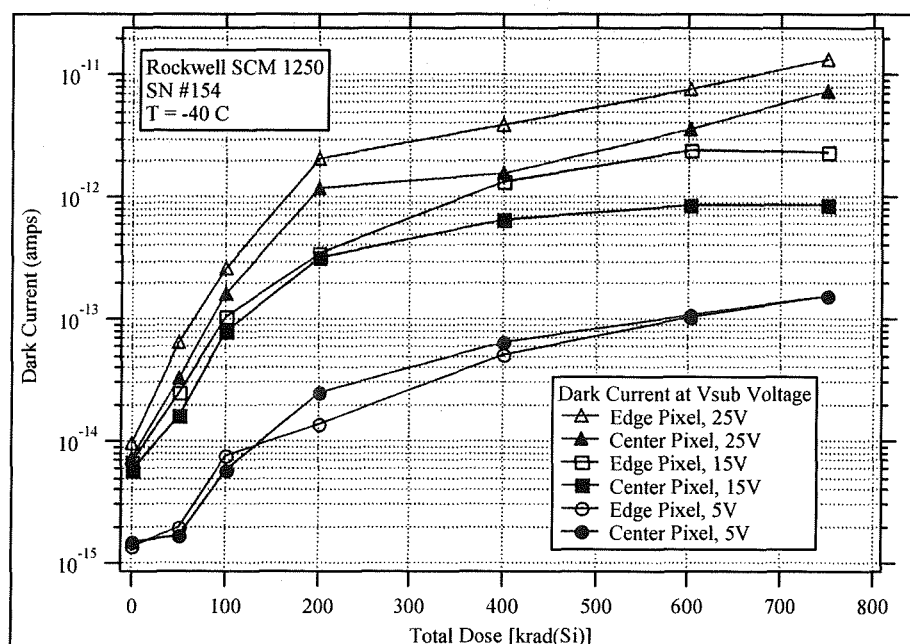


Figure 39. SN #154 Dark Current for Edge and Center Pixels versus Total Dose

Another way to look at the data is shown in Figure 40, where dark currents for edge and center pixels are plotted versus V<sub>SUB</sub> voltage at 100 and 750 krad(Si). Note that at 100 krad(Si) the dark current was fairly uniform, while at 750 krad(Si), it was decidedly non-uniform. We again see that at the same total dose and V<sub>SUB</sub> voltage, the pixel near the center has the lower current. Since the dark current is known to be a strong function of bias, one way to interpret these data would be to say that the pixels near the center of the array were biased to a lower voltage than those near the edge. This would be entirely possible if the resistance of the electrical contact that provides the common bias to all the pixels were too high. The pixel common voltage is typically connected to the edge of the array and bussed to each individual pixel through some type of grid system. Dark current must flow through this contact, and if its resistance is not low enough, a voltage drop can develop.

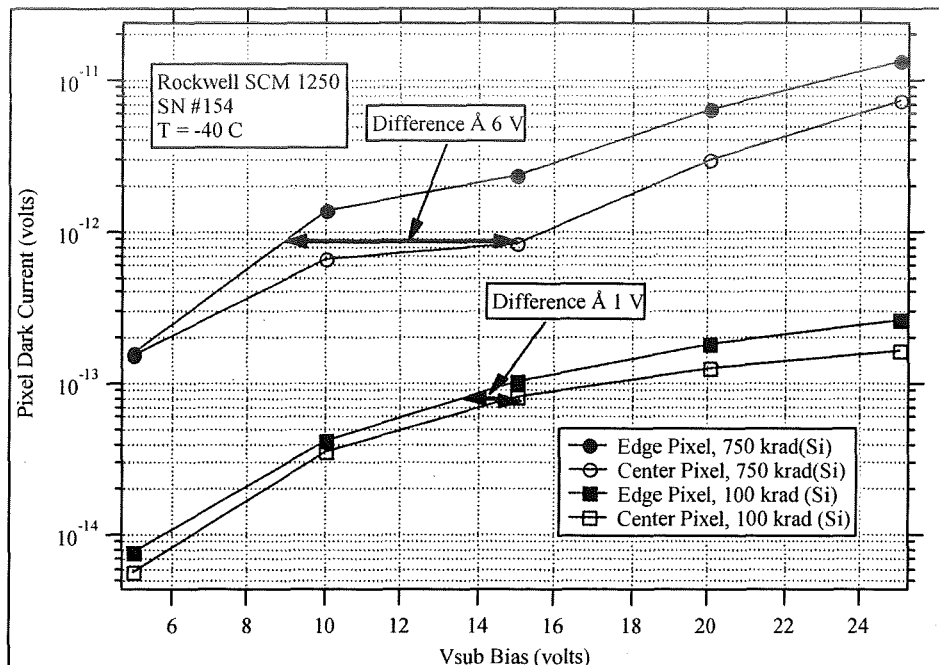


Figure 40. SN #154 Dark Current of Edge and Center Pixels versus VSUB Bias

Looking at Figure 40, note the horizontal lines that are drawn from the center pixel at a VSUB voltage of 15 volts. If the non-uniformity is caused by a bias non-uniformity, then the actual bias on the center pixel for an applied bias of 15 volts, would be the bias point at which these horizontal lines intersects the dark current plots for the edge pixel (assuming that the edge pixel has the full applied bias). At 100 krad(Si), the bias difference, and voltage drop, is approximately 1 volt, while at 750 krad(Si) it is approximately 6 volts.

### 6.2.5 Noise

Pre-Radiation median pixel noise data are shown as functions of irradiance in Figure 41. Also shown in this figure are plots photon noise, based on a quantum efficiency of 0.71 and a conversion gain of  $0.6 \times 10^{-6}$  V/e, and read noise, 0.25 mV. These two noises were RSS'd together to obtain the total noise, which is a good fit to the measured data up to about 200 krad(Si). Above 400 krad(Si) and above, the dark current noise contributes to the total noise at low irradiances. The noise due to a dark current of  $1 \times 10^{-12}$  amps is plotted in the figure and second total noise that includes this dark current noise is also plotted. Note that the dark current is quite non-uniform at higher doses and the dark current chosen here is only representative.

Histograms of pixel noise at several total dose levels are shown in Figure 42 at irradiances where photon noise dominates. We see a very uniform distribution that remains fairly constant until about 600 krad(Si), when dark current begins to become significant.

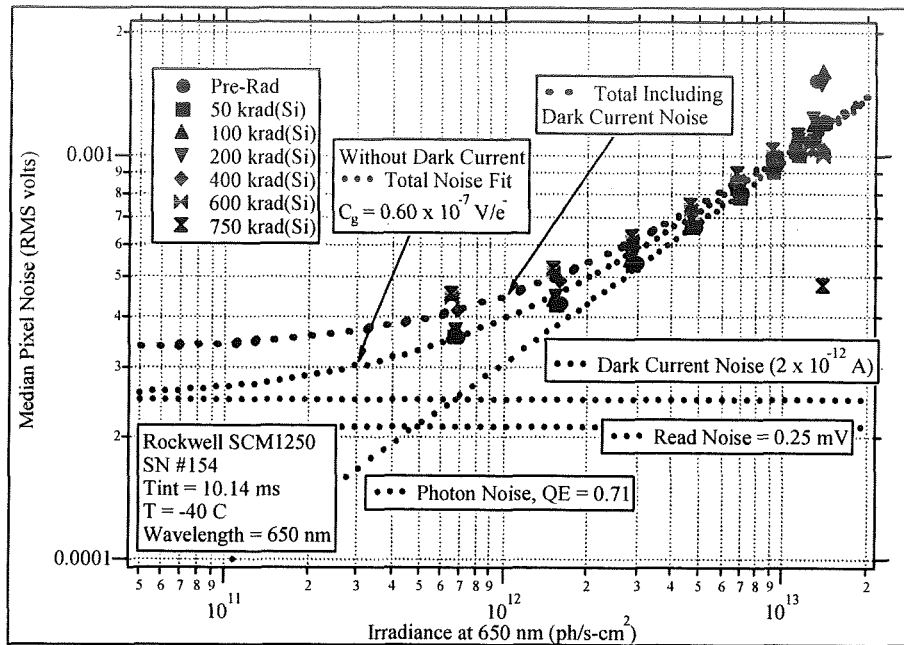


Figure 41. SN #154 Noise versus Irradiance at 650 nm

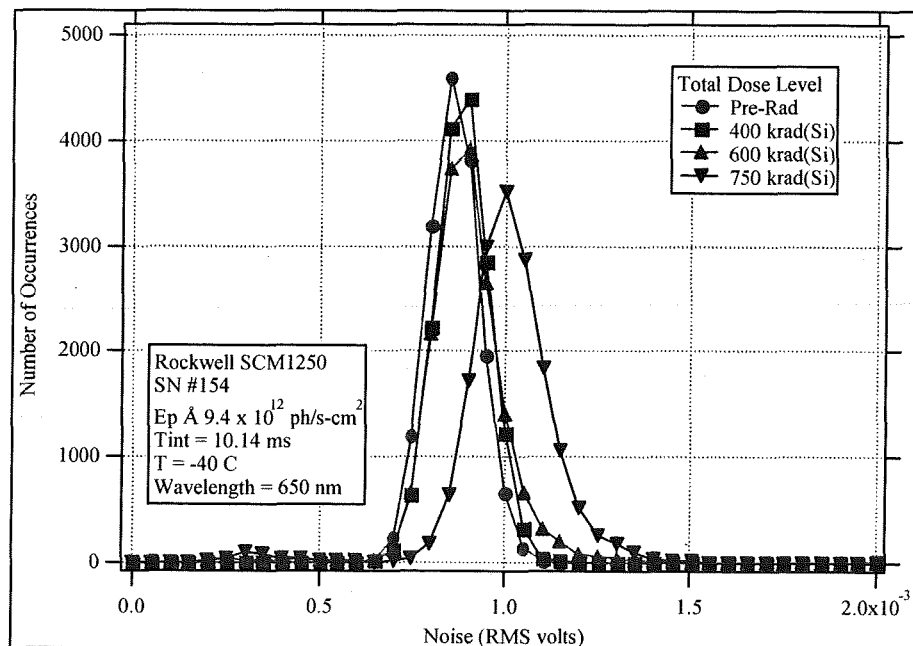


Figure 56. SN #154 Noise Histograms at Various Total Doses

### 6.2.6 Annealed Data

At the conclusion of the last dose and characterization, SN #154 was kept cold for 6 days, and at the end that period, it was completely characterized. The temperature was maintained at -40 C except for the 3<sup>rd</sup> day, when a failure of the cooling system allowed the device to warm up from -40 C to 1 C over night. It was immediately cooled to -40 C and maintained there until the test 3 days later. After this test, it was warmed up to 32 C over night. The next morning it was cooled again to -40 C and re-characterized.

The median output and noise after 750 krad(Si) and for the two annealed tests are shown in Figure and Figure . While the output shows some absolute shift, the responsivity remains constant. The noise is seen to have nearly returned to pre-radiation levels after the 6 day anneal.

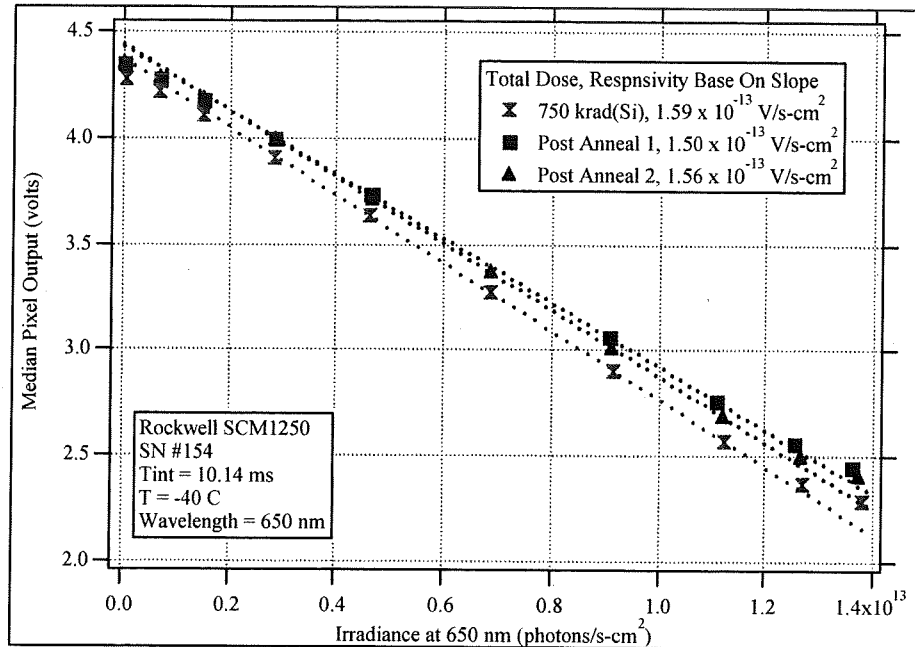


Figure 57. SN #154 Output versus Irradiance, Before and After Anneal

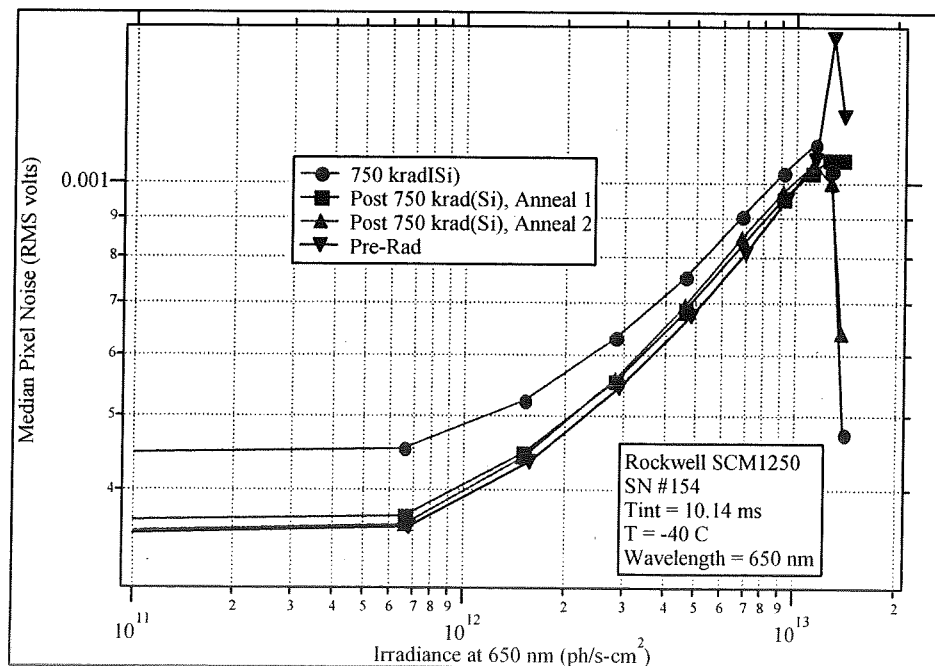


Figure 58. SN #154 Noise versus Irradiance, Before and After Anneal

The median dark current as a function of time after the 750 krad(Si) dose is shown at three VSUB voltages in Figure . The data show that after 6 days at -40 C and after warming up to 32 C, the dark current has been significantly reduced. This result suggests that if the total dose were accumulated more slowly, as on orbit, annealing may take place and the effect of total dose on dark current will be reduced.

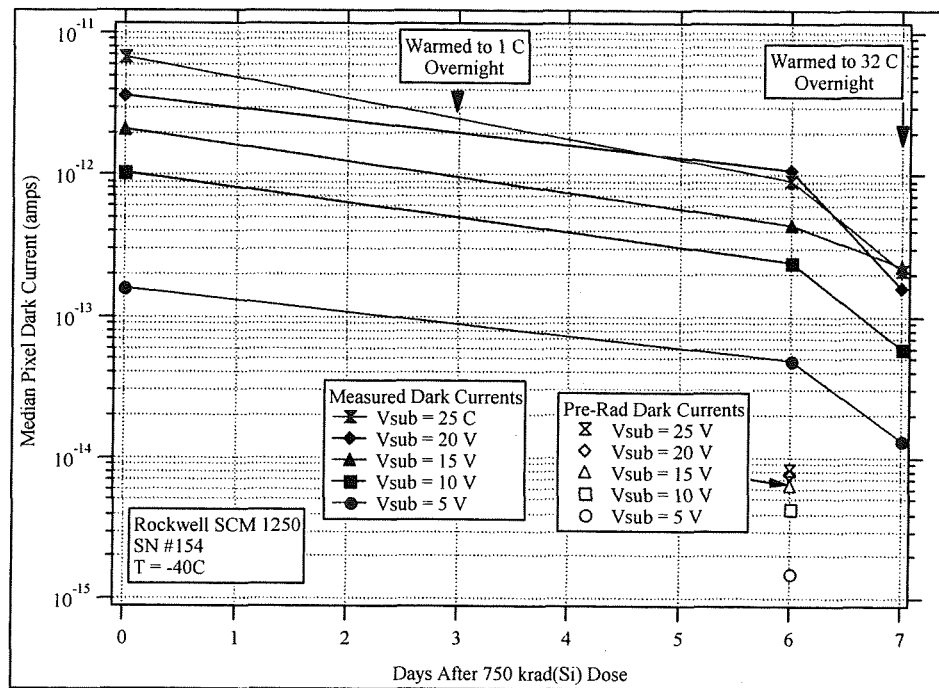


Figure 59. SN #154 Dark Current versus Time After 750 krad(Si) Dose

### 6.3 VFPA S/N 1250-150

RSC VFPA 1250-150 was characterized in a proton environment using the cyclotron at the Crocker Nuclear Laboratory (CNL) at UC Davis. For this experiment, the FPA was irradiated with 63 MeV protons while the VFPA was fully biased and operational at -40 C. The VFPA was mounted at a 45° angle with respect to both the proton beam and the incident photon irradiance so that both the proton beam and visible radiation could simultaneously illuminate the FPA.

#### 6.3.1 Diagnostic Measurements

No appreciable change in any node voltage or current or in the ROIC power dissipation was observed during the proton fluence test.

#### 6.3.2 Conversion Gain

**DC Current Method** Data obtained during spectral response measurements were used to determine the ROIC conversion gain using the DC Current method describe above. During these measurements, the total detector current and pixel outputs were measured at two or more different integration times or at two or more different irradiances at several irradiances (using different spectral filters). Since the outputs at different wavelengths were measured at different integration times, the outputs have been normalized to each integration time to make the data compatible. This normalized output is plotted as a function of detector current in Figure 42. The



conversion gain determined from these data is  $0.62 \times 10^{-6}$  V/e, relatively close to the  $0.7 \times 10^{-6}$  V/e design value.

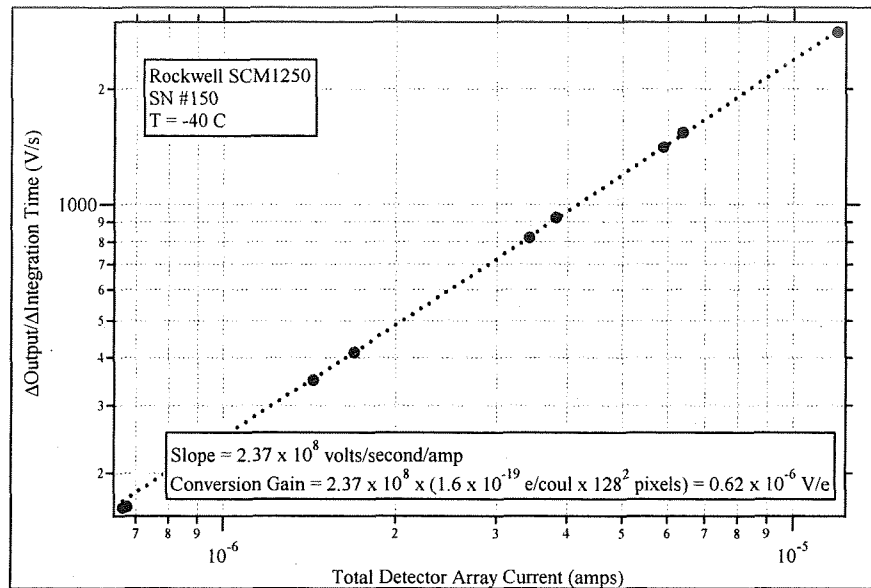


Figure 42. SN #150 DC Current Data Used to Determine Conversion Gain

**Mean-Variance Method** Pixel output voltages and RMS noises were measured at a number of photon irradiances at 650 nm and the square of the noise (variance) is plotted as a function of the output voltage in Figure 43. These data can be fit with a straight line, indicative of shot noise limited operation, and the ROIC conversion gain, obtained as the slope of this plot, is  $0.51 \mu\text{V}/\text{electron}$ . It is unclear why the conversion gains determined from the two methods do not agree since the assumptions made for each method seem to be reasonable. The value determined from the DC current method,  $0.62 \times 10^{-6}$  V/e, it is thought to be more accurate since it is closer to the design value. Conversion gain measurements were made as a function of proton fluence, and no change was observed.

### 6.3.3 Spectral Response

The spectral response of SN #150 was determined using both the total detector current and the output voltages as measured as a function of wavelength. These data are shown in Figure 44. The *average* pixel quantum efficiency (QE) can be determined directly from the current measurement, while the conversion gain must be known to determine the QE from the output data. Using a conversion gain of  $0.65 \times 10^{-7}$  V/e allows the QEs determined from the two sets of data to agree. It is not surprising that this value is close to that determined from the DC current method. The QE was monitored at several wavelengths as a function of proton fluence during the course of these measurements, and no changes were observed that were not within experimental error. This conclusion will be further reinforced below where responses as a function of proton fluence and detector bias are presented.

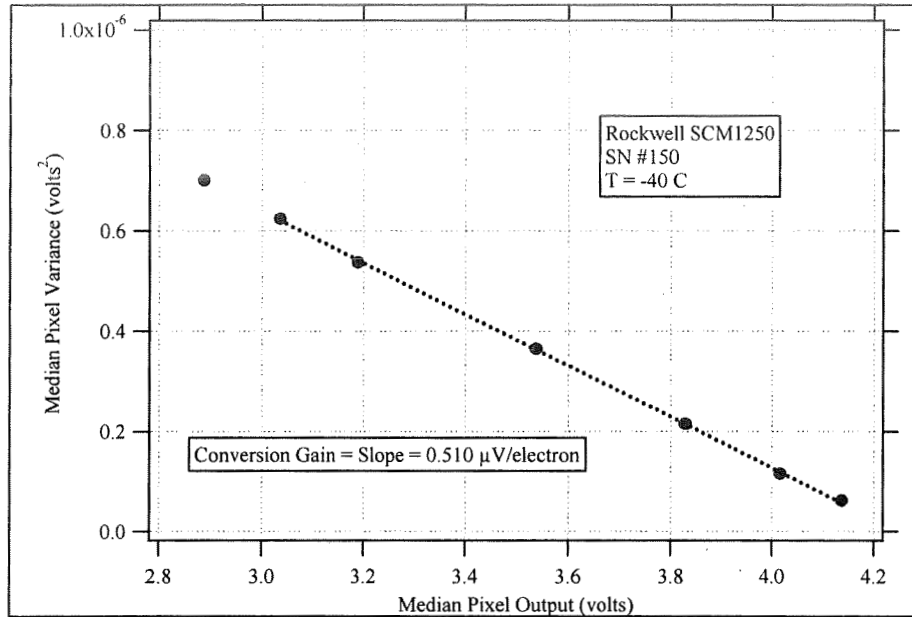


Figure 43. SN # 150 Mean-Variance Data Used to Determine Conversion Gain

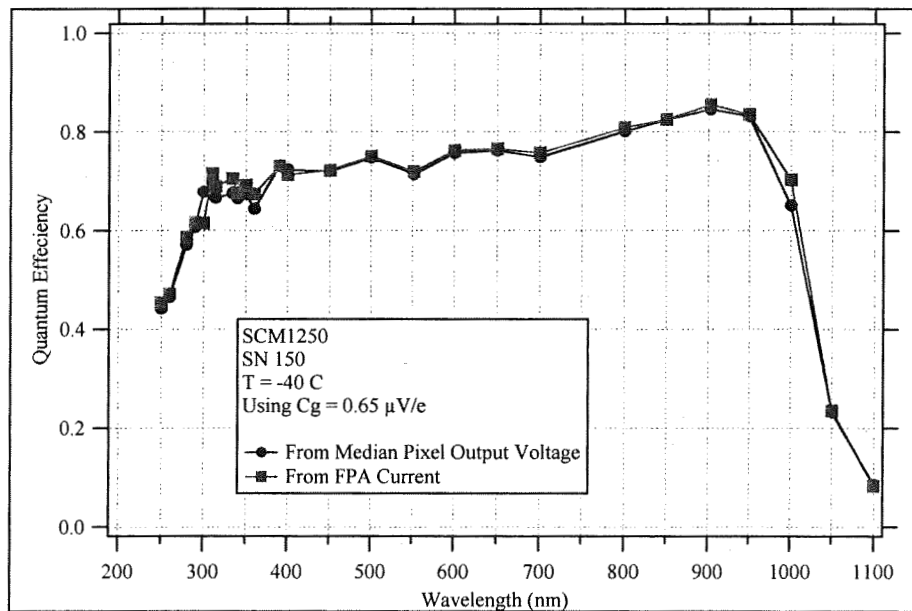


Figure 44. Spectral Response of SN #150 Using Both Detector Current and Output Voltage

### 6.3.4 Output

Pixel output voltage data, obtained as a function of photon irradiance, are presented in this section. Data are also shown that describe pixel output voltage as a function of VSUB (detector) bias.

#### 6.3.4.1 Responsivity

The median pixel output voltage is plotted as a function of photon irradiance at 650 nm in Figure 45 and **Error! Reference source not found.** Figure 45 is a plot of the pre-radiation data,

showing the linearity of the ROIC of better than 1% over most of the output voltage range. Similar output data at different proton fluences, show that the responsivity is constant up to the relevant dose levels of this study.

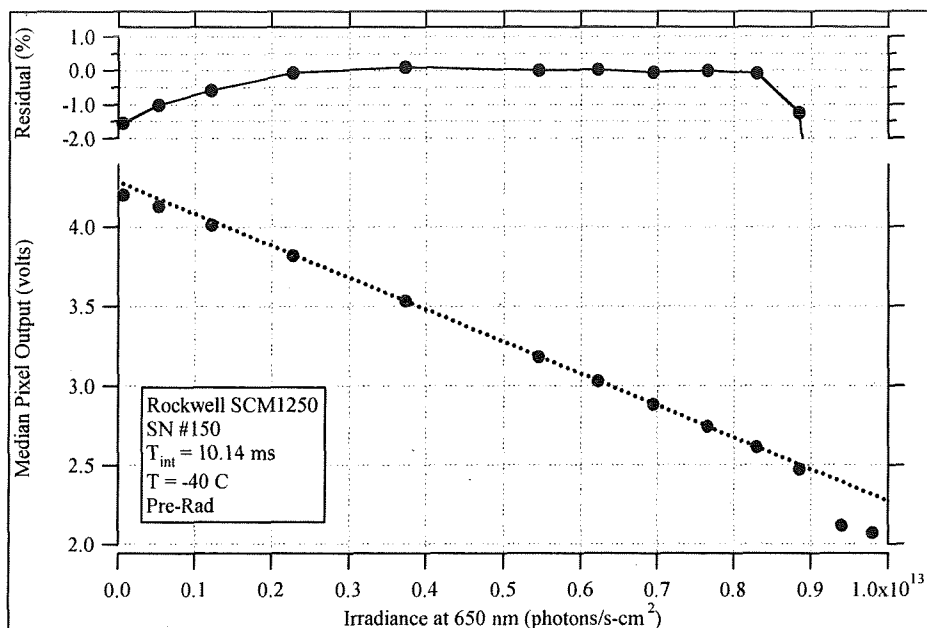


Figure 45. SN #150 Pre-Radiation Output versus Irradiance at 650 nm

Responsivity histograms are shown in Figure 46 for both pre-radiation and at the maximum proton fluence. These data were obtained from the difference in pixel outputs at two irradiances. Very little change is note in either the average or the very uniform distribution, which is consistent with the responsivity plots in **Error! Reference source not found.**

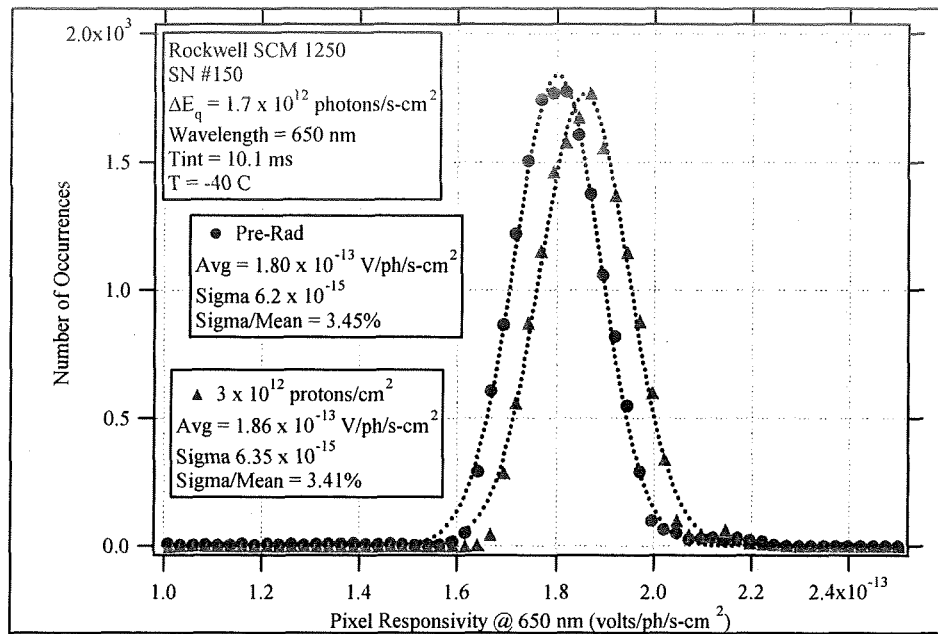


Figure 46. SN #150 Responsivity Histograms, Pre-Rad and Maximum Fluence

#### 6.3.4.2 Response versus Bias

A major objective of these tests was to determine if the quantum efficiency (QE) of the PIN detectors changed with proton fluence, especially at very short UV wavelengths. While the detectors were completely depleted prior to radiation at a substrate bias of 15 volts, it was thought that higher biases might be necessary for full depletion at high proton fluences, and that the QE at a bias 15 volts could go down with fluence. Thus, QE as a function of bias was measured at several wavelengths prior to radiation, and the variation in QE with bias was tracked with proton fluence.

Prior to radiation, the QE was found to be independent of bias at all wavelengths from near zero volts to 15 volts. During the accumulation of proton fluence, little or no change in QE was observed over this bias range, and it was decided to increase the bias range to 40 volts to insure that full depletion was being achieved. Median pixel response, normalized to the response at a bias of 40 volts, is plotted in Figure at the maximum proton fluence,  $3 \times 10^{12}$  p/cm<sup>2</sup>. The data show that at the maximum fluence, a small increase in bias is required to reach the maximum response (QE), generally taking higher bias at shorter wavelengths. However, even at the shortest wavelengths, the loss of QE at a bias of 15 volts is less than 5% at the maximum fluence.

The ratio of the response at 15 V to that at 40 volts is plotted in as a function of wavelength in Figure to illustrate this point. These data show that the QE at a substrate bias of 15 volts at all wavelengths decreases less than 4% up to a fluence of  $3 \times 10^{12}$  p/cm<sup>2</sup>, and an increase in substrate bias could further minimize this decrease.

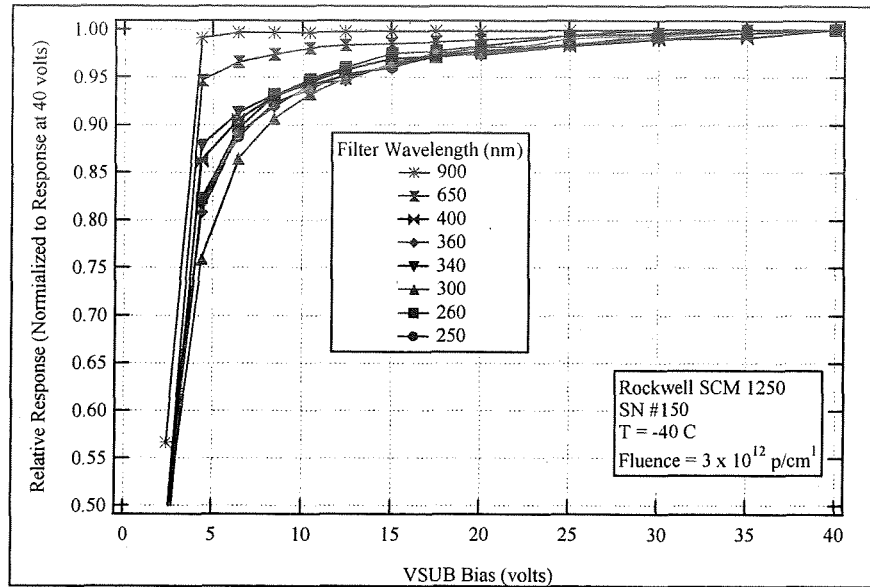


Figure 65. SN #150 Normalized Response versus Substrate Bias at Several Wavelengths

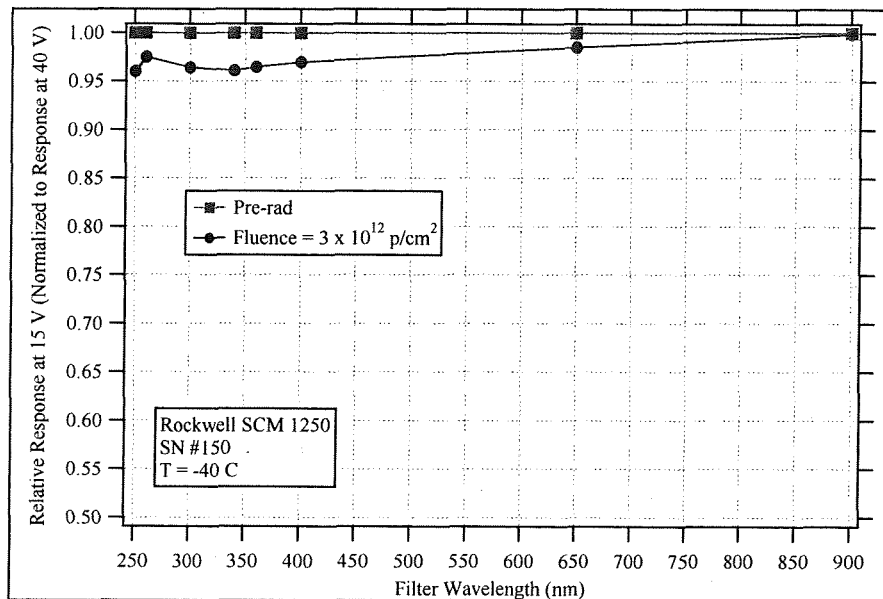


Figure 66. SN #150 Relative Response at VSUB = 15 V versus Wavelength

### 6.3.5 Dark Current

Pixel dark currents were determined by measuring the output of the VFPA at several integration times at low photon irradiance. Data were collected at several integration times to insure the measured data were linear with integration time at each fluence. The median pixel dark current versus proton fluence is shown in Figure . These data show that the dark current increases approximately linearly with fluence, approximately 2 orders of magnitude from pre-rad to the maximum fluence,  $3 \times 10^{12} \text{ p/cm}^2$ . After all data had been obtained at the maximum fluence, SN #150 was kept at -40 C for 34 hours and the dark current was re-measured. This data point, the

blue square on Figure , shows a slight decrease in dark current over that elapsed time. This data suggests that if the proton fluence is accumulated over an extended period of time (as in space), annealing will take place and the actual dark current will be less than that shown in this figure.

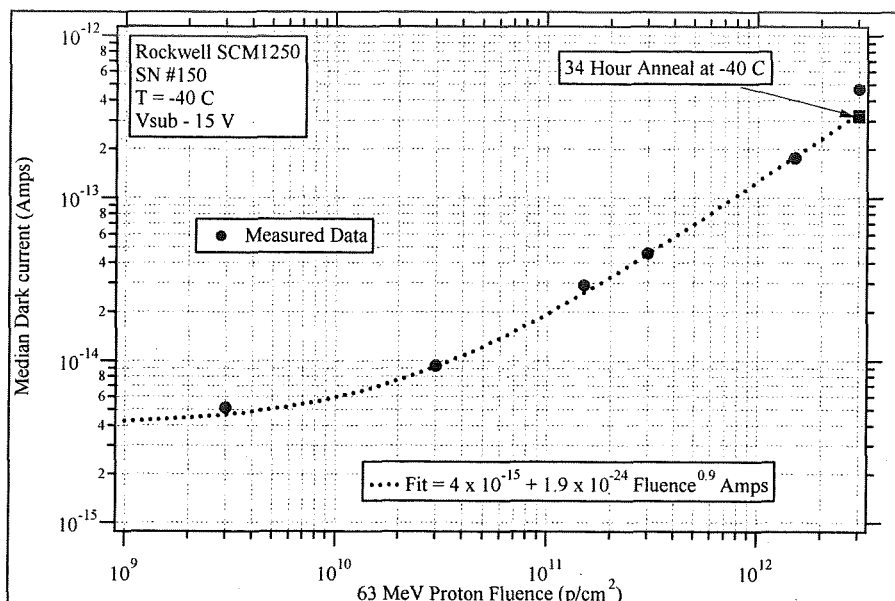


Figure 67. SN #150 Dark Current versus Proton Fluence

The pre-radiation median pixel dark current, along with the dark current at the maximum proton fluence (after anneal), is shown as a function of inverse temperature in Figure , and dark current distributions for pre-radiation and maximum fluence conditions are shown in Figure and Figure 47, respectively. The pre-radiation distribution is quite uniform while that at the maximum fluence has high current tail. However, in the dark current distribution obtained after the 34 hour anneal, shown in Figure 48, the tail is significantly reduced.

A 2-D map of the pre-radiation dark current is shown in Figure 49. As indicated by the histogram above, the current is quite uniform. A dark current map at  $3 \times 10^{12}$  p/cm<sup>2</sup>, given in Figure 50, shows that the higher current pixels tend to be located around the perimeter of the detector array. A 2-D map of dark current at  $3 \times 10^{12}$  p/cm<sup>2</sup> after the 34 hour anneal is shown in Figure 51. The high current associated with the perimeter pixels has been significantly reduced. This dark current non-uniformity is similar to that seen in total dose tests on SN # 154 and SN #155 and is likely caused by the same thing, a non-uniformity in the detector bias.

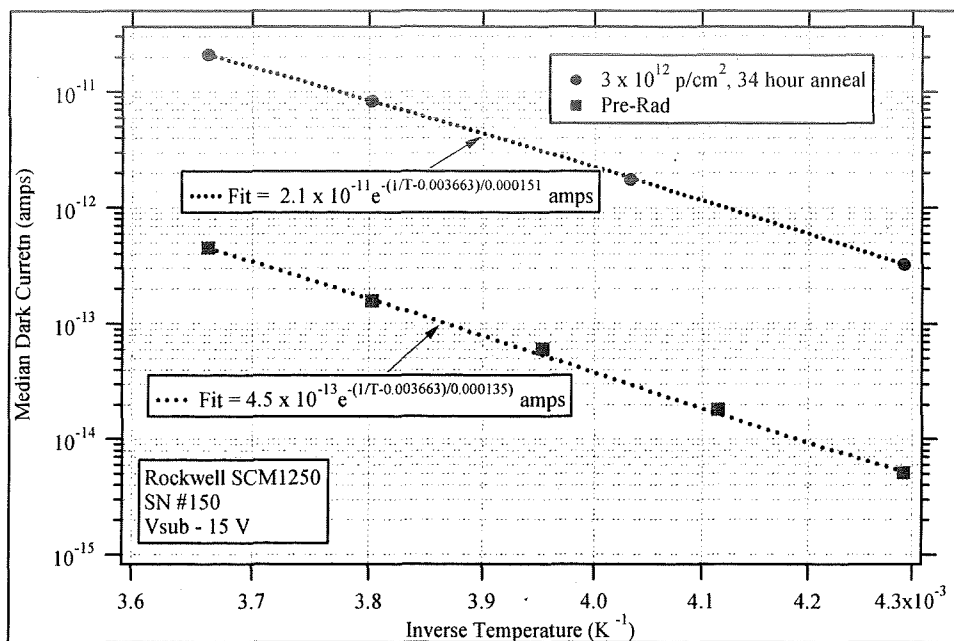


Figure 68. SN #150 Dark Current versus Inverse Temperature

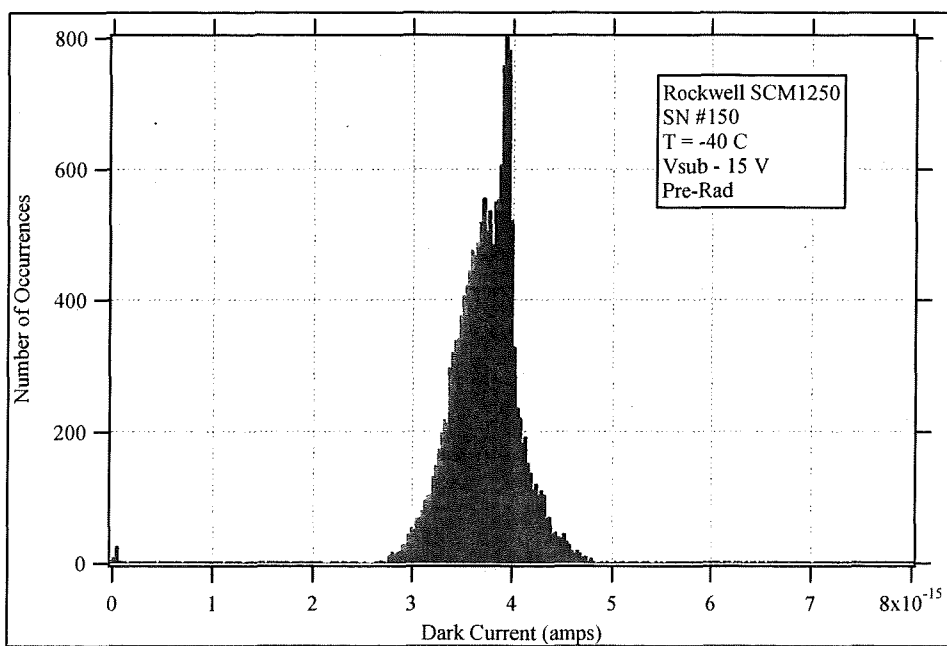


Figure 69. SN #150 Pre-Rad Dark Current Distribution

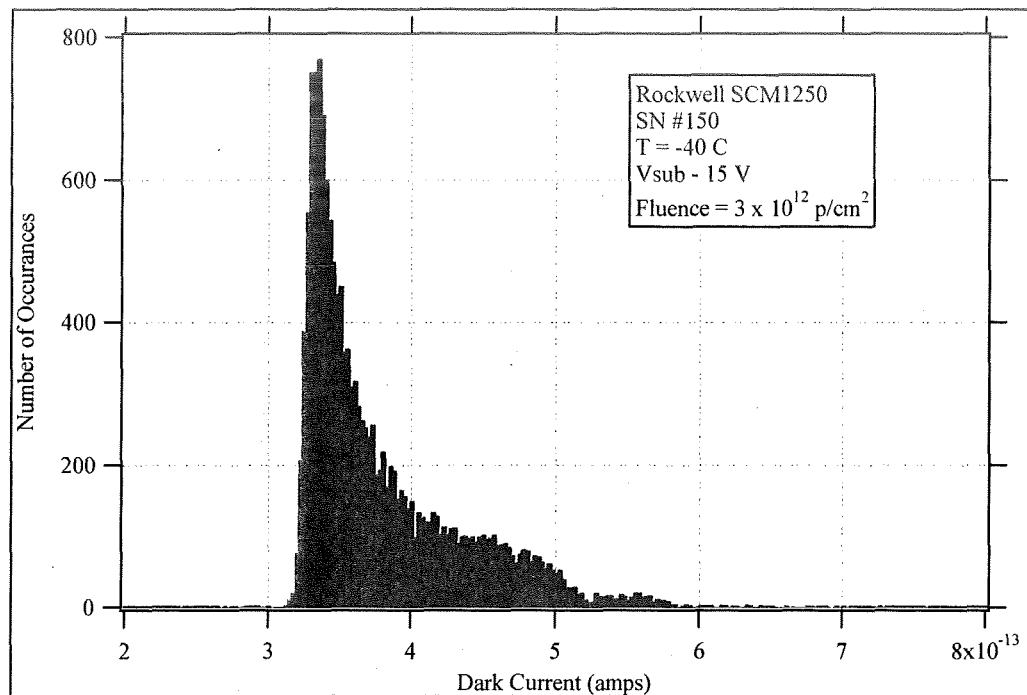


Figure 47. SN #150 Dark Current Histogram at  $3 \times 10^{12}$  p/cm<sup>2</sup>

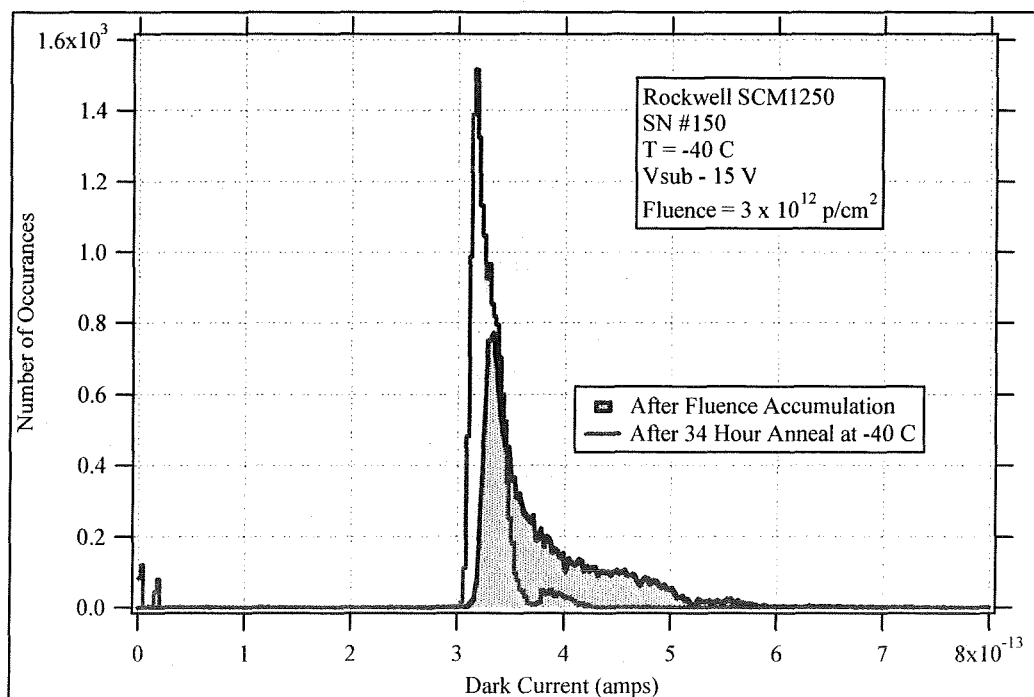


Figure 48. SN #150 Dark Current Histogram at  $3 \times 10^{12}$  p/cm<sup>2</sup>, Right After Accumulation and After 34 Hour Anneal



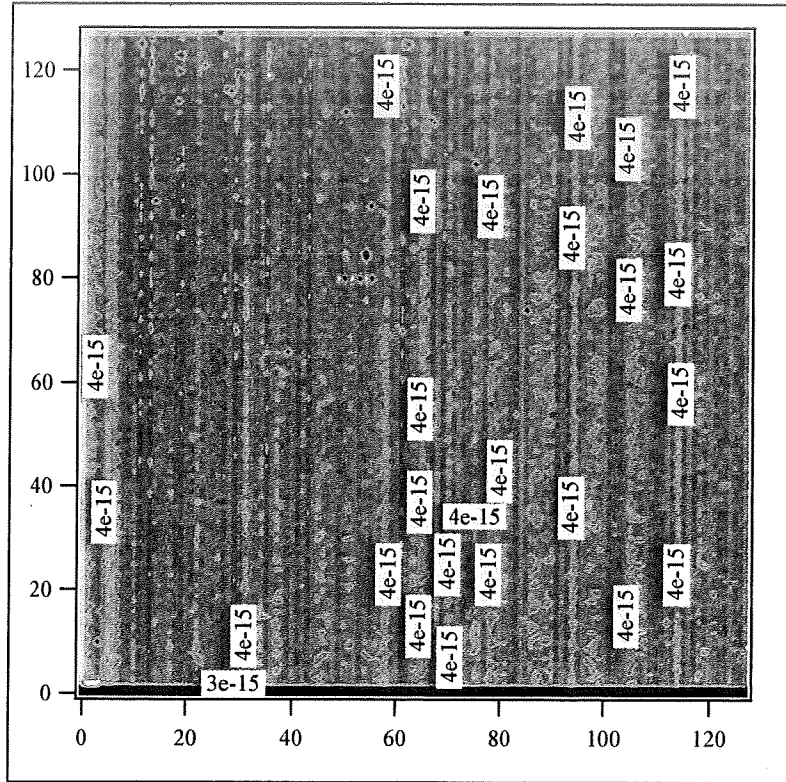


Figure 49. SN #150 2-D Map of Pre-Radiation Dark Current

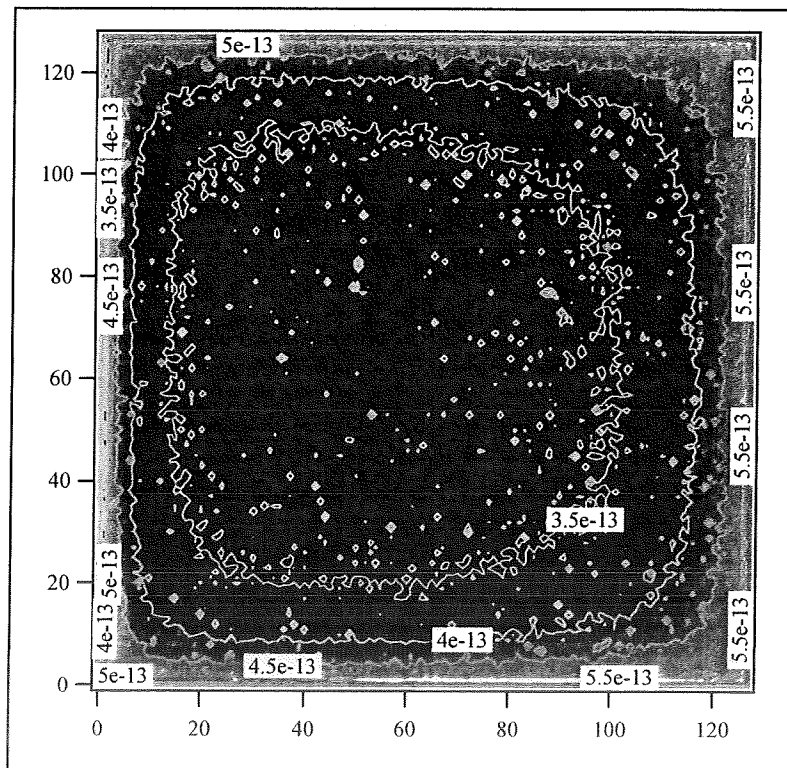


Figure 50. SN #150 Dark Current Map at  $3 \times 10^{12} \text{ p/cm}^2$

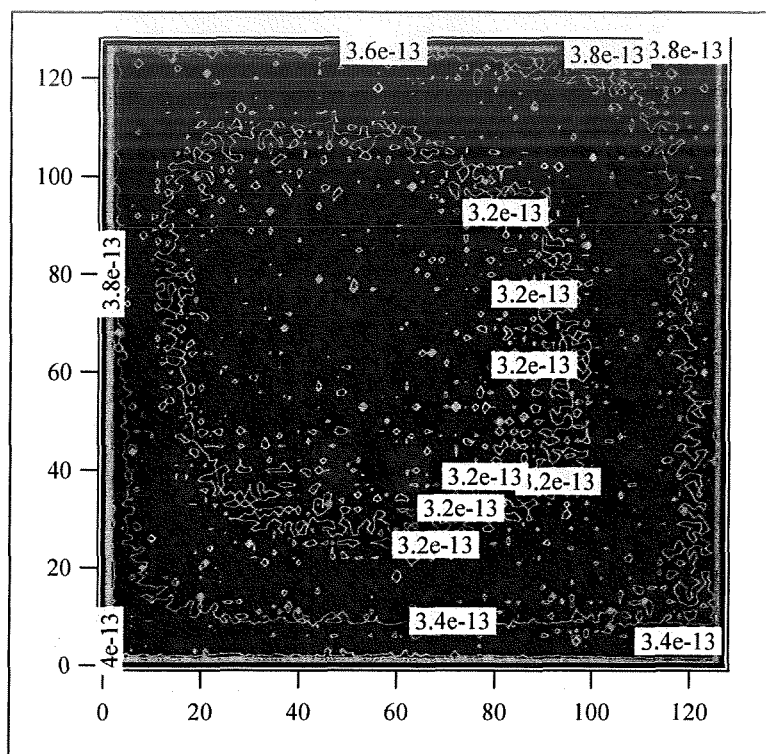


Figure 51. SN #150 Dark Current Map After 34 Hour Anneal

### 6.3.6 Noise

Pre-Radiation median pixel noise data are shown as functions of irradiance in Figure . Also shown in this figure are plots of read noise, photon noise, and the total noise (dark current noise is not significant at these irradiances and integration times). The read noise used was 0.14 mV, and the photon noise was based on a quantum efficiency of 0.77 and a conversion gain of  $0.62 \times 10^{-6}$  V/e. There is some increase in noise as the readout approaches saturation, but the noise basically has two terms, readout noise and photon noise. Noise data at all fluence levels are shown in Figure , and little change in median noise is observed at all fluences.

Histograms of noise at an irradiance of  $4.4 \times 10^{12}$  ph/s-cm<sup>2</sup> for pre-radiation and at the maximum fluence are shown in Figure . Both distributions are relatively uniform with the distribution at the maximum fluence slightly higher in average noise but significantly wider. Some of this increase in noise could be due to the creation of radioactive parts within the Dewar by protons.

### 6.3.7 Transient Data

Histograms of pixel outputs for 25 frames of data collected at three proton fluence rates are shown in Figure . The exact shapes of these distributions are related to the geometries shown in Figure 7. One histogram obtained at the maximum fluence rate for 190 frames is shown in Figure . With the data provided by the additional frames, the shape of the distribution at higher output voltages is clearer.

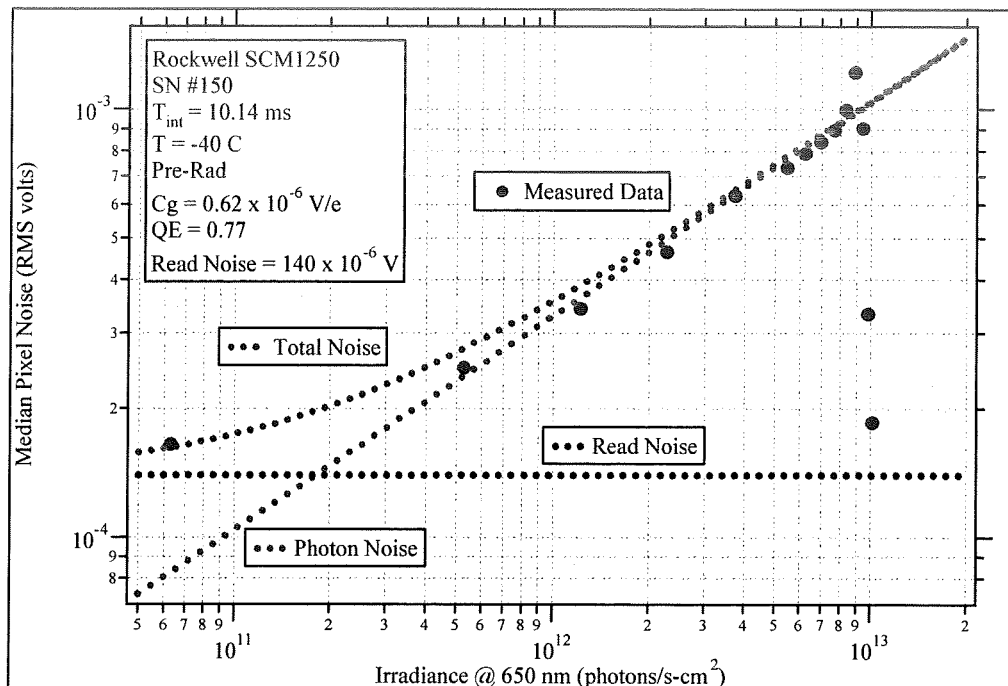


Figure 75. SN #150 Noise versus Irradiance at 650 nm, Pre-Radiation

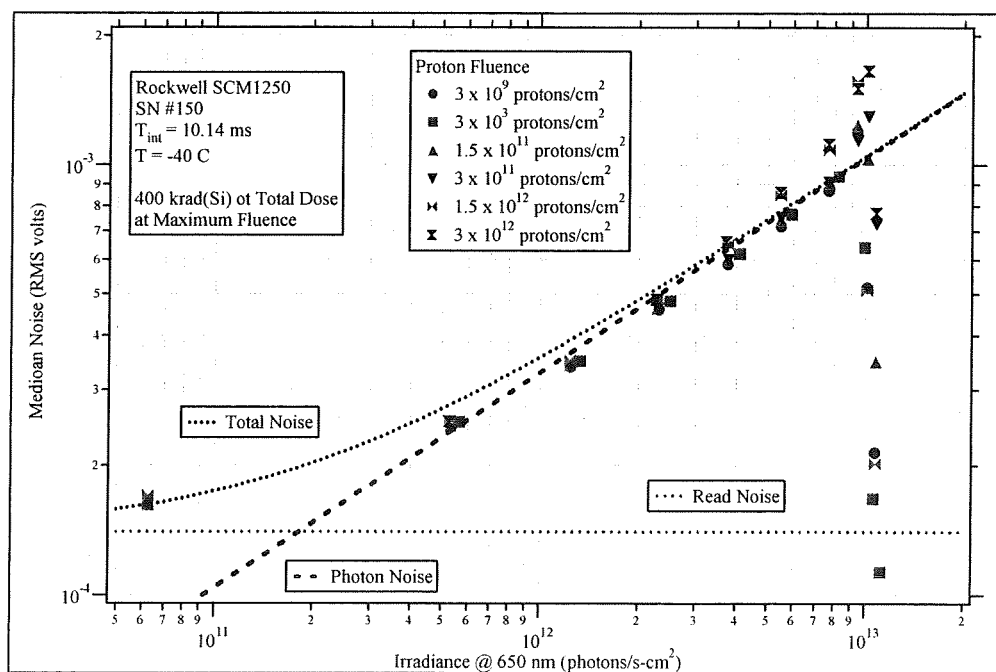


Figure 76. SN #150 Median Noise versus Irradiance at 650 nm, All Fluences

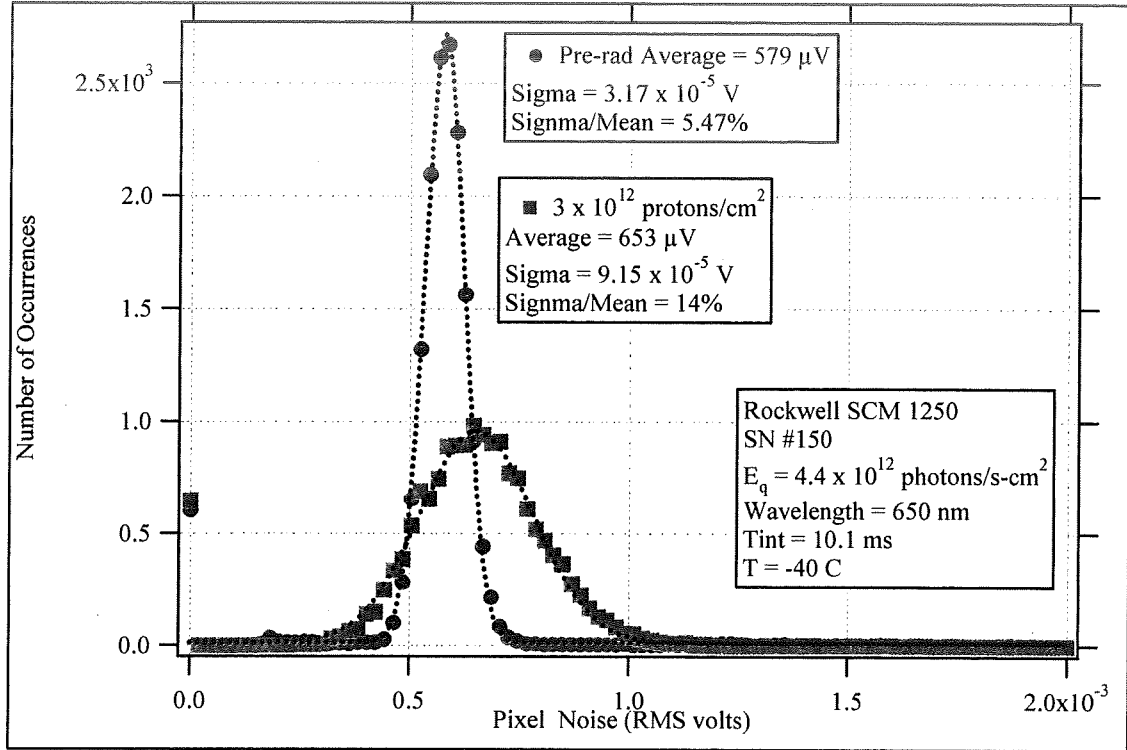


Figure 77. SN #150 Noise Histograms at  $4.4 \times 10^{12}$  ph/s-cm<sup>2</sup>

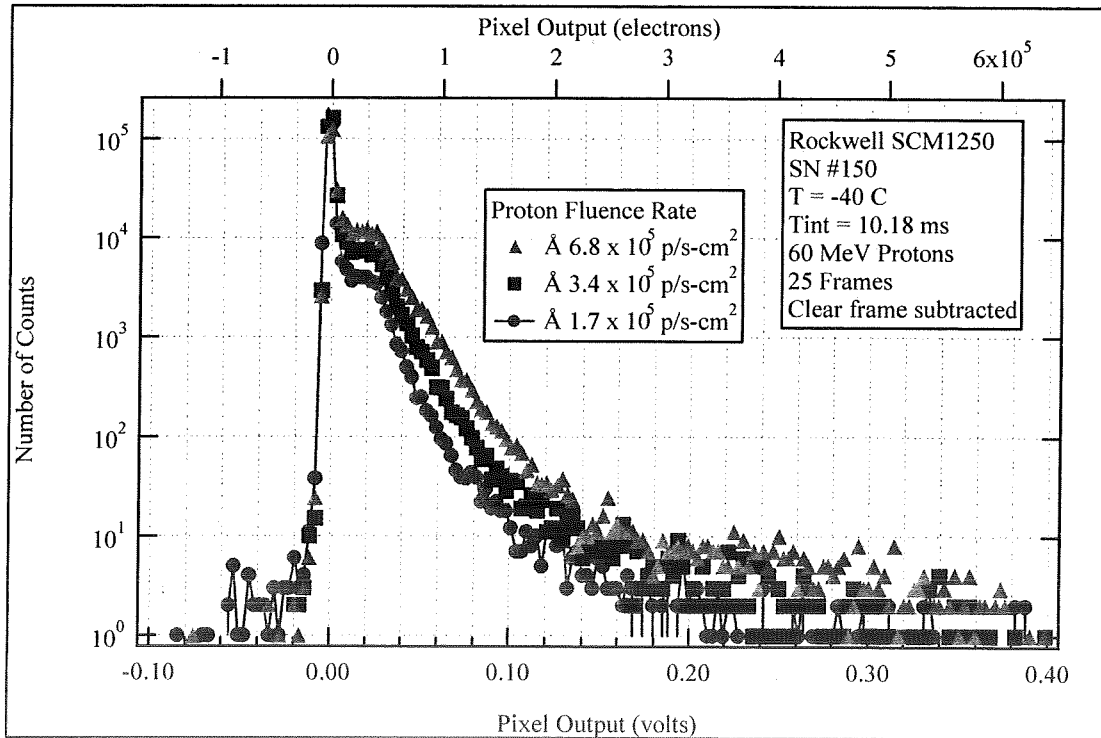


Figure 78. SN #150 Histograms of Output at Different Fluence Rates for 25 Frames

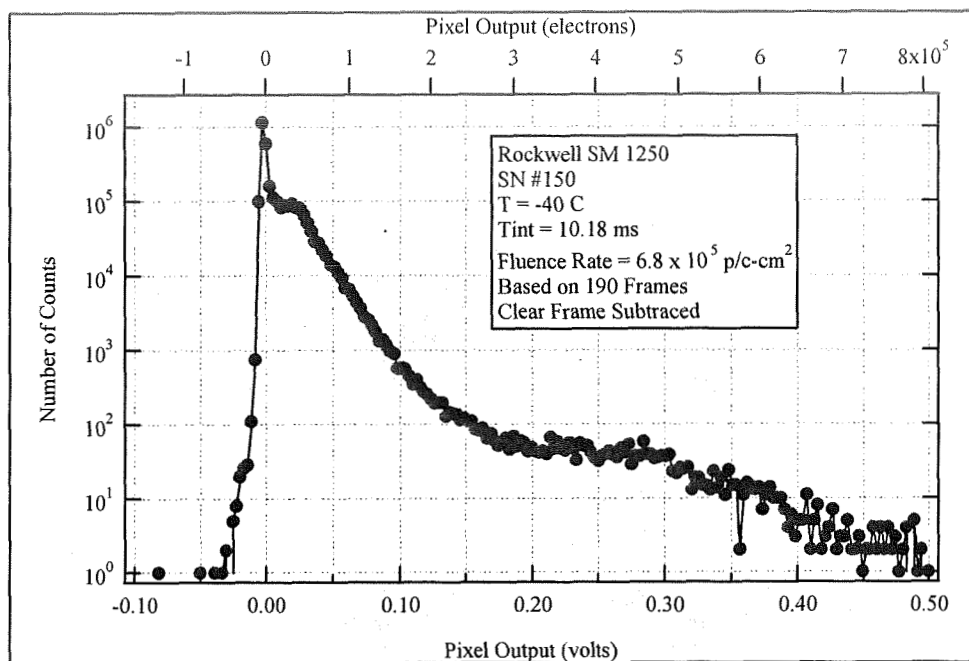


Figure 79. SN #150 Histogram of Output from 190 Frames at  $6.8 \times 10^5$  p/s-cm<sup>2</sup>

Three frames of output data at the three proton fluence rates are shown in Figure 52 through Figure 54. Here, black represents no proton events and the events amplitudes increase as the colors move through the following color sequence: brown, red, orange, yellow, white, and blue. The presence of proton events in adjacent pixels is apparent, especially at the higher event rates.

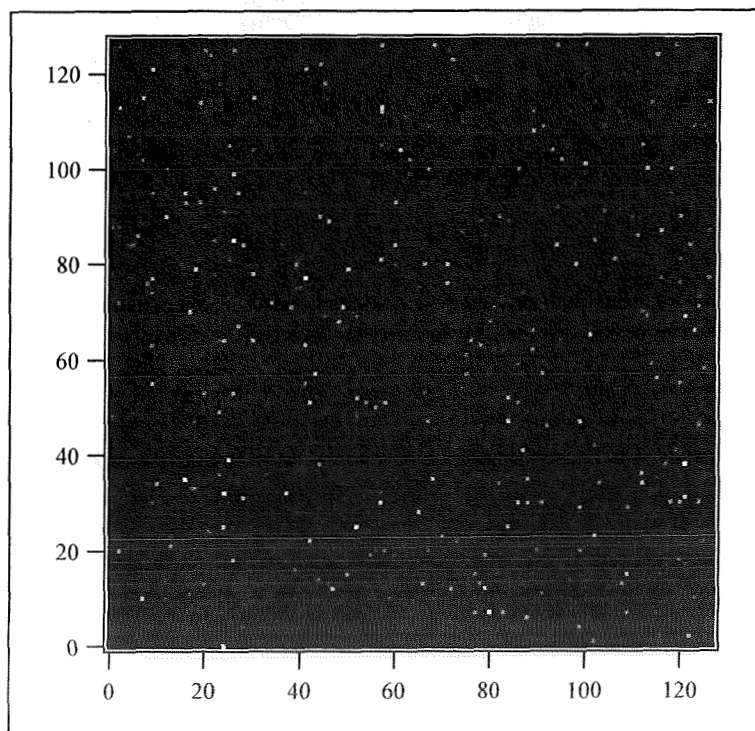


Figure 52. SN #150 One Output Frame at  $1.7 \times 10^5$  protons/s-cm<sup>2</sup>

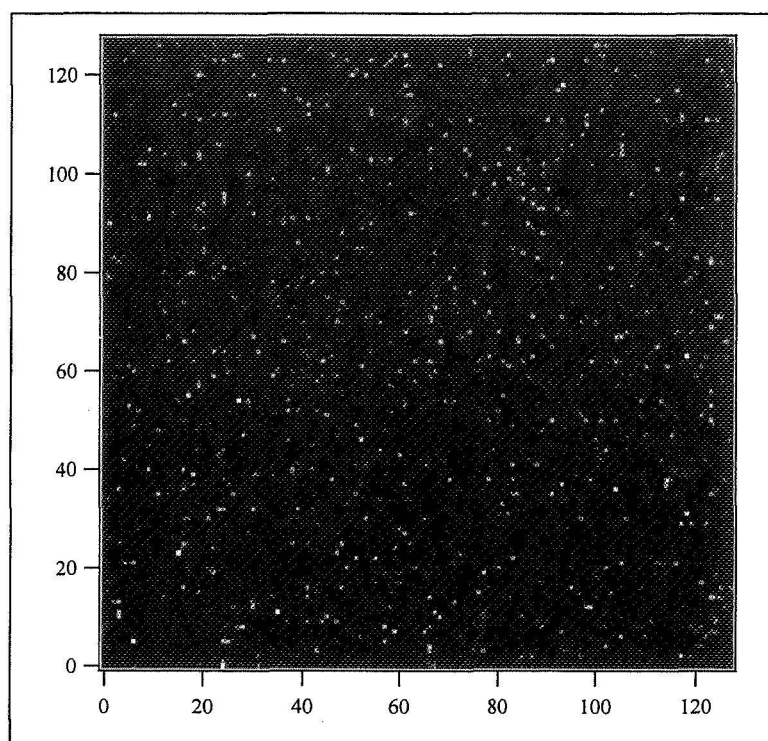


Figure 53. SN #150 One Output Frame at  $3.4 \times 10^5$  protons/s-cm<sup>2</sup>

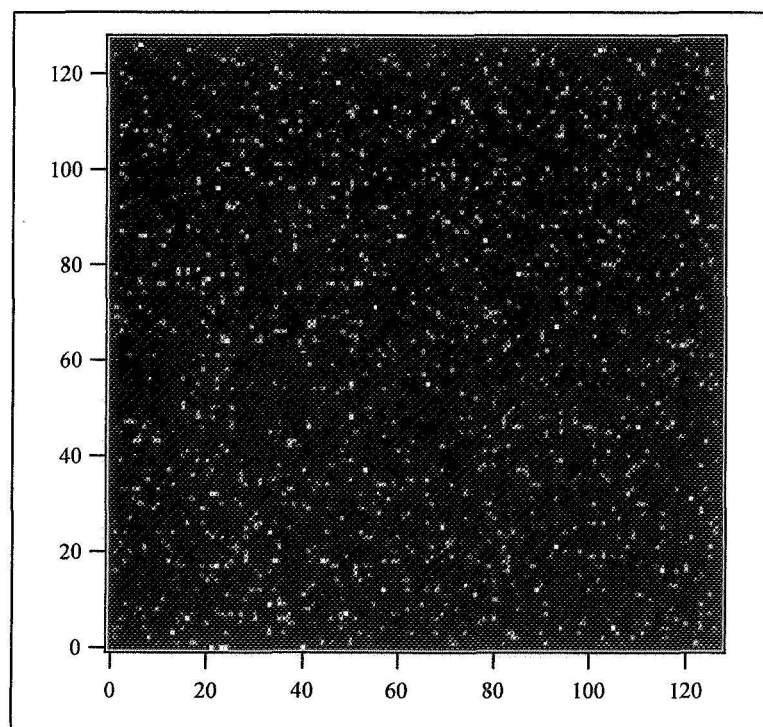


Figure 54. SN #150 One Output Frame at  $6.8 \times 10^5$  protons/s-cm<sup>2</sup>

## 6.4 VFPA S/N 1250-157

RSC VFPA 1250-157 was characterized in a proton environment using the cyclotron at the Crocker Nuclear Laboratory (CNL) at UC Davis. For this experiment, the FPA was irradiated with 63 MeV protons while the VFPA was fully biased and operational at -40 C. The VFPA was mounted at a 45° angle with respect to both the proton beam and the incident photon irradiance so that both the proton beam and visible radiation could simultaneously illuminate the FPA.

### 6.4.1 Diagnostic Measurements

No appreciable change in any node voltage or current or in the ROIC power dissipation was observed during the proton fluence test.

### 6.4.2 Conversion Gain

**DC Current Method** Data obtained during spectral response measurements were used to determine the ROIC conversion gain using the DC Current method describe above. During these measurements, the total detector current and pixel outputs were measured at two or more different integration times or at two or more different irradiances at several irradiances (using different spectral filters). Since the outputs at different wavelengths were measured at different integration times, the outputs have been normalized to integration time to make the data compatible. This normalized output is plotted as a function of detector current in Figure 55. The conversion gain determined from these data is  $0.63 \times 10^{-6}$  V/e, relatively close to the  $0.7 \times 10^{-6}$  V/e design value.

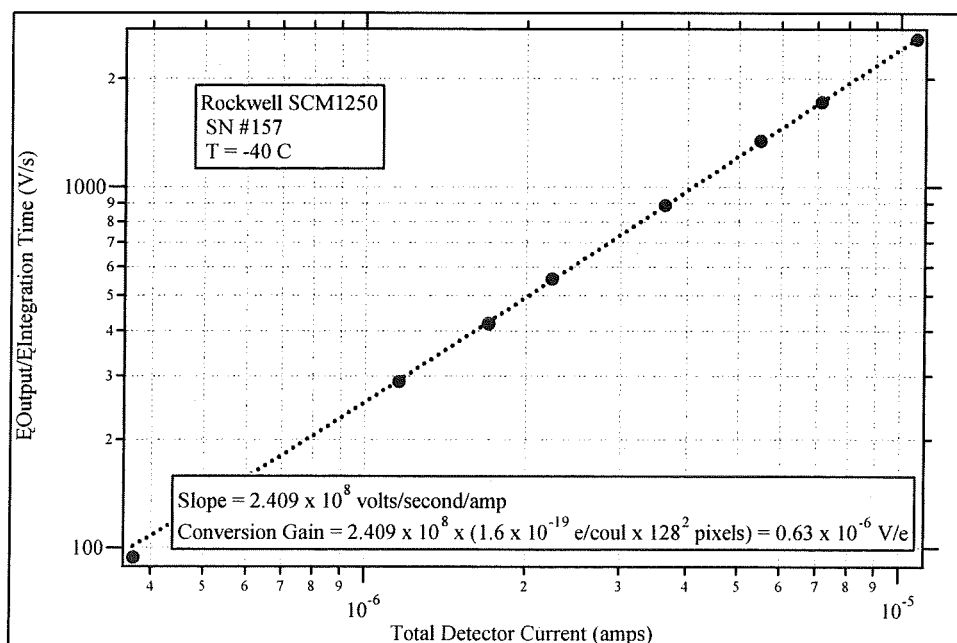


Figure 55. SN #157 DC Current Data Used to Determine Conversion Gain

**Mean-Variance Method** Pixel output voltages and RMS noises were measured at a number of photon irradiances at 650 nm and the square of the noise (variance) is plotted as a function of the output voltage in Figure 56. These data can be fit with a straight line, indicative of shot noise

limited operation, and the ROIC conversion gain, obtained as the slope of this plot, is  $0.547 \mu\text{V}/\text{electron}$ . It is unclear why the conversion gains determined from the two methods do not agree since the assumptions made for each method seem to be reasonable. The value determined from the DC current method,  $0.63 \times 10^{-6} \text{ V}/\text{e}$ , is thought to be the most correct since it is closer to the expected value. Conversion gain measurements were made as a function of proton fluence, and no change was observed.

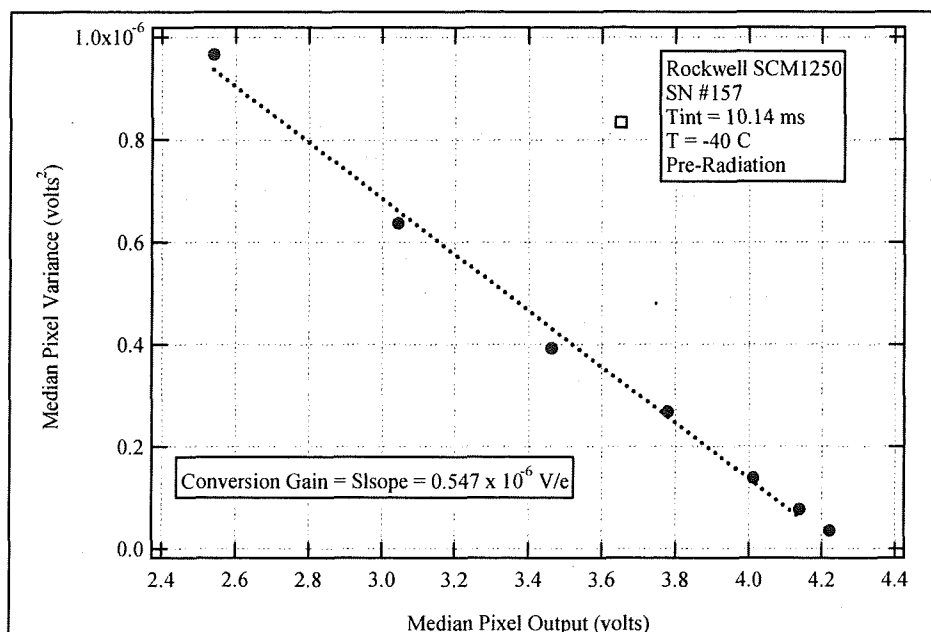


Figure 56. SN #157 Mean Variance Data Used to Determine Conversion Gain

The spectral response of SN #157 was determined using both the total detector current and the output voltages as measured as a function of wavelength. These data are shown in Figure . The *average* pixel quantum efficiency (QE) can be determined directly from the current measurement, while the conversion gain must be known to determine the QE from the output data. Using a conversion gain of  $0.65 \times 10^{-7} \text{ V}/\text{e}$  allows the QEs determined from the two sets of data to agree. It is not surprising that this value is close to that determined from the DC current method. The QE was monitored at several wavelengths as a function of proton fluence during the course of these measurements, and no changes were observed that were not within experimental error. This conclusion will be further reinforced below where responses as a function of proton fluence and detector bias are presented.

### 6.4.3 Output

Pixel output voltage data, obtained as a function of photon irradiance, are presented in this section. Data are also shown that describe the pixel output voltage as a function of the detector bias.



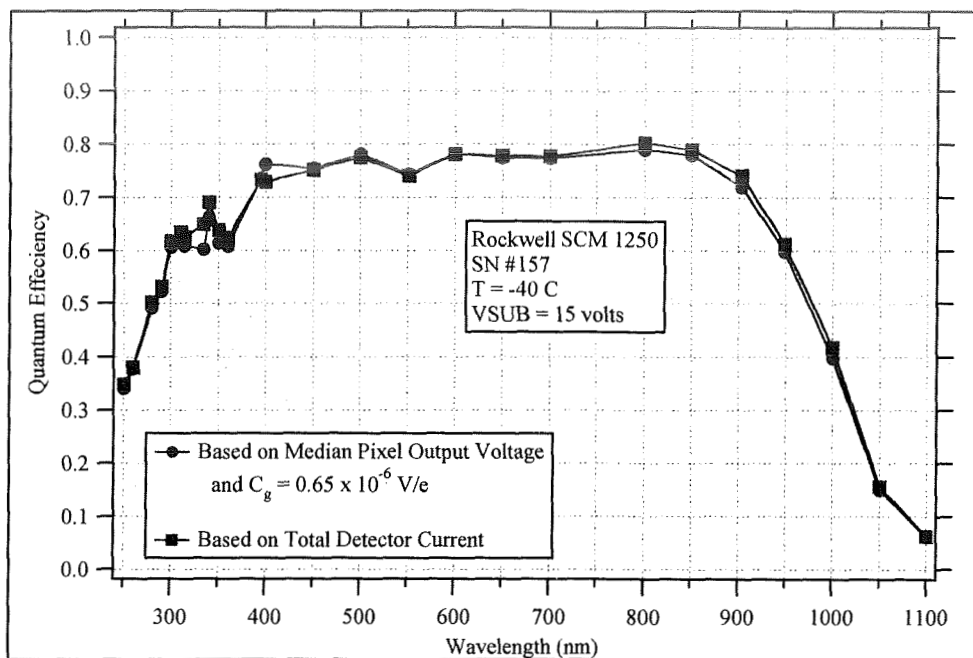


Figure 85. Spectral Response of SN #157 Using Both Detector Current and Output Voltage

#### 6.4.3.1 Responsivity

The median pixel output voltage is plotted as a function of photon irradiance at 650 nm in Figure and Figure . Figure is a plot of the pre-radiation data, showing the linearity of the ROIC of better than 1% over most of the output voltage range. Similar output data at different proton fluences, plotted in Figure , show that the responsivity, as determined from the slopes of these plots, is constant up to  $3 \times 10^{12} \text{ p/cm}^2$ , assuring that neither the QE nor the conversion gain change with fluence or total dose (to 400 krad(Si)). There is a slight shift in the output of approximately 50 mV at the maximum dose, no doubt due to uncompensated threshold shifts due to the total dose accumulation.

Responsivity histograms are shown in Figure for both pre-radiation and at the maximum proton fluence. These data were obtained from the difference in pixel outputs at two irradiances. Very little change is seen in either the average or the very uniform distribution.

#### 6.4.3.2 Response versus Bias

A major objective of these tests was to determine if the quantum efficiency (QE) of the PIN detectors changed with proton fluence, especially at very short UV wavelengths. While the detectors were completely depleted prior to radiation at a substrate bias of 15 volts, it was thought that higher biases might be necessary for full depletion at high proton fluences, and that the QE at a bias 15 volts could go down with fluence. Thus, QE as a function of bias was measured at several wavelengths prior to radiation, and the variation in QE with bias was tracked with proton fluence.

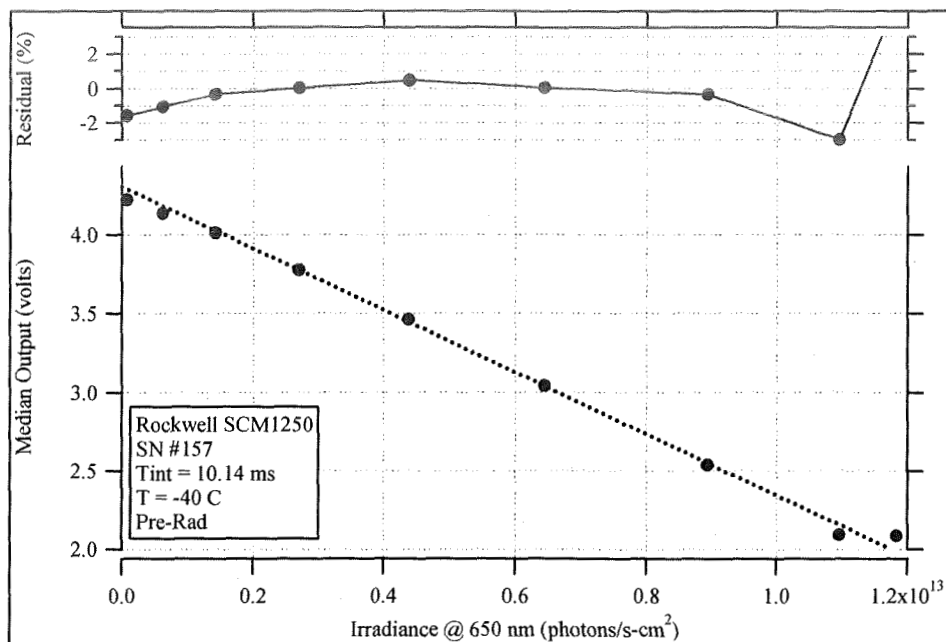


Figure 86. SN #157 Pre-Radiation Output versus Irradiance at 650 nm

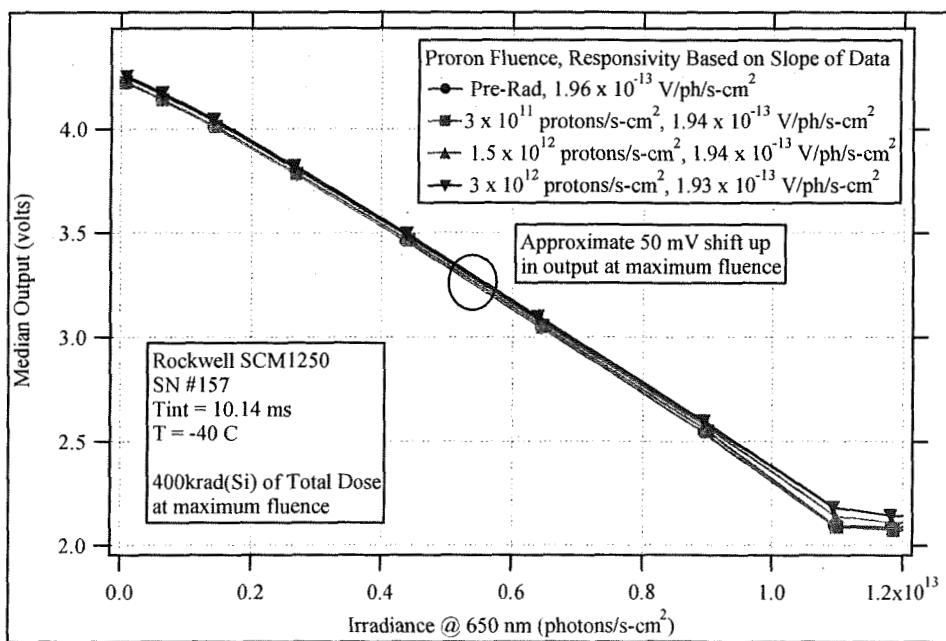


Figure 87. SN #157 Output versus Irradiance at 650 nm At All Proton Fluences

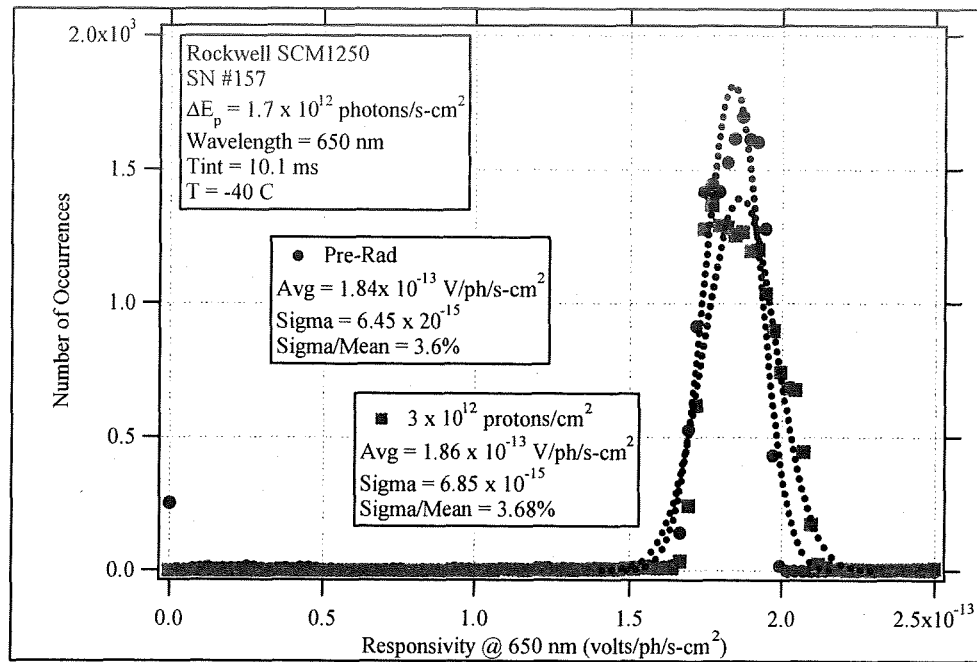


Figure 88. SN #157 Responsivity Histograms, Pre-Rad and Maximum Fluence

Prior to radiation, the QE was found to be independent of bias (V<sub>SUB</sub>) at all wavelengths from near zero volts to 15 volts. During the accumulation of proton fluence, little or no change in QE was observed over this bias range, and it was decided to increase the bias range to 40 volts to insure that full depletion was being achieved. Median pixel response, normalized to the response at a bias of 40 volts, is plotted in Figure at the maximum proton fluence,  $3 \times 10^{12} \text{ p/cm}^2$ . The data show that at the maximum fluence, a small increase in bias is required to reach the maximum response (QE), generally taking higher bias at shorter wavelengths. However, even at the shortest wavelengths, the loss of QE at a bias of 15 volts is less than 5% at the maximum fluence.

The ratio of the response at 15 V to that at 40 volts is plotted in Figure 57 as a function of wavelength in to illustrate this point. (The data point at 400 nm seems to be anomalously low and is probably due to a data collection error.) These data show that the QE at a substrate bias of 15 volts at all wavelengths decreases less than 3% up to a fluence of  $3 \times 10^{12} \text{ p/cm}^2$ , and an increase in substrate bias could further minimize this decrease.

#### 6.4.4 Dark Current

Dark currents were determined by measuring the output of the VFPA at several integration times at low photon irradiance. Data were obtained at several integration times at each fluence to insure the measured data were linear with integration time. The median pixel dark current versus proton fluence is shown in Figure 58. These data show that the dark current increases approximately linearly with fluence, approximately 2 orders of magnitude from pre-rad to the maximum fluence,  $3 \times 10^{12} \text{ p/cm}^2$ . The dark current for SN #157 at higher fluences is approximately one-half that of SN #150, which is twice as thick.

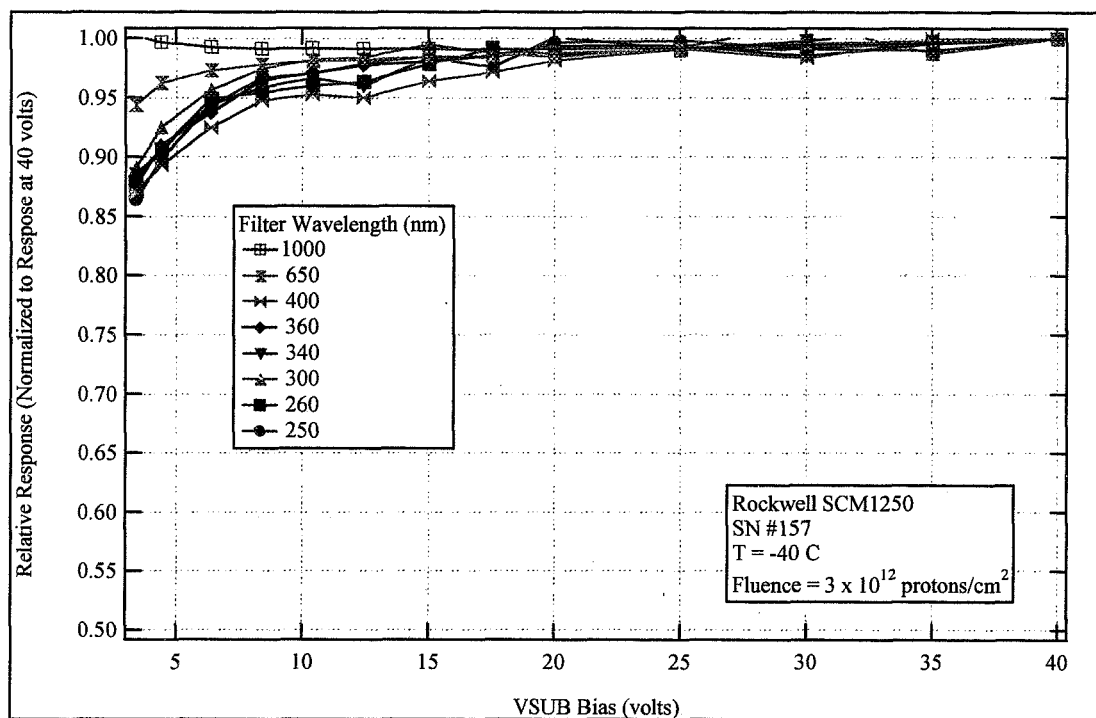


Figure 89. SN #157 Normalized Response versus Substrate Bias at Several Wavelengths

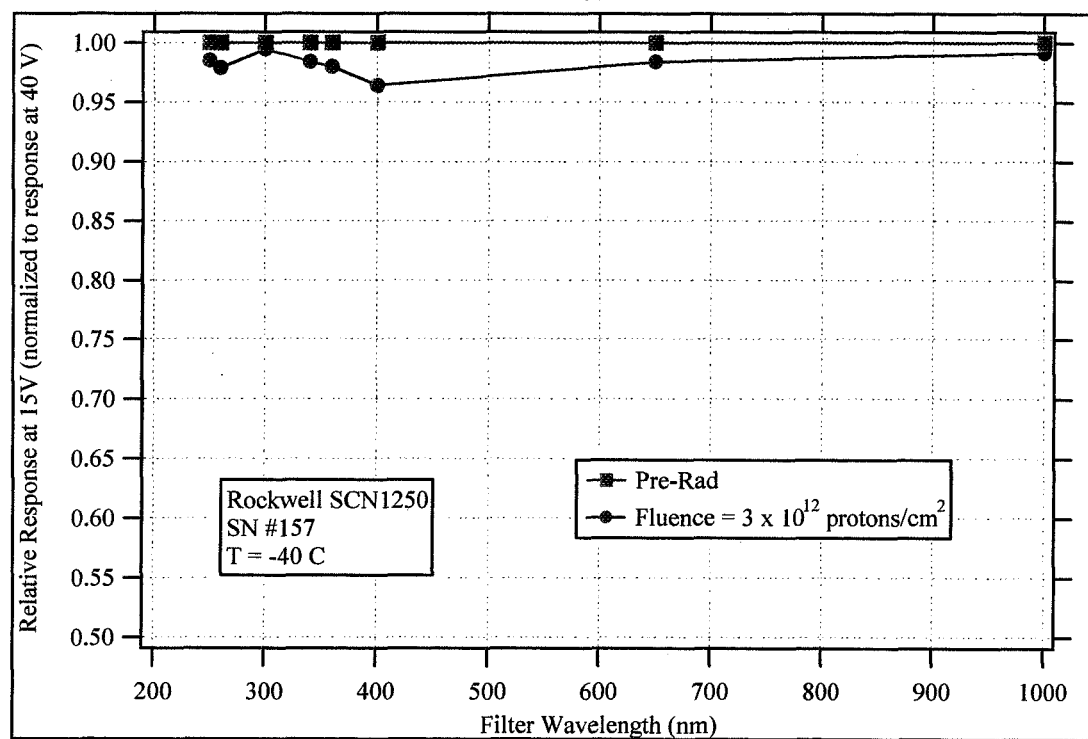


Figure 57. SN #157 Relative Response at VSUB = 15 V versus Wavelength

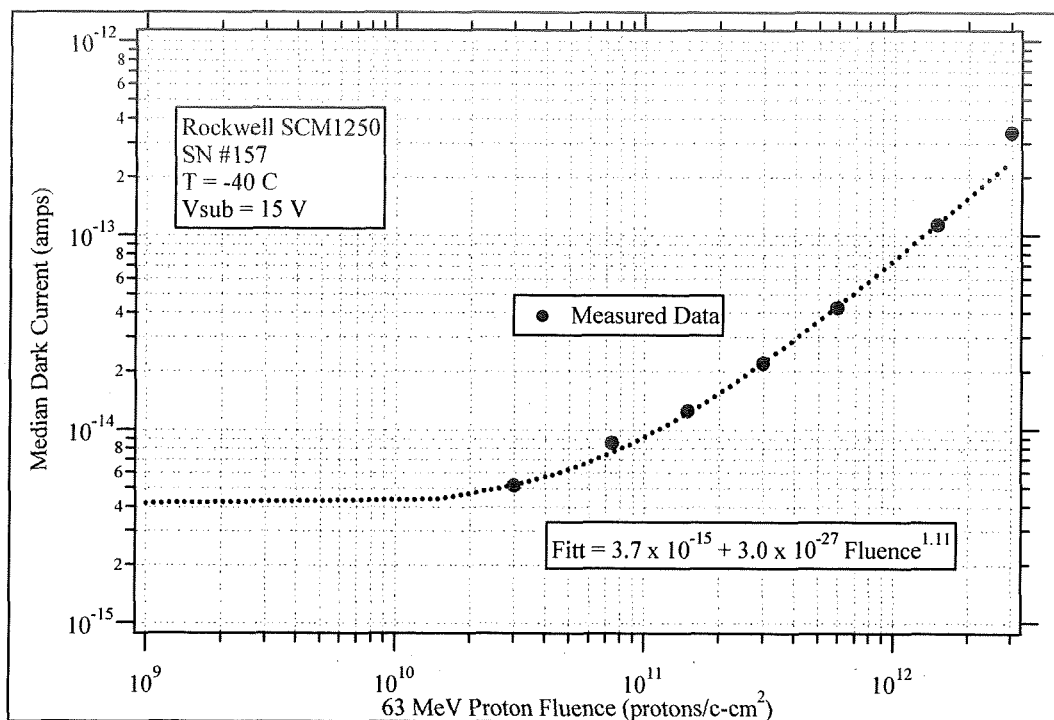


Figure 58. SN #157 Dark Current versus Proton Fluence

The pre-radiation median pixel dark current, along with the dark current at the maximum proton fluence, is shown as a function of inverse temperature in Figure 59. Dark current distributions for pre-radiation and maximum fluence conditions are shown in Figure 60 and Figure 61, respectively. While both distributions are quite uniform, the distribution at the maximum fluence has groups of pixels with currents both higher and lower than the main group of pixels.

A 2-D map of the pre-radiation dark current is shown in Figure . As indicated by the histogram above, the current is quite uniform. A dark current map at  $3 \times 10^{12}$  p/cm<sup>2</sup>, given in Figure , shows that the higher current pixels tend to be located around the perimeter of the detector array and the lower current pixels are in the lower right hand corner. This result is consistent with the results seen for the other three devices and is likely due to a bias non-uniformity cause by a voltage drop across the detector common lead.

#### 6.4.5 Noise

Median pixel noise data, pre-radiation and at several proton fluences, are shown as functions of irradiance in Figure . Also shown in this figure are plots of read noise, photon noise, and the total noise (dark current noise is not significant at these irradiances and integration times). The read noise used was 0.18 mV, and the photon noise was based on a quantum efficiency of 0.70 and a conversion gain of  $0.63 \times 10^{-6}$  V/e. The median noise basically has two terms, readout noise and photon noise, and there is little change with fluence. These data support the conclusion that neither the quantum efficiency nor the conversion gain change appreciably with proton fluence.

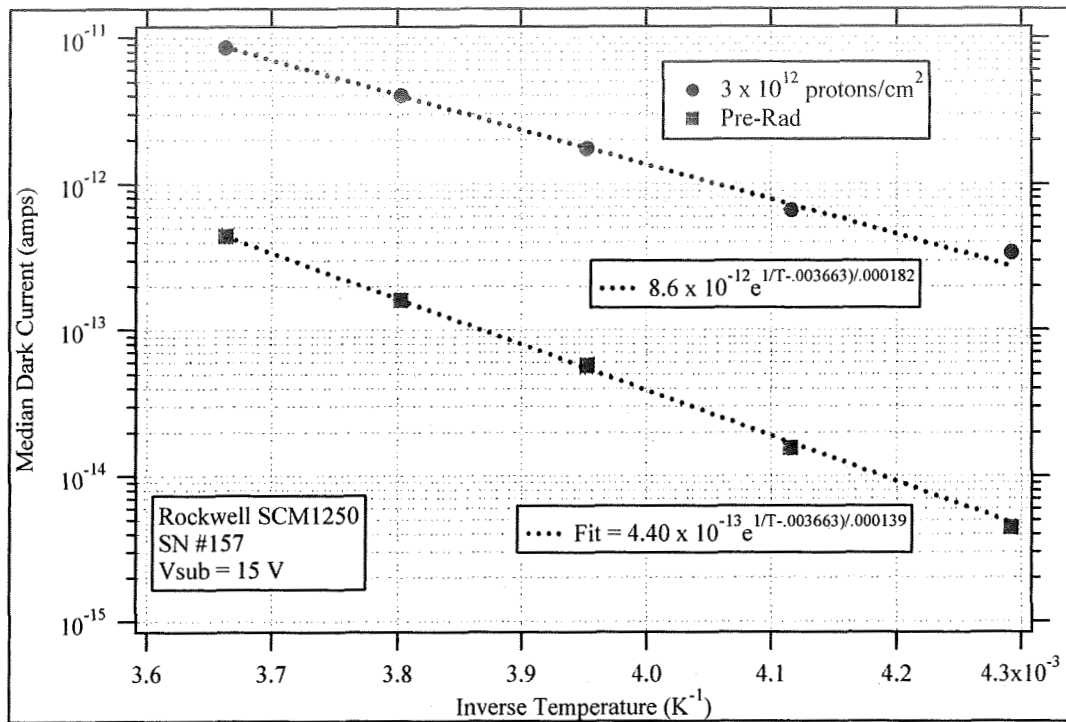


Figure 59. SN #157 Dark Current versus Inverse Temperature

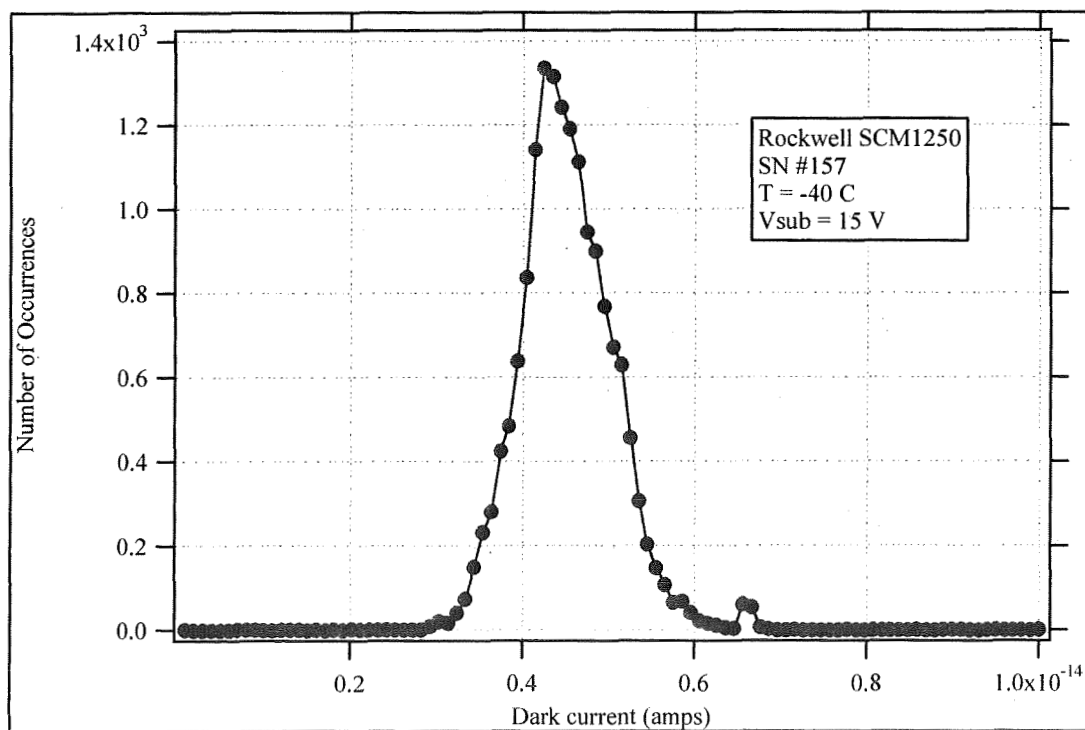


Figure 60. SN #157 Pre-Rad Dark Current Distribution

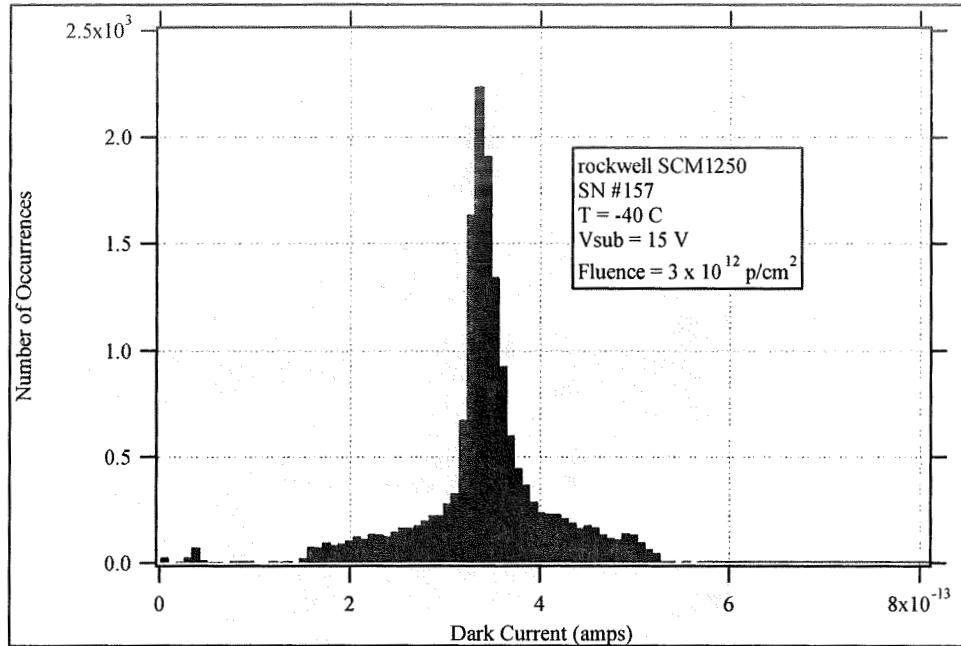


Figure 61. SN #157 Dark Current Histogram at  $3 \times 10^{12}$  p/cm<sup>2</sup>

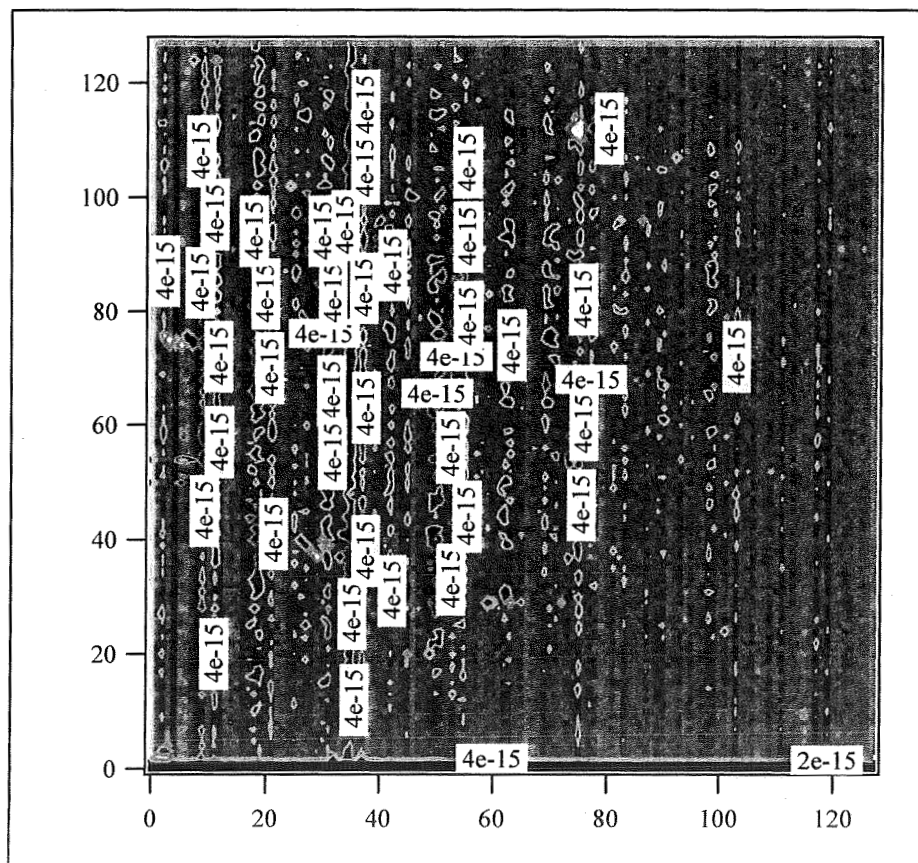


Figure 95. SN #157 2-D Map of Pre-Radiation Dark Current

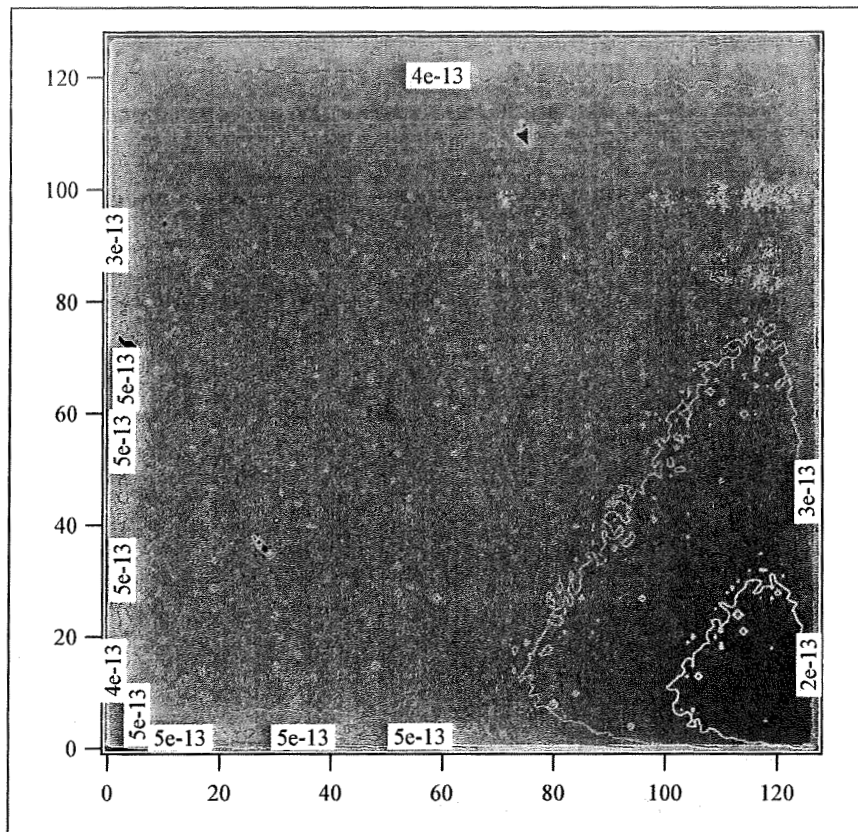


Figure 96. SN #157 2-D Dark Current Map at  $3 \times 10^{12}$  protons/cm<sup>2</sup>

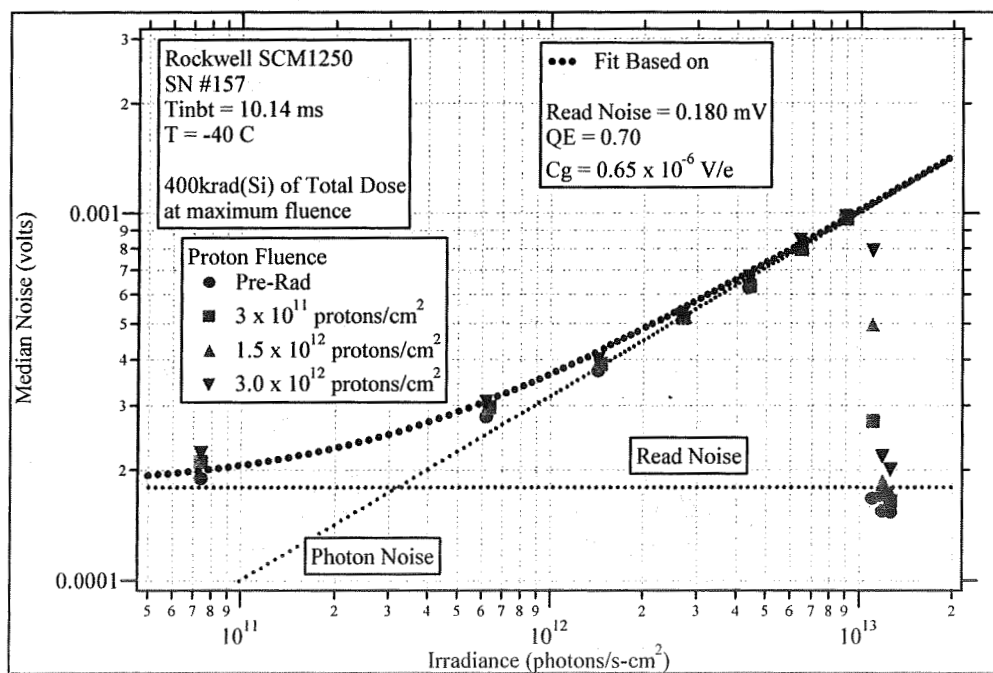


Figure 97. SN #157 Noise versus Irradiance at 650 nm



Histograms of noise at an irradiance of  $6.4 \times 10^{12}$  ph/s-cm<sup>2</sup> for pre-radiation and at the maximum fluence are shown in Figure . Both distributions are relatively uniform with a slight increase in average noise at the highest fluence, which could be due to activation of Dewar parts by protons. There is a slight increase in the number of pixels with higher in the tail, and these pixels located are at one edge of the array.

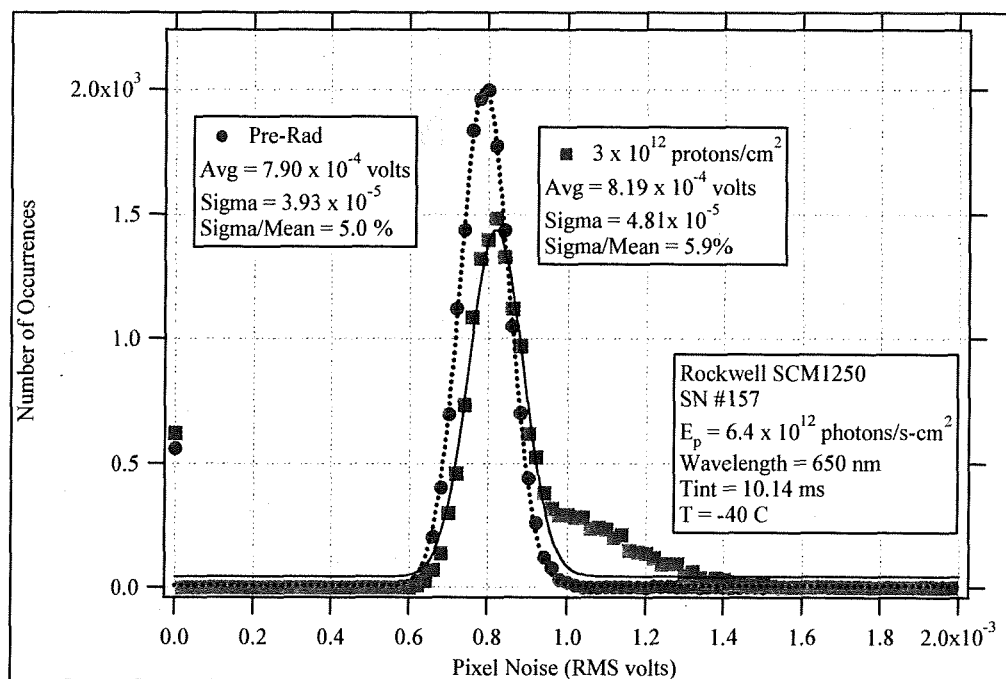


Figure 98. SN # 157 Noise Histograms at  $6.4 \times 10^{12}$  ph/s-cm<sup>2</sup>

#### 6.4.6 Transient Data

Output data were collected from all pixels during irradiation by protons at three fluence rates. The geometry for this set up, which was shown in Figure 7, is repeated in more detail in Figure . The pixel is 60 x 60 micrometers in size and is 60 micrometers thick, and it is aligned at 45 degrees with the proton beam. Looking at the figure, we see that some protons can pass through a single pixel (protons a – b, g – h), while most protons pass through two pixels, creating two events. The probability of passing through one pixel is approximately 10/60 = 0.167, and the probability of passing through two is 50/60 = 0.833. The expected number of proton events is thus:  $1 \times 0.167 + 2 \times 0.833 = 1.83$  events/proton. Furthermore, since the amount of charge produced by a proton is roughly proportional to its path length and the path lengths (for 2 event protons) extend from zero to the  $50 \times (2)^{0.5}$  micrometers, the diagonal of a 50 micrometer square, one expects a distribution of charge from proton events that is roughly uniform from zero to some maximum charge, with a slight peak near the maximum charge corresponding to those protons that passed through one pixel near the diagonal.

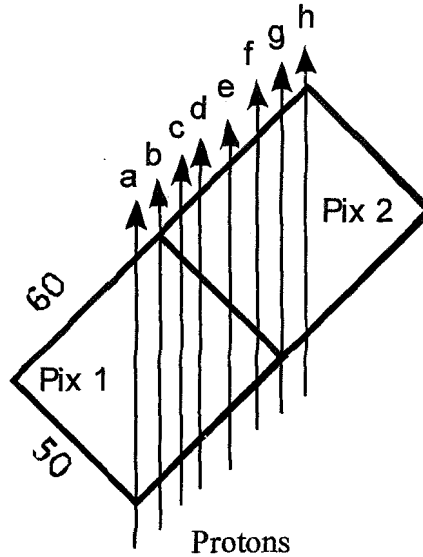


Figure 99. Proton Geometry for SN #157

Histograms of pixel outputs for 25 frames of data collected at three proton fluence rates are shown in Figure 62. Those pixels with no events are peaked around zero volts, there is a flat region that extends from about 5 mV to 20 mV, and an exponential region extends out to approximately 200 mV. The flat region is thought to be due to the protons that pass directly through the pixels as described above. At the lowest fluence rate,  $1.7 \times 10^5$  p/s-cm<sup>2</sup>, the total number of events in this region (extended to zero volts) is  $2.88 \times 10^4$  events. The total number of protons incident on the VFPA during this 25 frames at an integration time of 10 ms is:

$$\# \text{ Protons} = 1.7 \times 10^5 \text{ p/s-cm}^2 \times (60 \mu\text{m} \times 128)^2 \times \cos(45) \times 25 (10 \text{ ms}) = 1.77 \times 10^4$$

Thus, the number of events per proton is  $2.88 \times 10^4 / 1.77 \times 10^4 = 1.63$ , which is in reasonable agreement with the predicted number of 1.83. The source of the high amplitude events is not known.

One set of data was obtained at the maximum fluence rate for 1 and a histogram is shown in Figure 63. With the data provided by the additional frames, the shape of the distribution at higher output voltages is clearer.

Three frames of output data at the three proton fluence rates are shown in Figure 64 through Figure 66. Here, black represents no proton events and the events amplitudes increase as the colors move through the following color sequence: brown, red, orange, yellow, white, and blue. The presence of proton events in adjacent pixels is apparent, especially at the higher event rates.

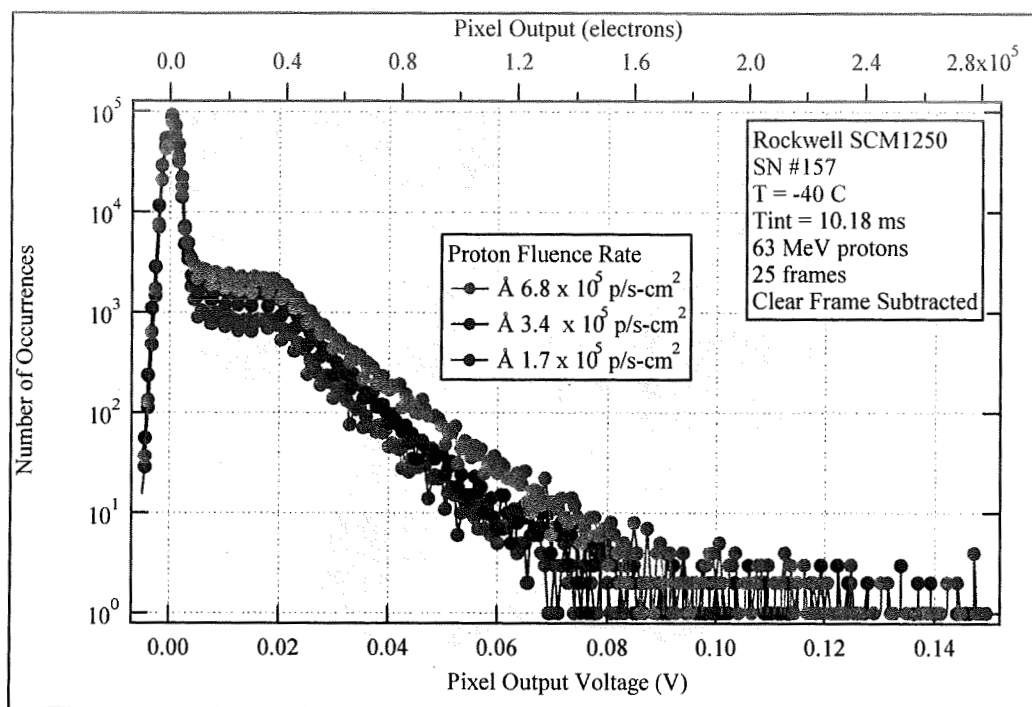


Figure 62. SN #157 Histograms of Output at Different Fluence Rates for 25 Frames

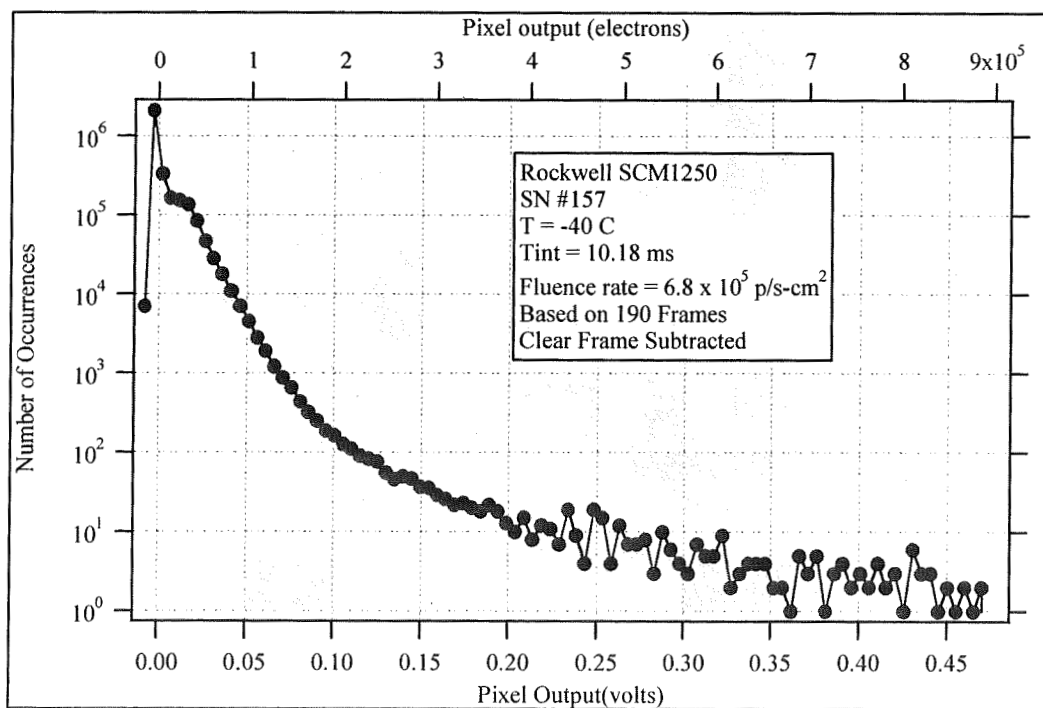


Figure 63. SN #157 Histogram of Output from 190 Frames at  $6.8 \times 10^5$  p/s-cm<sup>2</sup>

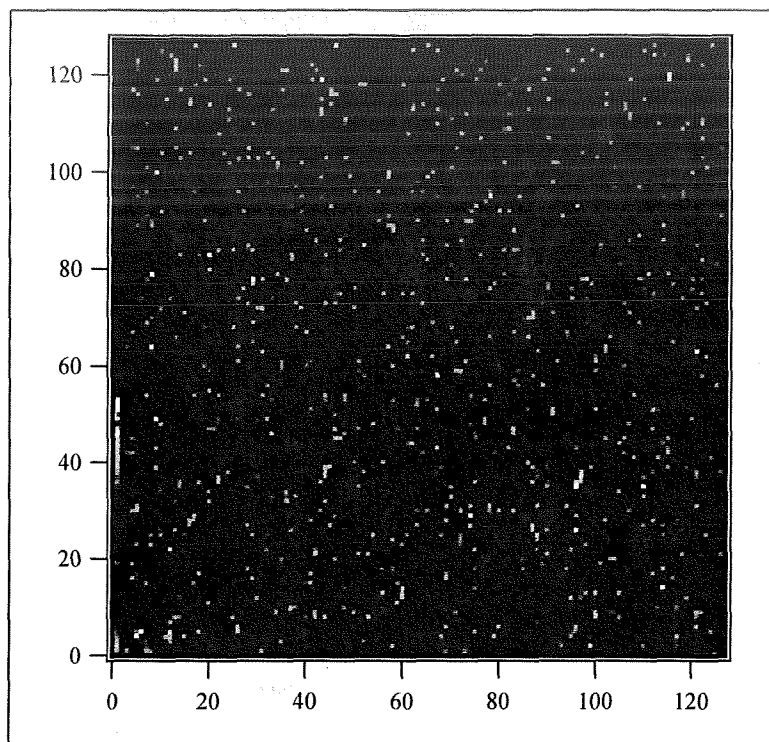


Figure 64. SN #157 One Output Frame at  $1.7 \times 10^5$  protons/s-cm<sup>2</sup>

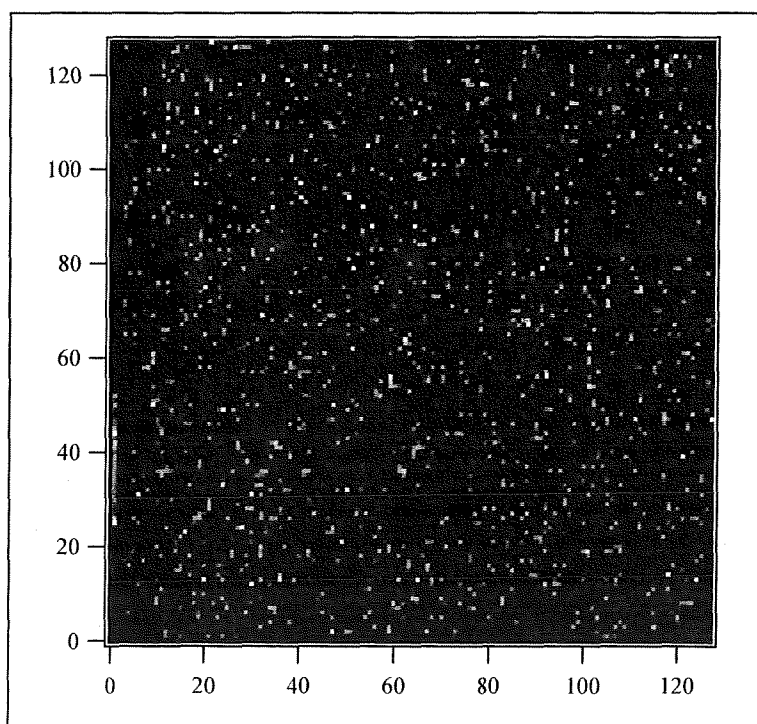


Figure 65. SN #157 One Output Frame at  $3.4 \times 10^5$  protons/s-cm<sup>2</sup>

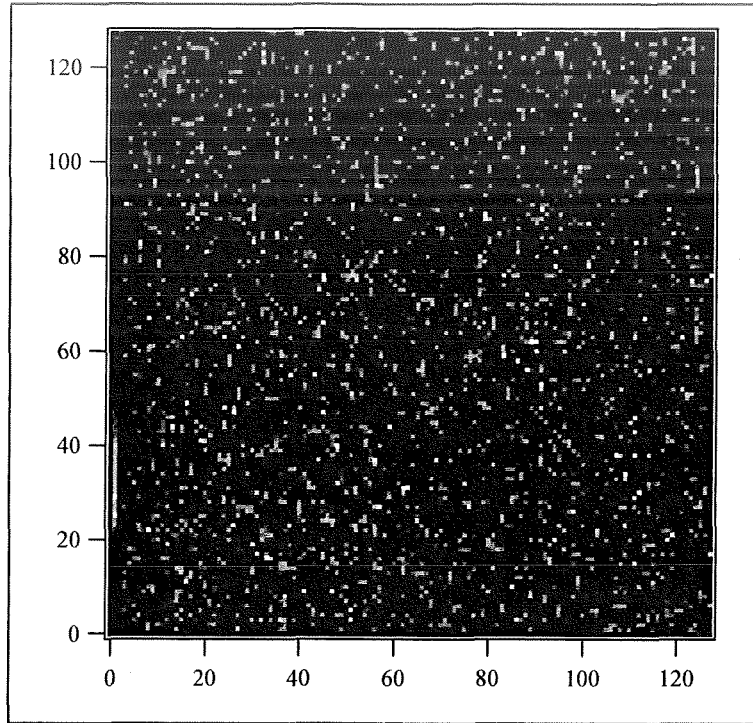


Figure 66. SN #157 One Output Frame at  $6.8 \times 10^5$  protons/s-cm<sup>2</sup>